FIRST-PRINCIPLES STUDY OF ANTIFERROELECTRIC OXIDE CRYSTALS

BY SEBASTIAN E. REYES LILLO

A dissertation submitted to the

Graduate School—New Brunswick

Rutgers, The State University of New Jersey

in partial fulfillment of the requirements

for the degree of

Doctor of Philosophy

Graduate Program in Physics and Astronomy

Written under the direction of

Karin M. Rabe

and approved by

_____

_____

_____

_____

_____

New Brunswick, New Jersey

OCTOBER, 2014

ABSTRACT OF THE DISSERTATION

First-principles study of antiferroelectric oxide crystals

by Sebastian E. Reyes Lillo

Dissertation Director: Karin M. Rabe

The fundamental physics of antiferroelectric crystal oxides is studied using first principles methods. The microscopic origin of antiferroelectricity in traditional perovskite antiferroelectrics and other oxide compounds is investigated. The structural and energetic competition between ferroelectricity and antiferroelectricity is explored under the effect of epitaxial strain and compositional modification. The energy landscape of the field-induced ferroelectric transition is described with a Landau-Devonshire model. The work concludes with a search for more antiferroelectric materials. Promising candidates are identified and the role of tuning parameters is discussed.

Acknowledgements

During these five years of doctoral studies in Rutgers, I have had the pleasure of meeting a number of wonderful people whose moral support was fundamental for the completion of this work. First of all, I would like to thank my advisor Karin Rabe, for giving me the opportunity to work under her supervision, and for all the wonderful opportunities that she gave me during my thesis work. Among the professors involved in my professional development I would like to thank David Vanderbilt, Michael Gershenson, Natan Andrei, Premala Chandra and Lev Ioffee for their scientific guidance and encouragement. Also, I would to acknowledge the postdocs and group members for their help learning the code and the theoretical formalism.

The summer internships at the Material Research Institute in Penn State University were especially important for the progress of my thesis work. I would like to thank Susan Trolier-McKinstry, Clive Randall and their group for their hospitality during these internships and for stimulating scientific discussions. I would also like to thank the members of the thesis committee: Tom Banks, Girsh Blusmberg, Emil Yuzbashyan as well as my academic advisors Ron Ransome, Ted Williams and Ron Gilman for their guidance, suggestions, and corrections during this work. Additionally, I would like acknowledge the support from the Physics and Astronomy Department of Rutgers University, the Office of Naval Research (ONR), the Consejo Nacional de Ciencia y Tecnologia (Conicyt) and the Fulbright Foundation.

Finally, I would like to thank Elaina for her love and unconditional support during my doctorate studies. I would also like to thank my parents and family in Chile as well as Elaina's family in New Jersey for their love and encouragement during my doctorate studies. Also, I would like to thank Eliav Edrey, Brett Manning and Matt Brahlek for their friendship and kindness.

Dedication

To my son, Benjamin

Table of Contents

Abstract ii

Acknowledgements iii

Dedication iv

1. Introduction 1

2. First principles methods 3

2.1. Solid state Hamiltonian 3

2.1.1. Born-Oppenheimer approximation 4

2.1.2. Hellman-Feynman theorem 5

2.2. Density functional theory 5

2.2.1. Approximate exchange-correlation potential 8

2.2.2. Density functional perturbation theory 9

2.3. Structural and electronic properties 10

2.3.1. Polarization 11

2.3.2. Epitaxial strain 12

2.4. Practical implementations 14

2.4.1. Plane wave basis 14

2.4.2. Brillouin grid 15

2.4.3. Pseudopotentials 15

2.4.4. Space group symmetries 16

2.4.5. Software packages 17

3. Ferroelectricity and antiferroelectricity 19

3.1. Ferroelectricity 19

3.1.1. Prototypical example 21
3.2. Microscopic models of ferroelectricity 22
3.2.1. Landau-Devonshire 22
3.2.2. Soft mode theory 24
3.2.3. Effective models 25
3.3. Antiferroelectricity 27
3.3.1. Kittel's model of antiferroelectricity 28
3.3.2. Definition of antiferroelectricity 31
3.4. Microscopic model of antiferroelectricity 34
3.5. Antiferroelectric materials 39
3.5.1. Functional properties 40

4. Antiferroelectric perovskites 43
4.1. The physics of ABO_3 perovskites 43
4.1.1. Glazer notation 45
4.1.2. Technical details 46
4.1.3. Ferroelectric and antiferrodistortive distortions 46
4.2. Antiferroelectric perovskites 49
4.3. Why are there so few antiferroelectric perovskites? 53
4.3.1. Kittel antiferroelectric phases 55
4.3.2. The role of oxygen octahedron rotations 57
4.3.3. Antiferroelectric energy barrier 58
4.3.4. Origin of the small energy difference 60
4.3.5. Conclusions 61

5. Antiferroelectricity and ferroelectricity in epitaxially strained $PbZrO_3$ from first principles 63
5.1. Thin film $PbZrO_3$ 64
5.1.1. Technical details and notations 65
5.1.2. Bulk results 67

5.1.3. Epitaxial strain . . . 69
5.1.4. Discussion . . . 72
5.2. Conclusions . . . 72

6. Nonlinear increase of critical electric-field in doped antiferroelectric $NaNbO_3$ . . . 73
6.1. Field-induced ferroelectric transition in $NaNbO_3$ . . . 73
6.2. Technical details . . . 76
6.3. First principles results . . . 77
6.3.1. Energy landscape . . . 77
6.3.2. Chemical substitution . . . 79
6.4. Conclusions . . . 81

7. Antiferroelectricity in thin film ZrO_2 from first principles . . . 82
7.1. Thin film ZrO_2 . . . 83
7.2. Technical details . . . 85
7.3. First principles results . . . 85
7.3.1. Energy barrier . . . 87
7.3.2. Landau-Devonshire model . . . 88
7.3.3. Epitaxial strain . . . 89
7.3.4. Comparison with hafnia (HfO_2) . . . 90
7.4. Conclusions . . . 91

8. High-throughput search of antiferroelectric oxides . . . 93
8.1. Technical details . . . 94
8.2. Orthorhombic ABO_3 as perovskite antiferroelectrics . . . 94
8.2.1. Epitaxial strain . . . 100
8.2.2. Chemical modification . . . 100
8.3. Ferroic order in orthorhombic AXY compounds . . . 102
8.4. Conclusions . . . 108

9. Conclusions 109

References 112

Chapter 1

Introduction

Antiferroelectricity was introduced by C. Kittel in 1951 [1] and soon after that was discovered by G. Shirane in the perovskite compound lead zirconate ($PbZrO_3$) [2]. Since then, and compared to ferroelectricity, the fundamental physics of antiferroelectricity has received little attention in condensed matter physics [3, 4]. The spurious identification of local electric dipoles, analogous to magnetic moments, does not allow for a definition of antiferroelectricity equivalent to the definition of antiferromagnetism based on complementary sublattices. Furthermore, the complex structures of known antiferroelectrics have slowed advances in the subject.

Antiferroelectric materials are characterized by a centrosymmetric crystal structure with an alternative competing low-energy ferroelectric phase [5]. The small free energy difference between antiferroelectric and ferroelectric structures corresponds to an intrinsic property of the material and gives rise to a characteristic double hysteresis loop. The first-order transition that produces the field-induced ferroelectric phase is the source of promising technological applications.

$PbZrO_3$ has a paraelectric perovskite structure at high temperature and an antiferroelectric phase with orthorhombic structure below 505 K [6]. The low-temperature antiferroelectric phase consists of an antipolar displacement of Pb ions, accompanied by a rather complex oxygen octahedral rotation pattern. Antiferroelectric double hysteresis loops are experimentally observed in $PbZrO_3$ based ceramics, single crystals and thin films. Optimal functional properties for technological applications are pursued through a variety of tuning parameters such as compositional modification or size effects [7].

As a result of the great progress in synthesis of materials and first principles methods, there is a renewed interest in the phenomenon of antiferroelectricity and its potential

technological applications. The great advances of the modern theory of polarization stimulate a reexamination of the fundamental physics of antiferroelectricity. Integrated database and first principles methods suggest a high-throughput search of more antiferroelectric materials with enhanced functionalities and novel properties.

The thesis is divided into chapters, each corresponding to different projects developed during the doctoral work. Chapter 2 introduces the basic concepts of density functional theory and first-principles methods. In chapter 3, the physics of ferroelectricity and antiferroelectricity is reviewed. The difficulties arising in the formulation of a precise definition of antiferroelectricity are discussed. The microscopic origin of macroscopic properties observed in antiferroelectrics is investigated with a phenomenological model.

In chapter 4, first principles methods are used to investigate the scarcity of pure antiferroelectrics in the perovskite family of compounds. The structural and energetic conditions required for the stabilization of antiferroelectricity are explored in specific antiferroelectric perovskites. Chapter 4 has an introductory character and allows the study of specific antiferroelectric perovskites in subsequent chapters. Chapter 5 studies the effect of epitaxial strain in the competition of ferroelectric and antiferroelectric phases of lead zirconate. In chapter 6, recent experimental results obtained for the field-induced ferroelectric transition in sodium-niobate-based ceramics are examined using first principles methods. Chapter 7 presents our work on thin-film antiferroelectric zirconia. The experimental discovery of this new functional property in this extensively investigated material is supported with first principles methods. Finally, in chapter 8, a high-throughput search of more antiferroelectric materials is presented in the ABO_3 perovskite family and in other families of oxide compounds. Chapter 8 corresponds to work in progress and therefore can guide future work in the subject.

Chapter 2

First principles methods

In this chapter the basic concepts of density functional theory and first principles methods are reviewed. Structural and electronic properties of interest are introduced, as well as computational techniques used throughout this work.

First principles calculations are fundamental for the prediction and analysis of materials in solid state physics. The fundamental equations of quantum mechanics and electromagnetism that describe molecules and crystals are efficiently solved using a few input parameters, such as the positions of the atoms and the lattice constants.

In the first section of this chapter the crystal Hamiltonian and density functional theory are introduced, along with the local density approximation and the Kohn-Sham equations. First principles methods for the calculation of polarization, unstable modes and epitaxial strain diagrams are described as important applications. Finally, the third section describes pseudopotentials and practical aspects of the computational implementation.

2.1 Solid state Hamiltonian

The fundamental equation describing the state of an interacting system of particles corresponds to the time independent Schroedinger equation [8] given by:

$$\hat{H}\Psi = E\Psi, \tag{2.1}$$

where $\hat{H}$ is the Hamiltonian operator, E is the energy and Ψ is the many-body wave function of the system. In the case of a solid state system, the complete Hamiltonian [9] is given by:

$$\hat{H}(R,r) = \hat{T}_N(R) + \hat{T}_e(r) + \hat{V}_{NN}(R) + \hat{V}_{ee}(r) + \hat{V}_{Ne}(R,r), \tag{2.2}$$

where $R \equiv \{R_I\}$ labels the set of nuclear positions R_I and $r \equiv \{r_i\}$ labels the set of electronic positions r_i. $\hat{T}_N$ and $\hat{T}_e$ denote the kinetic energy operators for the nuclei and electrons, and $\hat{V}_{NN}$, $\hat{V}_{ee}$ and $\hat{V}_{Ne}$ denote the electrostatic potential energy operators between the nuclei, electrons, and nuclei and electrons, respectively. In the non relativistic limit, these operators are given by:

$$\hat{T}_N = \sum_I -\frac{\hbar^2}{2M_I}\frac{\partial^2}{\partial R_I^2}, \qquad \hat{T}_e = \sum_i -\frac{\hbar^2}{2m}\frac{\partial^2}{\partial r_i^2},$$

$$\hat{V}_{NN} = \frac{1}{2}\sum_{I\neq J}\frac{e^2 Z_I Z_J}{||R_I - R_J||}, \qquad \hat{V}_{ee} = \frac{1}{2}\sum_{i\neq j}\frac{e^2}{||r_i - r_j||}, \qquad \hat{V}_{Ne} = -\sum_{i,I}\frac{e^2 Z_I}{||r_i - R_I||},$$

where M_I and Z_I correspond to the mass and charge of ion I, and m and $-e$ are the mass and elementary charge of the electron.

2.1.1 Born-Oppenheimer approximation

The full many-body problem described by Eq. 2.1 and 2.2 includes all the interaction among electrons and ions. Since the electron/ion mass ratio is very small in a crystal ($m/M_I \sim 0.01$), the slow ionic degrees of freedom can be neglected in favor of the much faster electronic degrees of freedom [10]. If the kinetic energy term T_N is neglected, the nuclei positions are effectively fixed, the electronic degrees of freedom are decoupled from Eq. 2.2 and the system of electrons is described by the Hamiltonian:

$$\hat{H}_e(r) = \hat{T}_e(r) + \hat{V}_{ee}(r) + \hat{V}_{ext}(r), \tag{2.3}$$

where the electrostatic potential $\hat{V}_{Ne}$ is interpreted as an external perturbation $\hat{V}_{ext}$ for the system of electrons. The electronic kinetic energy $\hat{T}_e$ and electrostatic potential energy $\hat{V}_{ee}$ have the same form as before, whereas the ionic kinetic energy $\hat{T}_N$ and electrostatic potential energy $\hat{V}_{NN}$ are constants that shift the reference energy.

The electronic Hamiltonian given by Eq 2.3 correspond to an effective description of the many-body system. Given the nuclei positions, the total energy, charge density and set of eigenstates can be obtained by solving a Schroedinger equation for $\hat{H}_e$.

2.1.2 Hellman-Feynman theorem

A wide variety of physical properties can be accessed from derivatives of the total energy. If an external perturbation of the system is denoted with the parameter λ, the Hellman-Feynman theorem [11] is given by:

$$\frac{dE}{d\lambda} = \langle \Psi_\lambda | \frac{d\hat{H}_\lambda}{d\lambda} | \Psi_\lambda \rangle,$$

where the wavefunction Ψ_λ corresponds to the eigenstate of the perturbed Hamiltonian $\hat{H}_\lambda$.

The Hellman-Feynman theorem allows the calculation of forces and stresses through first-order derivatives of the total energy. In particular, the optimized equilibrium ionic structure of the system can be found by minimization of the forces among ions [12].

Higher-order derivatives of the energy can be determined through finite differences of small perturbations of the Hamiltonian. In the frozen-phonon technique, finite values of the perturbation are frozen in to the structure and derivatives are extracted from finite difference formulas.

2.2 Density functional theory

The total energy of the interacting system of electrons and ions is the fundamental quantity of interest in the description of solid state systems. However, even with the Born-Oppenheimer approximation, the solution of the many-body system of N_e electrons in a macroscopic solid ($N_e \sim 10^{23}$) remains an impossible task. In practice, other simplifications are required to solve the Schroedinger equation for $\hat{H}_e$.

Density Functional Theory (DFT) provides an efficient approach to solve the interacting electronic system given by Eq 2.3. The theory is constructed in seminal publications by Hohenberg and Kohn [13] and Kohn and Sham [14]. In the following we review the main results of DFT.

The first DFT paper shows that the ground state electronic density $n_0(r)$ of a quantum mechanical many-body system can be considered as a fundamental quantity

of the problem, so that the total energy of the system can be considered as a functional of the charge density.

More specifically, Hohenberg and Kohn proved that the external potential V_{ext} of the system can be uniquely determined from the ground state charge density $n_0(r)$ and vice versa. The proof of the theorem follows from the construction of the Hohenberg-Kohn energy functional $E_{HK}[\cdot]$ from the space of functions n to the real numbers:

$$E_{HK}[\cdot]: n \longrightarrow \mathbb{R},$$

which is well defined, and has the functional form given by:

$$E_{HK}[n] = T[n] + V_{ee}[n] + \int V_{ext}(r)n(r)dr. \tag{2.4}$$

The kinetic energy $T[n]$ and electrostatic potential energy $V_{ee}[n]$ include the interactions among electrons and their functional form is unknown. The exact ground state energy E_0 and the exact ground state many-body wavefunction Ψ_0 are uniquely determined by the charge density that minimizes the Hohenberg-Kohn energy functional E_{HK}. Unfortunately, although the Hohenberg-Kohn theorem proves the existence of this functional, the theorem does not provide its explicit form.

The second DFT paper proposes an explicit method to solve the interacting many-body system. As is squematically represented in Fig. 2.1, the interacting system of electrons moving in the crystal potential is mapped into an equivalent system of non-interacting fictitious particles.

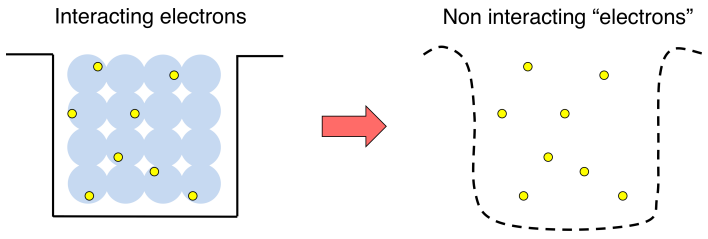

Figure 2.1: Representation of the DFT mapping from the fully interacting system of electrons to the non-interacting system of Kohn-Sham particles.

The Kohn-Sham approach replaces the interacting kinetic $T[n]$ and electrostatic $V_{ee}[n]$ operators with their non-interacting versions and re-writes the Hohenberg-Kohn

energy functional in the following form [9]:

$$E^{HK}[n] = T_0[n] + V_H[n] + E_{xc}[n] + \int V_{ext}(r)n(r)dr,$$

where $T_0[n]$ corresponds to the non-interacting kinetic energy operator, $V_H[n]$ corresponds to the classical Coulomb electrostatic energy or Hartree term, $E_{xc}[n]$ corresponds to the exchange and correlation energy between electrons, given by:

$$E_{xc}[n(r)] = (T[n] - T_0[n]) + (V_{ee}[n] - V_H[n]),$$

and V_{ext} is the external electrostatic energy created by the interaction between electrons and ions.

If $\{\psi_i(r)\}$ denotes the set of non-interacting Kohn-Sham particles, the charge density of the non-interacting system is given by:

$$n(r) = \sum_i |\psi_i(r)|^2$$

and the energy functional given by Eq. 2.4 can be written as:

$$E^{HK}[\psi_i] = -\frac{1}{2}\sum_i \langle\psi_i|\nabla^2|\psi_i\rangle + \frac{1}{2}\int \frac{n(r)n(r')}{||r-r'||}drdr' + E_{xc}[n(r)] + \int V_{ext}(r)n(r)dr. \tag{2.5}$$

With the exception for the exchange-correlation term $E_{xc}[n(r)]$, that contains all the electronic interactions beyond the classical Coulomb potential, all the terms in Eq. 2.5 are completely determined by the charge density $n(r)$. If the exact functional form of $E_{xc}[n]$ is known, the exact ground state energy and charge density of the many-body electron problem is determined.

For a set of atomic positions, the ground state is determined via the minimization of Eq. 2.5 under the constraint $\langle\psi_i|\psi_j\rangle = \delta_{ij}$; details can be found in [9]. Defining the Hartree and exchange-correlation potentials as the functional derivatives of the Hartree and exchange-correlation energies with respect to the density:

$$V_H = \frac{\delta E_H[n]}{\delta n(r)}, \qquad V_{xc} = \frac{\delta E_{xc}[n]}{\delta n(r)},$$

the set of N_e independent Kohn-Sham equations are given by:

$$\begin{cases} n = \sum_i \psi_i^* \psi_i \\ [-\frac{\hbar^2 \nabla^2}{2m} + V_H + V_{xc} + V_{ext}]\psi_i(r) = \epsilon_i \psi_i(r) \end{cases}$$

where each equation for $\psi_i(r)$ represents a non-interacting one particle system moving in a self-consistent effective potential containing the Hartree V_H, exchange correlation V_{xc}, and external V_{ext} potentials.

This set of equations can be efficiently solved recursively in a self-consistent way. Given a charge density $n(r)$, a new set of eigenstates can be found by solving the equation for $\psi_i(r)$, and a new charge density $n'(r)$ is constructed. This procedure is repeated until self-consistency is achieved. These equations thus open the door to the study of solid-state systems with efficient numerical methods.

2.2.1 Approximate exchange-correlation potential

In theory, the Kohn-Sham equations allows an exact calculation of the ground state of the system. However, the exact functional form of the exchange-correlation potential is not known and an approximation of $E_{xc}[n]$ is required.

The simplest approximation corresponds to the local density approximation (LDA) [15] in which the exchange-correlation energy per electron is assumed to depend on the value of the density and not, for example, on its derivatives:

$$E_{xc}^{LDA}[n] = \int \epsilon_{xc}^{LDA}[n(r)]n(r)dr.$$

Normally, the exchange-correlation density is assumed to be equal to the homogeneous electron gas density. The exchange-correlation is divided in two terms. The exchange part of the homogeneous electron gas can be obtained from the Hartree-Fock approach, and is given by:

$$\epsilon_x^{hom}[n] = -\frac{3}{4\pi}(3\pi^2 n)^{1/3}.$$

The correlation part $\epsilon_c^{hom}[n]$ is calculated with Quantum Monte-Carlo simulations of the homogeneous electron gas [16].

The LDA approximation works remarkably well for a wide variety of compounds, and is therefore the most commonly used in solid state simulations [17]. Compared to experimental values, typical systematic errors of LDA are within 1% for atomic positions and lattice constants, and around 5% for phonon frequencies [4]. The largest error is normally found in the underestimation of energy band gaps.

Several other approximations beyond LDA are available. For instance, the generalized gradient approximation (GGA) [18, 19] is developed to ameliorate the deficiencies of the LDA approach.

2.2.2 Density functional perturbation theory

Mechanical, dielectric and dynamical properties of the system can be obtained through first and higher-order derivatives of the total energy. Higher-order derivatives can be accessed through the frozen-phonon technique or through density functional perturbation theory (DFPT) [20].

The basic assumption behind DFPT is that quantities such as the wavefunction, electron density, or the external potential can be written as a perturbation series of the form:

$$X(\lambda) = X(0) + \sum_i \frac{\partial X}{\partial \lambda_i}|_0 \lambda + \frac{1}{2}\sum_{i,j} \frac{\partial^2 X}{\partial \lambda_i \partial \lambda_j}|_0 \lambda_i \lambda_j + \dots$$

where $X(\lambda)$ is a generic physical quantity, such as the Kohn-Sham orbitals $\psi_i(\lambda)$, the Kohn-Sham energy $E(\lambda)$, or the electronic charge density $n(\lambda)$, and λ is a small perturbation parameter. The variation in the Kohn-Sham orbitals may be determined by solving the so-called Sternheimer equation [21], which is obtained by expanding the Kohn-Sham equations to first order. In the case of insulators, the computational cost of determining the first correction to the Kohn-Sham orbitals is comparable to that required to solve the zero-order Kohn-Sham equations.

First-order derivatives of the total energy with respect to atomic positions, strain tensor and electric field determine respectively the forces on the atoms, the stress tensor and the spontaneous polarization. Second-order derivatives of the energy allow access

to the linear response of the solid through the force constant matrix, the Born effective charge tensor and the static dielectric tensor.

2.3 Structural and electronic properties

The theoretical background of density functional theory provides access to a number of experimental and theoretical physical quantities. In this section, structural and electronic quantities of special relevance for the present work are introduced, including the calculation of polarization and epitaxial strain diagrams.

Structural transitions from a reference to a distorted structure can be identified by unstable modes of the reference structure. The complete phonon diagram spectrum can be computed in the high symmetry phase through the force-constant matrix:

$$\Phi_{i\alpha,j\beta} = \frac{\partial^2 E}{\partial u_{i\alpha} \partial u_{j\beta}},$$

where $u_{i\alpha}$ represents the displacement of the i-th atom along the direction α. The n-th normalized eigenvector is denoted as $\xi^n_{i\alpha}$ and its eigenvalue as ω_n. Modes with real frequency $\omega^2 > 0$ are stable and correspond to local energy minimum with respect to that atomic displacement pattern. Modes with imaginary frequency $\omega^2 < 0$ are unstable and generate low symmetry distortion of the reference structure.

Born effective charges described the response of the charge density to local distortions, particularly those that create electric fields in the material. The Born effective charge matrix is defined as:

$$Z_{i,\alpha\beta} = \frac{\Omega}{e} \frac{\partial P_\alpha}{\partial u_{i\beta}},$$

where P_α is the polarization induced in the crystal by the displacement of the i-th atom in the direction β.

The dielectric susceptibility measures the polarizability of a dielectric medium in response to an applied electric field. The static dielectric tensor consist of electronic ϵ^{el} and ionic ϵ^{ion} contributions. The electronic contribution is given by:

$$\epsilon^{el}_{\alpha\beta} = \delta_{\alpha\beta} + 4\pi \left. \frac{\partial P_\alpha}{\partial \mathcal{E}_\beta} \right|_{u=0},$$

where P_α is the polarization induced by the electric field $\mathcal{E}_\beta$ with ions fixed. The ionic contribution ϵ^{ion} can be calculated from the force constant matrix $\Phi_{i\alpha,j\beta}$ and the Born effective charge matrix $Z_{i,\alpha\beta}$ as:

$$\epsilon^{ion}_{\alpha\beta} = \frac{4\pi e^2}{\Omega} \sum_n \frac{1}{\omega_n} Q^n_\alpha Q^n_\beta,$$

where the mode effective charge Q^n_α is defined as $Q^n_\alpha = \sum_{i\beta} Z_{i,\alpha\beta} \xi^n_{i\beta}$.

2.3.1 Polarization

The essential quantity in the description of ferroelectricity is the spontaneous polarization. However, given the continuous nature of the electronic charge density, the microscopic definition of polarization in periodic systems is an ambiguous concept. In the case of ferroelectric oxides, chemical bonds have a mixed ionic/covalent character, and therefore it is incorrect to define the polarization via the charge distribution [4].

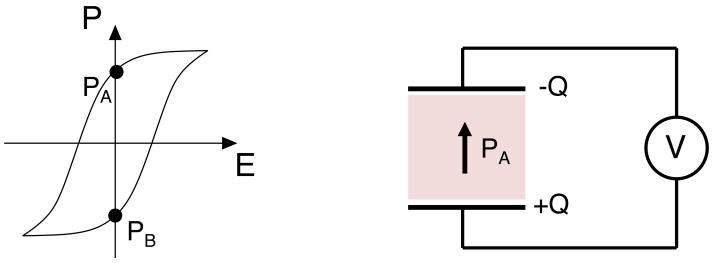

Figure 2.2: Polarization versus electric field hysteresis loop (left). Schematic representation of an experimental measurement of polarization (right).

Experimentally, the polarization of a ferroelectric material is computed from differences of macroscopic measurements. In a ferroelectric material, the spontaneous polarization displays the characteristic hysteresis loop shown in Fig. 2.2. If A and B denote the zero electric field polarizations, the spontaneous polarization is evaluated as $(P_A - P_B)/2$.

Experimentally, the polarization difference corresponds to the measured integrated macroscopic current $j(t)$ through the sample during a time Δt:

$$\Delta P = \int_0^{\Delta t} j(t) dt = P(\Delta t) - P(0),$$

where the initial and final states are normally associated with a centrosymmetric ($P(0) = 0$) and polar microscopic structure. Theoretically, the bulk sample between the conducting electrodes is simulated by a periodic infinite crystal, with zero external electric field. The total polarization P can be decomposed into ionic P_{ion} and electronic P_{el} contributions [4]:

$$P = P_{ion} + P_{el}.$$

The ionic part can be written as:

$$P_{ion} = \frac{e}{\Omega} \sum_i Z_i R_i$$

where Ω is the volume of the unit cell and Z_i is the charge of the ion i at position R_i. The electronic polarization part can be formulated as a Berry phase of the occupied bands:

$$P_{el} = -\frac{2ie}{(2\pi)^3} \sum_{n=1}^{N_b} \int_{BZ} \langle u_{nk} | \nabla_k | u_{nk} \rangle dk,$$

where N_b is the number of occupied electronic bands, u_{nk} is the lattice periodic part of the Bloch wavefunction $\Psi_{nk}(r) = u_{nk}(r)e^{ikr}$ and BZ denotes the Brillouin zone. This expression is the central results of the modern theory of polarization developed by King-Smith and Vanderbilt [22]. The expression is valid for an insulating path connecting initial and final states of the system and depends only on the final state.

It is very important to note that given that the atomic positions R_i are defined modulo a lattice vector R, the ionic polarization P_{ion} and total polarization P are defined modulo a quantum of polarization eR/Ω. However, typical magnitudes of the spontaneous polarization in ferroelectrics are less than 0.8 C/m^2 while the polarization quantum is on the order of 1 C/m^2 and therefore, the reference phase for the phase branch is usually easy to recognize. When ambiguity appears about the identification of the quantum factor, polarization can be computed between the nonpolar and polar structures, in order to identify discontinuous jumps in the path.

2.3.2 Epitaxial strain

The study of the mechanical constraint imposed by the substrate on thin films properties is an area of intensive research [23]. Complex oxides are strongly sensitive to the effect

of pressure and mechanical constraints. In particular, epitaxial strain has been shown to play an important role in the determination of ferroelectric properties of thin films and superlattices.

As shown in Fig. 2.3(a), experimental realization of epitaxial strain on a thin film or superlattices is achieved through coherent growth of the sample over a substrate. If the epitaxial growth is coherent, the in-plane atomic distances and in-plane cell dimensions are fixed to match the substrate, while the out-of-plane dimensions are free to relax.

The film thickness has an important role on the degree of coherence between thin film and substrate [24]. If the epitaxial strain is too large, the thin film grow coherently with the substrate until the elastic energy required to strain the film and match the substrate plane is equal to the energy required to create random misfit dislocations. Beyond this threshold thickness, dislocation and defects appear to reduce the strain and allow the structure to recover the bulk geometry with zero strain.

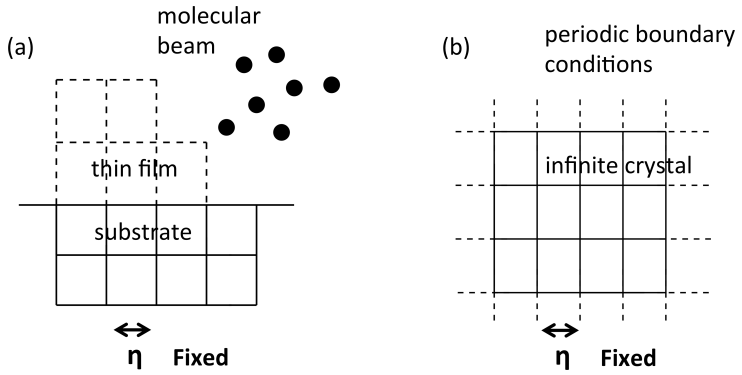

Figure 2.3: Schematic representation of (a) experimental coherent epitaxial growth of a material and (b) first principles calculation of an epitaxially strained crystal.

In first principles calculations, epitaxial strain is simulated in a uniform crystal through mixed mechanical boundary conditions: fixed in-plane strain and fixed out-of-plane stress. The matching plane, the in-plane lattice vectors as well as the in-plane unit cell shape are fixed to match the experimental geometry of the substrate, while the out-of-plane lattice vector is allowed to relax.

Experimental and theoretical studies have shown the important role of epitaxial strain in the stabilization of ferroelectricity in thin films [24]. In the particular case

of complex oxides, the magnitude of the thin film polarization can be enhanced or suppressed with respect to its bulk value depending on the value of the applied strain. The effect of epitaxial strain on antiferroelectricity will be the subject of chapter 5.

2.4 Practical implementations

Even with the powerful approximations introduced earlier, the Kohn-Sham equations require a couple more simplifications in order to be tractable numerically. These simplifications are briefly reviewed in this section.

2.4.1 Plane wave basis

The infinite crystal is constructed by imposing Born-Von Karman periodic boundary conditions:

$$\psi_{n.k}(r+R) = e^{ik\cdot R}\psi_{n.k}(r)$$

where R correspond to any vector in the direct space. The Bloch theorem [9] allows to write any wavefunction as the product of a plane wave and a lattice periodic function $u_n(k,r)$:

$$\psi_{n.k}(r) = \frac{1}{\sqrt{\Omega}} u_n(k,r) e^{ikr}$$

where Ω is the volume of the cell, k is a wave-vector in reciprocal space, and n is the energy band index. In practice, the periodic functions $u_n(k,r)$ are decomposed in a Fourier series as:

$$\psi_{n.k}(r) = \frac{1}{\sqrt{\Omega}} \sum_G C_{n,k}(G) e^{i(k+G)r}$$

where G represents any vector in reciprocal space.

In theory, the Fourier expansion requires an infinite number of plane waves. In practice, the plane wave expansion is truncated at a certain cut-off energy value E_{ecut} so that the kinetic energy satisfies:

$$\frac{\hbar^2}{2m}|k+G|^2 < E_{ecut}.$$

In order to optimize computational resources, the energy cut-off is chosen through a convergence test and so that total energy calculations are accurate below 1 meV/f.u.

2.4.2 Brillouin grid

The calculation of macroscopic quantities such as the energy and polarization involves the integration of the electronic charge density:

$$\rho = \sum_{n}^{N_b} \int_{BZ} d\vec{k} |\psi_{n.k}(r)|^2,$$

where $|\psi_{n.k}(r)|^2$ correspond to modulo squared Bloch functions, N_b is the number of occupied energy bands and BZ is the Brillouin zone. Integration over reciprocal space involves the knowledge of the Bloch functions over an infinite number of k points, and therefore a finite amount of k points must be selected for numerical calculations.

The most extensively used technique correspond to the k point sampling method developed by H. J. Monkhorst and J. D. Pack [25]. A small number of k points along lattice vector directions is selected based on symmetries of the system such as time reversal, inversion and space group symmetries. In practice, convergence studies are carried out to find the optimal number k points in the grid, so that the a small numerical error is achieved with a small amount of computational resources.

2.4.3 Pseudopotentials

The core electrons as well as the valence electrons close to the nucleus have rapidly varying wave functions in the central region of the nuclei. The correct description of these electrons requires a large number of plane waves, in clear conflict with the plane wave basis truncation.

The pseudopotential approach was design to solve this problem, for an introductory review see Ref. [26]. The electronic properties of molecules and solids are governed by the valence electrons, while the core electrons can be considered chemically inert and independent of the atomic environment. The pseudopotentials approximation replaces the core ionic potential with a fictitious potential such that the original potential, and the valence wave functions, remain unchanged beyond a certain cut-off radius and the rapidly varying functions inside the core region are replaced by smoothly varying functions.

In practice, a reference calculation is performed for the isolated atom including all the electrons. The analytical pseudotential is then fitted in order to reproduce the all-electron calculation. The cut-off radius is chosen so that constructed pseudopotential can be transferred to the solid or any other environment. The pseudopotential approximation decreases the number of plane waves involved in the Bloch expansion as well as the number of electrons considered in the Kohn-Sham equations, decreasing enormously the calculation time.

Different types of pseudotentials have been developed. In this work, norm conserving pseudopotentials are often adopted. These pseudopotentials are constructed to enforce the condition that the norm of each pseudo-wavefunction be identical to its corresponding all-electron wavefunction inside the cut-off radius. Another type of pseudopotential used in this work includes the projected augmented wave (PAW) method [28,29], which greatly improve the efficiency of the calculation.

2.4.4 Space group symmetries

One of the most important features of density functional implementations is the use of symmetries and space groups. Geometrical restrictions in the positions of the atoms and unit cell parameters allow the study of metastable structures, unaccessible experimentally. In this section, the notation for crystal structures and space groups is briefly reviewed, for details see Ref. [27].

A space group correspond to the group of all isometries under which the lattice and basis of the crystal are invariant in space. There are 230 space groups in three dimensions, which can be divided in one of the 7 crystal systems (distributing 32 point groups) or into 7 lattices systems (distributing 14 Bravais lattices).

The Hermann-Mauguin notation of space groups is the most commonly used. In this notation, the space group is denoted with a symbol including the lattice type and the point group. The first letter describes the centering of the Bravais lattice, which is given by one of the following in three dimensions: (P) primitive, (I) body centered, (F) face centered, (A) centered on A faces only, (B) centered on B faces only, (C) centered

on C faces only and (R) rhombohedral.

The next letters describe the point group symmetries, with the addition of glide planes and screw axis. The first lowercase letter describe the symmetry operation along the major symmetry axis of the crystal. The second lowercase letter denotes the symmetry along secondary axes. The third lowercase letter denote the symmetry along another symmetry axis.

Reflection planes, denoted as m in point group notation, can be replaced by a glide operation depending on extra symmetries present in the structure. For instance, the letters a, b, or c denote glide planes with translation along half of the face normal, while the letter n denotes a plane with translation along half of the face diagonal.

2.4.5 Software packages

All the results reported in this work are based on the theoretical and practical considerations presented in the previous sections. Different software implementations of density functional theory were used to perform calculations.

Complex oxides calculations were performed using version 7.4.1 of `ABINIT` package [30], the local-density approximation (LDA) and norm conserving pseudopotentials. The `ABINIT` package is an open source software, made under general public license GNU, which allows the user to access the source of the program and eventually modify it as well as to distribute it.

Nudge elastic band calculations, lattice entropy contributions, phonon frequencies and linear response calculations were performed with version 5.0 of `QUANTUM ESPRESSO` [31], the local-density approximation (LDA) and norm conserving pseudopotentials.

High-throughput screening of compounds were performed with version 5.3.2 of `VASP` package [32], the local spin density approximation (LSDA) plus Hubbard U method and projector augmented-wave pseudopotentials [28, 29]. The `VASP` package is very suitable for database methods, given the extensive library of pseudopotentials provided.

The `ISOTROPY` [33] software suite is a collection of applications for the analysis

of phase transitions in crystalline solids, including the identification of space group symmetries and structural distortions. Structural relationships between structures can be obtained with The Bilbao Crystallographic Server [34].

Chapter 3

Ferroelectricity and antiferroelectricity

In this chapter, the physics of ferroelectricity and antiferroelectricity is reviewed. Important microscopic and phenomenological models as well as important examples of ferroelectric and antiferroelectric materials are summarized. The relationship between these ferroic orders is highlighted throughout this chapter, and abridged in the definition of antiferroelectricity.

3.1 Ferroelectricity

Ferroelectricity is an extensively studied and well understood phenomena [3, 4]. Ferroelectric materials are characterized by a spontaneous and switchable polarization. Under the effect of an external electric field, the macroscopic polarization displays the characteristic hysteresis loop shown in Fig. 3.1. With increasing temperature, the polarization magnitude decreases and disappears at a critical temperature T_c, where the system undergoes a phase transition to a paraelectric phase. In ferroelectrics, the transition can be first or second order, producing a continuous or discontinuous transition at T_c respectively.

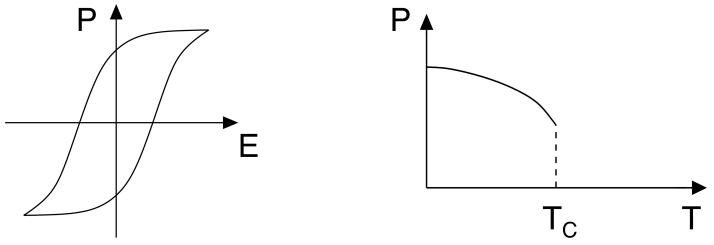

Figure 3.1: Characteristic ferroelectric hysteris loop (left). Macroscopic polarization as a function of temperature (right).

As introduced in section 2.3.1, the modern theory of polarization stipulates that

only differences of the macroscopic polarizations are physically meaningful. Microscopically, the spontaneous polarization is produced by the atomic arrangement of ions in the crystal structure, producing an asymmetrical distribution of positive and negative charges [35]. This charge asymmetry develops below the critical temperature by two different mechanisms. In some cases, local dipoles already exist at high temperature in such a way that the net polarization is zero, and the dipoles align below T_c to produce a net non-zero polarization. This is known as an order-disorder ferroelectric phase transition. If dipoles are not present at high temperatures and develop below T_c the ferroelectric phase transition is known as displacive. In general, ferroelectric phase transitions in oxides correspond to an intermediate case between these two extremes.

From a first-principles point of view, ferroelectric materials are characterized by a polar crystal structure. In a displacive transition, the polar structure corresponds to a small and continuous distortion of a reference structure, normally associated with the high-temperature paraelectric phase. The ferroelectric hysteresis loop is explained by the energy barrier separating different polarization orientations. Experimentally, the physics of ferroelectric switching includes extrinsic and macroscopic effects such as nucleation and domain wall motion [3].

Ferroelectric materials correspond to a subclass in the wider group of piezoelectric materials. Piezoelectric crystals develop a voltage under the application of an external stress. Among these, pyroelecric crystals develop a polar structure with a change in spontaneous polarization with decreasing temperature. Among these, those crystals that have a switchable polarization correspond to ferroelectric materials.

Ferroelectric and piezoelectric properties can be greatly enhanced by external effects. Traditional tunable parameters include isovalent substitution and compositional doping, pressure, epitaxial strain and size effects. The application of these techniques to antiferroelectrics is discussed in chapters 4 and 8.

3.1.1 Prototypical example

A large number of ABO_3 oxides compounds adopt the cubic perovskite structure shown in Fig 3.2. Atoms are assigned to high symmetry points of the cubic lattice, with atom A at the corner, atom B at the center, and oxygen O at the faces of the cube. The cubic perovskite structure has space group $Pm\bar{3}m$, and normally corresponds to the structure of the high-temperature paraelectric phase. When the temperature is lowered, perovskites undergo different types of polar and non-polar structural distortions depending on their chemistry, as discussed in section 4.

Barium titanate ($BaTiO_3$) is a prototypical ferroelectric. At the critical temperature $T_c = 393$ K, the cubic perovskite structure undergoes a phase transition to a tetragonal phase ($P4mm$) with a non-zero polarization $P \backsimeq 27\mu C/cm^2$. Microscopically, the low-temperature tetragonal phase is originated by the polar displacement of the titanium Ti^{+4} ion at the center of the octahedral cage, as shown in Fig 3.5.

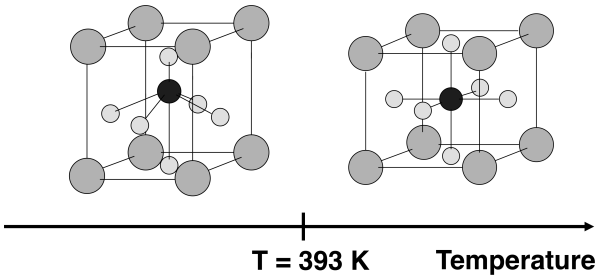

Figure 3.2: Cubic to tetragonal phase transition of $BaTiO_3$ as a function of temperature.

The symmetry-breaking relation between the cubic and tetragonal structures is consistent with a second order phase transition. Experimentally, the phase transition is weakly first order. This apparent inconsistency is resolved by the strong polarization-strain coupling of the material. Finally, temperature dependent models are able to reproduce the observed sequence of phase transitions [36,37], as described in section 3.2.3.

3.2 Microscopic models of ferroelectricity

The description of ferroelectric phase transitions is one of the most traditional fields in solid-state physics [3]. In this section, different approaches to describe structural phase transitions are reviewed.

3.2.1 Landau-Devonshire

Ferroelectric phase transitions can be described by Landau theory [35]. The equilibrium state of the system, at a given pressure and temperature, can be found by minimizing the free energy:

$$F = U - TS,$$

where T is the temperature, S is the entropy and U is the internal energy of the system.

The order parameter that describes the macroscopic state of the ferroelectric transition corresponds to the macroscopic polarization P. In accordance to Landau Theory, this physical quantity adopts a zero value in the high-symmetry paraelectric phase and becomes non-zero below the phase transition temperature.

The hypothesis of the Landau theory is that the free energy can be Taylor expanded around the transition temperature with respect to the order parameter, where only symmetry allowed terms are retained, and the expansion is assumed to remain valid above and below the phase transition temperature. In a simplified Landau-Devonshire description, the strain degrees of freedom are neglected, and the free energy of the ferroelectric system is given by:

$$F = \frac{1}{2}\alpha(T - T_c)P^2 + \frac{1}{4}\beta P^4 + \frac{1}{6}\gamma P^6,$$

where T is the temperature, T_c is the transition temperature, α, β and γ are temperature independent coefficients and the expansion is truncated at sixth order. From this expression, the internal energy and entropy of the system can be identified as:

$$U(P) = -\frac{1}{2}\alpha T_c P^2 + \frac{1}{4}\beta P^4 + \frac{1}{6}\gamma P^6 \qquad S(P) = -\frac{1}{2}\alpha P^2.$$

The coefficients of the polynomial expansion can be fitted to experiments or temperature dependent models.

In this Landau model, the coefficients α and γ are always positive, and the sign of the coefficient β determine the nature of the phase transition. As shown in Fig. 3.3, at $T > T_c$ the system is paraelectric, the free energy has a single well as a function of the polarization with solution $P = 0$.

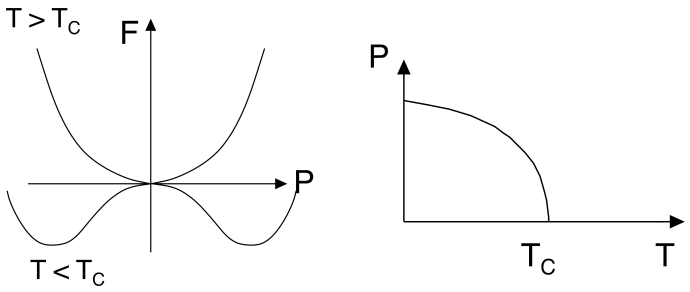

Figure 3.3: Evolution of the free energy (left) and polarization (right) as a function of temperature in a second-order transition.

If $\beta > 0$, the paraelectric to ferroelectric transition is second order. The free energy evolve continuously from a single well to a double well at $T = T_c$, and the spontaneous polarization P_0 of the material is given by the conditions:

$$\frac{\partial F}{\partial P} = 0 \quad \wedge \quad \frac{\partial^2 F}{\partial P^2} < 0 \quad \Longrightarrow \quad P_0 = \pm\sqrt{\frac{a}{b}(T_c - T)}.$$

The spontaneous polarization increases with decreasing temperature and vanish for $T > T_c$ as plotted is Fig 3.3(right). Furthermore, the dielectric susceptibility $\chi = (1/\epsilon_0)\partial P/\partial E|_{P_0}$ follows the Curie-Weiss behavior, given by:

$$\chi = \begin{cases} (a(T - T_c))^{-1} & T > T_c \\ (2a(T - T_c))^{-1} & T < T_c, \end{cases}$$

and diverges at $T = T_c$, consistent with the soft mode theory of ferroelectric transitions of section 3.2.2.

If $\beta < 0$, the paraelectric to ferroelectric transition is first order. The free energy develops two local minima at non-zero polarization values at a certain temperature T_0.

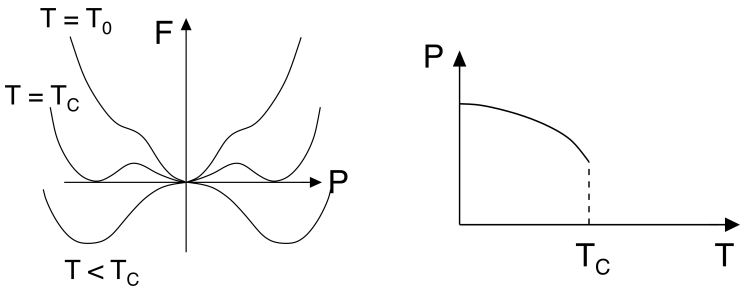

Figure 3.4: Evolution of the free energy (left) and polarization (right) as a function of temperature in a first-order transition.

Between T_0 and T_c ($T_0 > T_c$), the paraelelctric phase corresponds to the global minimum of the free energy. When the temperature is reduced, the polar phase become the most favorable phase below T_c. As a function of temperature, the polarization will display a discontinuous jump from the paralectric to the polar phase at T_c, as shown in Fig. 3.4.

3.2.2 Soft mode theory

The microscopic origin of ferroelectricity was the subject of intense investigation in solid-state physics. An important stimiluos for the theory of ferroelectricity came from the observation that ferroelectric transitions can be described in the framework of unstable modes.

In 1959, Cochran pointed out that at the second order ferroelectric transition there must be a transverse optical lattice vibration mode whose frequency goes to zero as the temperature is decreased. The soft mode freezes-in below the critical temperature and gives rise to a dipolar moment in the unit cell [38].

In the soft mode theory, a ferroelectric transition is characterized by a linear softening of the primary unstable mode with decreasing temperature. In the case of polar crystals, the frequencies ω_{LO} and ω_{TO} of the longitudinal and transverse optical phonons are different. The divergence of the dielectric susceptibility at the ferroelectric transition, predicted by the Landau theory, is related to the soft mode theory through the

Lyddane-Sachs-Teller relation [39]:

$$\frac{\omega_{LO}^2}{\omega_{TO}^2} = \frac{\epsilon}{\epsilon_\infty}$$

where $\epsilon = \epsilon_0 \chi$ is the static dielectric constant and ϵ_∞ is the high-frequency dielectric constant. In ferroelectric materials, ω_{TO} is anomalously small and ϵ anomalously large close to the transition temperature.

From a microscopic point of view, the temperature dependence of the soft mode arises from anharmonic couplings with other structural modes, giving rise to a renormalization of the harmonic frequency [3]:

$$\omega^2 = \omega_0^2 + \frac{k_B T}{2} \sum \frac{\alpha_i^4}{\omega_i^2} \tag{3.1}$$

where ω_0 is the harmonic frequency of the soft mode at $T = 0$, k_B is the Boltzmann constant and α_i is the anharmonic coupling coefficient of the soft mode with the mode i of frequency ω_i. The transition temperature T_c is the temperature where the frequency of the soft mode ω reaches zero. From Eq. 3.1 we deduce that:

$$T_C = -\frac{2\omega_0^2}{k_B \alpha},$$

where $\alpha = \sum_i \frac{\alpha_i^4}{\omega_i^2}$. The temperature dependence of ω can be rewritten in the following way:

$$\omega^2 = \omega_0^2 - \frac{\omega_0^2}{T_C} T = -\frac{\omega_0^2}{T_C}(T - T_C), \tag{3.2}$$

explicitly showing the linear relationship between the soft mode frequency and temperature, consistent with experiments.

3.2.3 Effective models

The functional properties of ferroelectrics are strongly dependent on temperature. The most accurate first-principles treatment of temperature is obtained with molecular dynamics simulations [12]. However, such approaches are computationally demanding and restricted to relatively small systems and time scales.

At the microscopic level, the effect of temperature can also be described by the first-principles effective Hamiltonian approach [40]. In this approach, a low order expansion

of the internal energy $U(\xi)$ is performed with respect to the most important degrees of freedom ξ governing the phase transition. Neglecting the effect of strain interactions, the internal energy has a typical double well shape:

$$U(\xi) = \frac{1}{2}a\sum_i \xi_i^2 + \frac{1}{4}b\sum_i \xi_i^4 + \frac{1}{4}c\sum_{ij}\xi_i^2\xi_j^2 + O(|\xi|^6), \tag{3.3}$$

where the coefficients a, b and c are determined from DFT calculations.

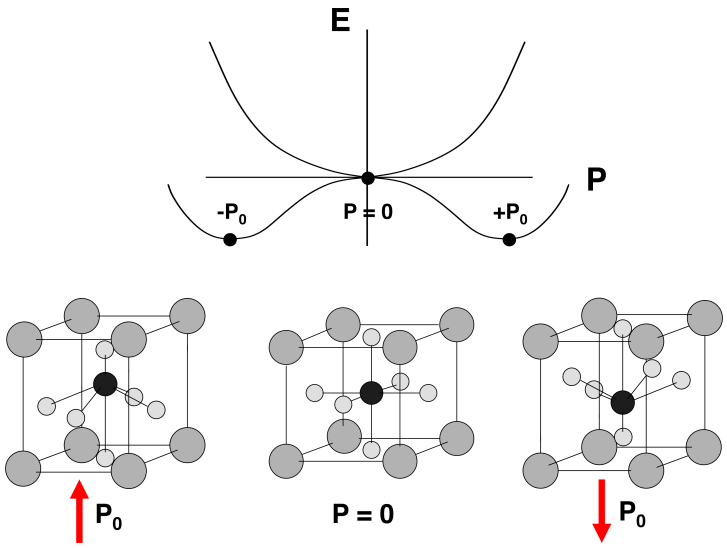

Figure 3.5: Doubel well potential describing the stabilization of the soft polar mode in a ferroelectric phase transition.

The connection between the microscopic and macroscopic descriptions is made by noticing that the coefficient a is proportional to the soft mode frequency ω^2 of Eq. 3.2. As shown in Fig. 3.5, the two stable states can be related to the equivalent up and down states of a polar mode or to the equivalent clockwise and counterclockwise angle of rotations in a antiferrodistortive mode. Assuming a uniform polar distortion, the free energy of Eq. 3.3 can be written as:

$$F(P) = -\frac{1}{2}\frac{\omega_0^2}{T_C}(T - T_C)P^2 + \frac{1}{4}b'P^4 + O(|P|^6),$$

consistent with the Landau-Devonshire model of ferroelectric phase transitions.

Monte Carlo simulations of effective Hamiltonians have been successfully applied to the study of ferroelectric perovskites oxides [36, 37]. The model is normally extended

to include the effect of strain η in the system $U(\xi, \eta)$, reproducing the right sequence and type of phase transitions.

Another important approach for the construction of effective Hamiltonians correspond to lattice Wannier functions [41]. In this approach the energy is again described as a Taylor expansion of the reference structure in term of selected degrees of freedom. However, in this case, the structural variable ξ is allowed to fluctuate between different unit cells. The decomposition of the system is not given by a homogeneous distortion throughout the entire crystal but by a local mode ξ associated to each unit cell. The parameters are fitted to the full unstable phonon branch and the local degree of freedom in each unit cell is interpreted as the lattice Wannier function associated to the unstable phonon branch. This method was applied to the case of antiferroelectric $PbZrO_3$ in Ref. [42].

3.3 Antiferroelectricity

Antiferroelectricity was introduced by Charles Kittel in 1951 [1]. In this work, Kittel proposed a material with chains of ions spontaneously polarized in opposite directions under no external field. As is schematically shown in Fig. 3.6, dipoles are formed below a certain critical temperature T_c, where two (or more) sublattices with equal and opposite polarization form, so that the total net polarization of the system is zero.

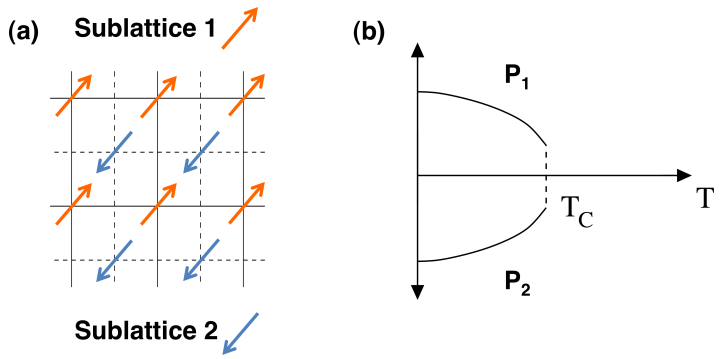

Figure 3.6: (a) Schematic representation of an antiferroelectric crystal. (b) Behavior of the macroscopic sublattices polarizations as a function of temperature.

As shown in Fig. 3.7, the application of an external field E align the dipoles and

increases the magnitude of the total polarization of the system. Dipoles pointing along the field increase their size, while dipoles pointing in the opposite direction decrease their size. At a certain critical field, one of the sublattices flips and aligns to the other, creating a uniform polar state.

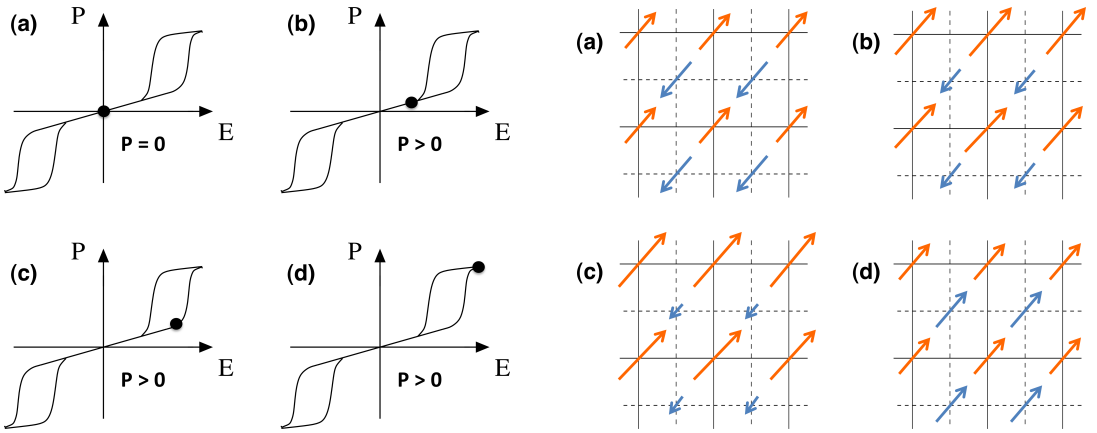

Figure 3.7: Behavior of the antiferroelectric system as a function of an electric field E. The initial (a), final (d) and intermediate states (b) and (c) of a field-induced transition are sketch with subllatices.

3.3.1 Kittel's model of antiferroelectricity

The macroscopic behavior of the antiferroelectric crystal is described by the Kittel model [1]. Assuming sublattices polarization P_1 and P_2, the free energy of the system shown in Fig. 3.6(a) is given by:

$$F = f(T)(P_1^2 + P_2^2) + h(P_1^4 + P_2^4) + gP_1P_2 - E(P_1 + P_2), \tag{3.4}$$

where $f(T) = g/2 + \lambda(T - T_c)$, T_c is the critical temperature, E is the external electric field and the coefficients g and h are positive constants. The coupling term gP_1P_2 favors the antipolar alignment of the sublattices polarizations. Other symmetry-allowed terms such as $(P_1P_2^3 + P_1^3P_2)$ and $P_1^2P_2^2$ are neglected for simplicity.

The macroscopic variables P_1 and P_2 are not thermodynamical quantities. Therefore, the Kittel model is mapped into a Landau-Devonshire functional using polar and antipolar variables $P = (P_1 + P_2)/\sqrt{2}$ and $Q = (-P_1 + P_2)/\sqrt{2}$ [43]. In these rotated

variables, Eq. 3.4 is written as:

$$F = (g + \lambda(T - T_c))P^2 + \lambda(T - T_c)Q^2 + \frac{h}{2}(P^4 + 6P^2Q^2 + Q^4) - \sqrt{2}EP.$$

From here it is clear that the temperature dependent form of $f(T)$ ensures the condensation of the variable Q below the critical temperature T_c. Similar to the case of ferroelectrics, the coefficients in the free energy can be fitted to experiments. In order to study the general behavior of the free energy, the following dimensionless variables [44, 45] are considered:

$$a = \frac{h}{2g^2}F \quad t = \frac{\lambda}{g}(T - T_c) \quad p^2 = \frac{h}{2g}P^2 \quad q^2 = \frac{h}{2g}Q^2 \quad e^2 = \frac{h}{g^3}E^2,$$

where a, t, p, q and e are the normalized free energy, temperature difference, polarization, staggered polarization, and electric field. Using these new variables, Eq. 3.4 is written as:

$$a = (1 + t)p^2 + tq^2 + p^4 + q^4 + 6p^2q^2 - ep. \tag{3.5}$$

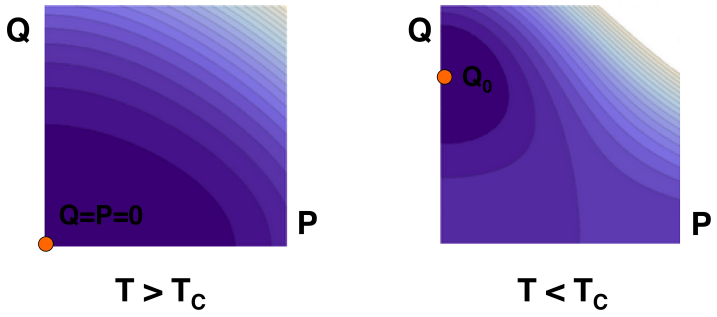

Figure 3.8: Paraelectric to antiferroelectric transition of the Kittel model. The orange point denote the global minimum. Above T_c the solution $P = 0$ and $Q = 0$ corresponds to the paraelectric phase, below T_c the solution $P = 0$ and $Q \neq 0$ corresponds to the antiferroelectric phase.

The state of the system can be described by contour energy profiles of the dimensionless free energy given by Eq. 3.5. Above the critical temperature ($t > 0$), the unique solution $P = 0$ and $Q = 0$ describes the paraelectric phase. Below the critical temperature ($t < 0$), Eq. 3.5 develops two solutions at $P = 0$ and $Q = \pm Q_0$, describing the antiferroelectric phase. As shown in Fig. 3.8, the sublattice polarization becomes

continuously non-zero ($Q \neq 0$ and $P = 0$) below T_c, increasing their magnitude with decreasing temperature.

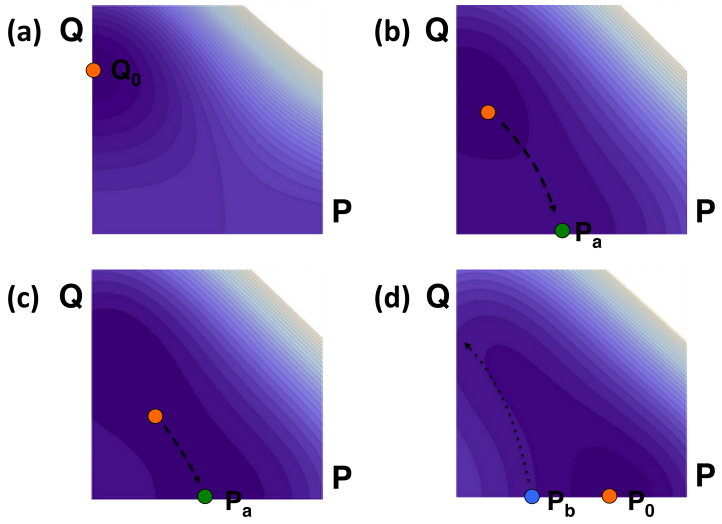

Figure 3.9: Field-induced transition from the antiferroelectric phase ($Q \neq 0$ and $P = 0$), to the ferroelectric phase ($Q = 0$ and $P \neq 0$). The energy profiles (a)-(d) correspond to the sequence of states shown in Fig. 3.8 (a)-(c). The global minimum is described by the orange point, while the ferroelectric metastable state is described by the green point. As described in the text, P_0 corresponds to the saturated induced polarization and P_b corresponds to the polarization at the back-switching point.

The effect of an external electric field is shown in Fig. 3.9. As the field is increased, the global minimum at $P = 0$ and $Q \neq 0$ becomes shallower and the local minimum at $P = P_a$ and $Q = 0$ becomes deeper. At the critical external field E_c, the minimum at $P = 0$ and $Q \neq 0$ disappear and the local minimum at $P = P_a$ and $Q = 0$ becomes the global minimum of the system. As the electric field is increased, the system reaches the saturation polarization at P_0. When the electric field is decreased, the system transforms back to the antipolar state at a different electric field E. The local polar minimum dissapear at $P = P_b$ and $Q = 0$, and the antipolar solution $P = 0$ and $Q \neq 0$ becomes the global minimum again. Integrating out Q from Eq. 3.5 shows that the discontinuous first-order transition originates from a renormalized negative coefficient in front of the P^2 term.

The Kittel model can be extended to first order transitions. Similar to the case of

ferroelectrics, the free energy expansion reads:

$$F = f(T)(P_1^2 + P_2^2) + h(P_1^4 + P_2^4) + j(P_1^6 + P_2^6) + gP_1P_2 - E(P_1 + P_2),$$

where $h < 0$ and $j > 0$ are temperature independent coefficients. The most important characteristics of a first order antiferroelectric transition correspond to the discontinuous jump of the sublattice polarizations at the critical temperature T_c. Finally, the Kittel model can be extended to include the effect of strain in the staggered polarization. A simple model including hydrostatic pressure and volume change was introduced in Ref. [46].

3.3.2 Definition of antiferroelectricity

The macroscopic model introduced by Kittel established important characteristics of antiferroelectric crystals such as their electrical behavior and response to mechanical effects. However, the identification of antiferroelectricity in real materials is more subtle and require further discussion. In this section, the difficulties in formulating a precise definition of antiferroelectricity are reviewed.

Antiferroelectricity is traditionally defined as a nonpolar phase obtained by the condensation of an antipolar lattice mode, which exhibits a large dielectric anomaly near the transition temperature and is transformed to an induced ferroelectric phase by the application of an electric field [3]. In practice, the identification of antiferroelectric materials through structural and dielectric measurements is challenging. The characteristic double hysteresis loops are typically observable in a narrow temperature range or under particular chemical and mechanical conditions.

Other approaches define antiferroelectricity based on the microscopic analogy to antiferromagnetism. In this case, the formulation of the staggered polarization require the identification of localized polarized ions on two or more symmetry-related sublattices. In this case, the modern theory of polarization arises the issue of the identification of local electric dipoles. These microscopic models tend emphasize the role of electrostatic dipole-dipole interactions and neglect short-range interactions, which have a

dominant role in the case of antiferrodistorted perovskites with centrosymmetric crystal structures [37]. As is discussed in section 3.4, a simple antipolar interaction between dipoles does not produce the characteristic double hysteresis. Polar intra-sublattice interactions are necessary to stabilize the sublattice polarization and produce the field-induced first-order transition.

The importance of an energetic criterion between the competing antiferroelectric and ferroelectric phases was first pointed out by G. Shirane [2, 47]. Antiferroelectric materials are defined as an antipolar crystal whose free energy is comparable to that of the polar crystal obtained by aligning the sublattice polarizations. The importance of both structural and energetic aspects in the definition are made clear by the Kittel model, where particular values of the parameter are required to obtain a structural transition with a low energy ferroelectric phase.

However, as pointed out by Levanyuk [48], the Landau functional derived from Kittel model is not specific to an antiferroelectric, and describes any system with a nonpolar structural transition. More specifically, any system with a nonpolar structural transition, described by a order parameter η, will have the generic coupling term $\eta^2 P^2$ that gives rise the double hysteresis loop and the dielectric anomalies of the Kittel model.

A precise definition can be proposed on the basis of soft mode theory. The connection between the microscopic and macroscopic behavior of antiferroelectrics starts with the identification of unstable modes in the relevant high symmetry reference structure. In the simple case, a Kittel type antiferroelectric has a single antipolar lattice mode, in which the atoms are divided in symmetry-related lattices with equal and opposite displacements. In the general case, other structural modes can be induced in the antiferroelectric phase through anharmonic couplings, producing more than two sublattices and either collinear or noncollinear sublattice polarizations. As is discussed in chapter 4, this is the situation observed in antiferroelectric perovskites, where the ground state is characterized by complex patterns of oxygen octahedron rotations and a cell-quadrupling antipolar modes.

The other key ingredient is the existence of a low-energy alternative ferroelectric phase, which is assumed to be obtained from the same reference structure. In the case of a simple Kittel type of antiferroelectric, this is described by including in the model the single polar mode, obtained by reversing the local dipole moments. In the general case, the ferroelectric phase could be generated by a general zone-center polar mode, and can be accompanied by other coupled modes either present or not present in the antiferroelectric phase. The relation between the polar mode and the primary unstable antipolar mode can be more complex than the simple alignment of ionic displacements. In particular, the direction of the polar mode could be independent of the directions of the sublattice polarizations.

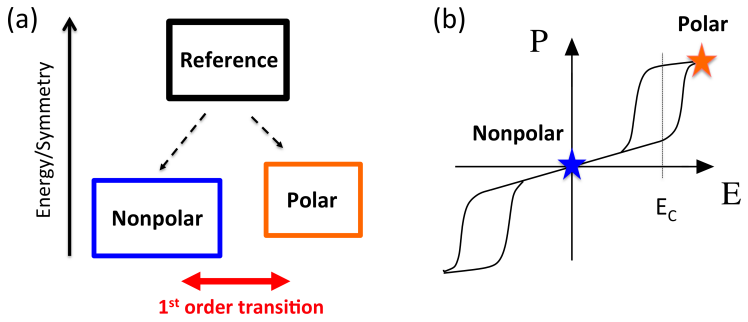

Figure 3.10: (a) Diagrammatic definition of an antiferroelectric crystal. (b) Characteristic antiferroelectric double-hysteresis loop.

The schematic definition in Fig. 3.10 (a) [4] recognizes the antipolar character of materials as a continuum. Kittel type two sublattice systems correspond to an extreme where polar and antipolar instabilities are related or belong to the same phonon branch. At the other extreme are cases where the relation between nonpolar and polar structures is not clear, and the two competing structures are merely distortions of the same reference structure with a small energy difference between them. All the cases in between display macroscopic properties characteristic of antiferroelectrics and are therefore included.

An antiferroelectric [5] is like a ferroelectric in that its structure is obtained through distortion of a nonpolar high-symmetry reference structure; for ferroelectrics the distortion is polar, while for antiferroelectrics it is nonpolar. However, not all nonpolar

phases thus obtained are antiferroelectric; in addition, there must be an alternative ferroelectric phase obtained by a polar distortion of the same reference structure, close enough in free energy so that an applied electric field can induce a first-order phase transition from the antiferroelectric to the ferroelectric phase, producing the characteristic polarization-electric field double-hysteresis loop shown in Fig. 3.10 (b).

This definition does not emphasize the structural conditions among the competing structures, but rather the small energy difference between them. This definition of antiferroelectricity can be used to search for new antiferroelectric materials through high-throughput methods. Simingly unrelated nonpolar and polar structures can be identified through the unstable modes of high-symmetry structures. First principles calculations can then be used to calculate the energy difference between these structure and select specific candidates for further experimental investigation.

3.4 Microscopic model of antiferroelectricity

In this section, a microscopic model of antiferroelectricity is constructed. Assuming an identification of local dipoles and sublattices polarization, the antipolar and polar interactions within the crystal are studied. The neccesary conditions that give rise to the field-induced first-order transition and the double hysteresis loops are investigated.

An array of electric dipoles labeled by p_i at site i is considered. As shown in Fig. 3.11, each dipole is characterized by an internal potential energy $\mathrm{U}(\mathrm{p}_i)$ associated with flipping the dipole between the up and down states and an interacting energy J_{ij} with a neighboring dipole p_j. The Ising-type Hamiltonian of the system can be written as:

$$H = \sum_{ij} J_{ij} p_i p_j + \sum_i U(p_i),$$

where the first sum will run over the nearest and next nearest neighbors, and the second sum will run over all sites of the lattice. The array of microscopic dipoles in the material is further assumed to be decomposed into two sublattices, and define macroscopic polarizations P_1 and P_2 for each of them.

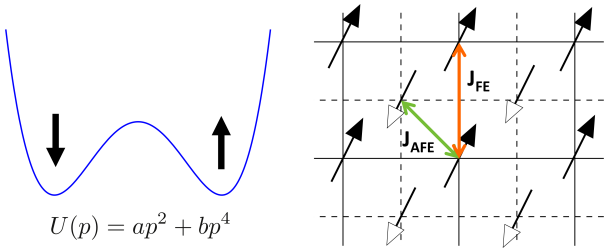

Figure 3.11: Weiss molecular model of antiferroelectricity. (a) On-site potential energy U(p) of the dipole. (b) Antipolar J_{AFE} and polar J_{FE} couplings coefficients for nearest and next-nearest neighbor interaction.

Given a dipole p, the nearest neighbor and next nearest neighborgh interactions define two sublattices in the system. Including an applied electric field E, the energy of a single dipole in each sublattice is given by:

$$H_1(p) = U(p) + J_{AFE}P_2p + J_{FE}P_1p - Ep$$

$$H_2(p) = U(p) + J_{AFE}P_1p + J_{FE}P_2p - Ep$$

where $J_{AFE} > 0$ represents the antipolar interaction between the dipole and the complementary sublattice and $J_{FE} < 0$ represents the polar interaction of the dipole with the sublattice that contains it. The simplest model is obtained by assuming a double well potential energy for the flipping of the dipole: $U(p) = ap^2 + bp^4$, where the coefficients $a < 0$ and $b > 0$ are temperature independent constants. The collective quantum interaction of all the dipoles within one sublattice are modeled by constructing the free energies of each sublattice:

$$F_i = -\log\left(\int_{-\infty}^{\infty} e^{-\beta H_i(p)}dp\right) \qquad i \in \{1, 2\},$$

where $\beta = (k_BT)^{-1}$, T is the temperature and k_B is the Boltzmann constant. From here, the macroscopic polarization field of each sublattice is recovered through the self consistent equations:

$$P_1 = \frac{1}{\beta}\frac{\partial F_1}{\partial E} \qquad P_2 = \frac{1}{\beta}\frac{\partial F_2}{\partial E}, \tag{3.6}$$

where the total macroscopic free energy of the system is given by $F = (F_1 + F_2)/2$ and the total polarization is obtained as $P = \partial F/\partial E$. For convenience, we define the function:

$$G(x) = \frac{\int_{-\infty}^{\infty} pe^{\beta(U(p)-xp)}dp}{\int_{-\infty}^{\infty} e^{\beta(U(p)-xp)}dp}$$

so that the set of equations 3.6 describing the system can be written in a compact form as:

$$P_1 = G(-J_{AFE}P_2 + J_{FE}P_1 + E) \qquad P_2 = G(-J_{AFE}P_1 + J_{FE}P_2 + E) \tag{3.7}$$

First, the behavior of the system is studied at high temperature and under no external field $E = 0$. In this case, $P_1 = P_2$ and the system of equations 3.7 reduces to the fix-point equation $P = G(-(J_{FE} + J_{AFE})P)$, which can be solved graphically by intersecting $P_2 = G(P_1)$ with the straight line of equation $P_2 = P_1$. At high temperatures there is only one solution $P_1 = P_2 = 0$, representing the paraelectric phase. As the temperature is decreased, two additional solutions appear below a certain critical temperature T_c, as shown in Fig. 3.13 (a). These two new solutions are equivalent and represent the antiferroelectric phase with $P_1 = -P_2$. In the antiferroelectric state the net polarization is $P = 0$ and $Q = (P_1 - P_2)/2$ measures the magnitude of the staggered polarization. The magnitude of the sublattice polarizations and critical electric field as a function of temperature are shown in Fig. 3.12 (a) and (b), respectively.

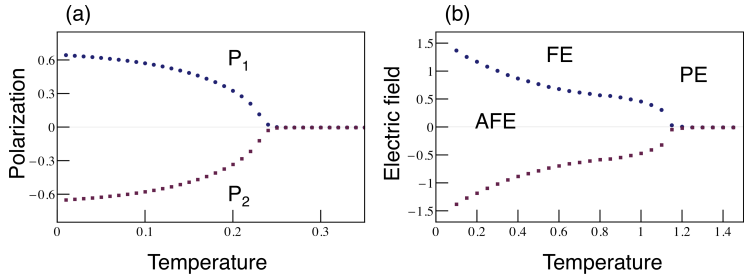

Figure 3.12: Paraelectric to antiferroelectric transition as function of temperature. Sublattice polarizations are denoted P_1 and P_2.

Next, the behavior of the system is considered under an external electric field E. In this case, Eqs. 3.7 are solved at a fixed temperature T. The magnitude of the sublattice polarizations as a function of the electric field E are shown in Fig. 3.13 (a)-(f). For typical values of $J_{AFE} = 0.1$ and $J_{FE} = 1.0$, the two equations intersect at multiple points depending on the value of the electric field. These points represent different phases and can be classified as: paraelectric at $P_1 = P_2 = 0$, ferroelectric $P_1 = P_2$, antiferroelectric $P_1 = -P_2$ and uncompensated antiferroelectric $P_1 \neq -P_2 \neq 0$. These solutions are separated by unstable saddle points. At zero external electric field, the

paraelectric (PE), ferroelectric (FE) and antiferroelectric (AFE) solutions are shown in Fig. 3.13 (a). When an external electric field is applied, one sublattice polarization increases while the other decreases, giving rise to uncompensated antiferroelectric solutions, denoted as U-AFE in Fig. 3.13 (b). At a critical electric field $E_C \backsimeq 1.2$, the uncompensated antiferroelectric solution disappear and the system transforms to the ferroelectric solution shown in Fig. 3.13 (e).

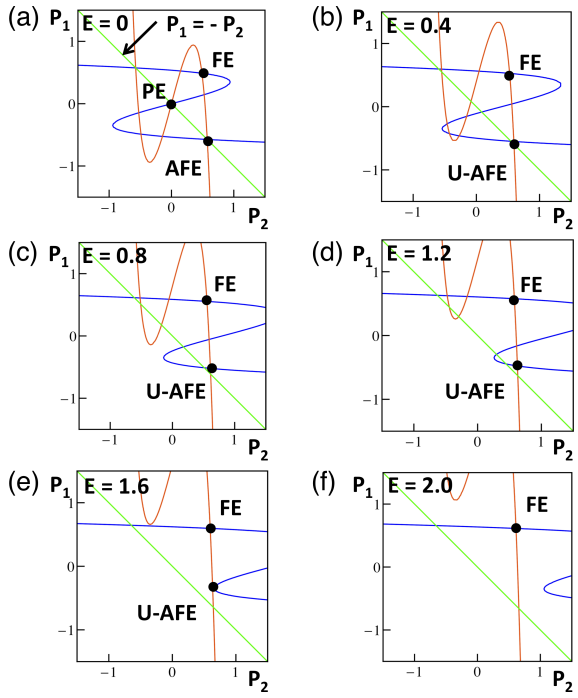

Figure 3.13: Field induced transition from the antiferroelectric (AFE) phase to the ferroelectric (FE) phase. The blue and orange line correspond to Eqs. 3.7, while the green line corresponds to $P_1 = -P_2$. Panels (a)-(f) show the evolution of the sublattice polarizations as a function of the electric field (E), the intersection of the blue and orange lines corresponds to the different paraelectric, ferroelectric, ferrielectric and antiferroelectric states of the field-induced transition.

The magnitude of the polarization P as a function of the external electric field E is shown in Fig. 3.14 (a). The antiferroelectric solution is depicted in red (squares) and the ferroelectric solution is depicted in blue (circles). The transformation from the uncompensated antiferroelectric solution to the polar solution at the critical electric field E_C is depicted by the jump in polarization ΔP. The state of the system is determined by the state with minimum free energy as a function of the external electric field, as shown in Fig. 3.14 (b).

The magnitude of the polarization discontinuity ΔP at the critical field depends on the magnitude of the coefficients J_1 and J_2. As the ferroelectric interaction within the same sublattice is decreased $J_2 \ll J_1$, the transition becomes smooth and $\Delta P = 0$. If the ferroelectric and antiferroelectric interactions have a similar magnitude $J_2 \sim J_1$, the transition becomes discontinuous and $\Delta P \neq 0$.

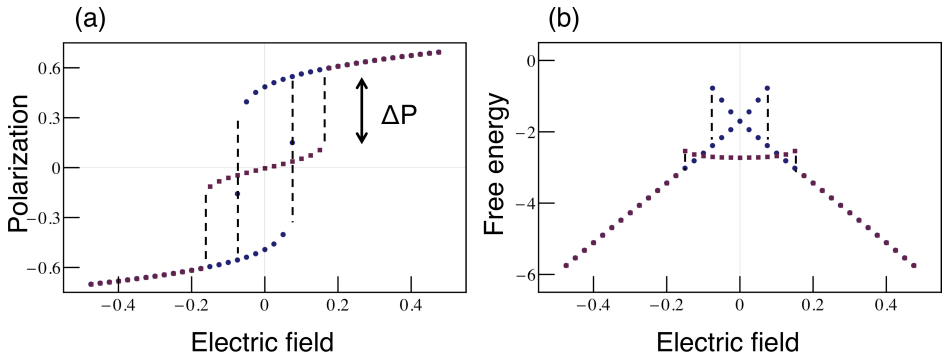

Figure 3.14: Field induced antiferroelectric to ferroelectric transition. (a) Polarization and (b) free energy versus electric field. The blue and red doted lines correspond to the ferroelectric ($P_1 = P_2$) and antiferroelectric ($P_1 = -P_2$) solutions of Eqs. 3.7.

Therefore, the absence of polar interactions between the complementary sublattice is an important condition for the appearance of the double hysteresis and the first order transition at the critical electric field. This result highlights the importance of the alternative competing ferroelectric phase in any antiferroelectric crystal. Finally, it is noticed that hysteresis is obtained in the polarization versus electric field graph if a triple well potential is used for the internal energy instead of the double well shown in Fig. 3.11 (a). The discontinuous first order transition at the critical electric field is therefore a consequence of polar and antipolar interactions and not of the potential energy used in the model.

3.5 Antiferroelectric materials

Perovskites antiferroelectrics

Pure antiferroelectric perovskites are rare but well documented [7]. As opposed to ferroelectric perovskites, antiferroelectric perovskites consists of rather complex structures with simultaneous distortions of the reference cubic structure. Typically, the antiferroelectric ground state structure is formed by a combination of oxygen octahedral rotations and antipolar displacements of the A-site cations. The structural and energetic origin of antiferroelectricity in pure perovskites is investigated in chapter 4

The compositional-substitution phase diagrams of $PbZrO_3$ and lead-free antiferroelecrtics has been the subject of intensive research for piezoelectric applications. The competition between ferroelectricity and antiferroelectricity has been studied in the (Pb,Sr)ZrO_3 [47] and (Sr,Ca)TiO_3 [49] systems.

More recently, antiferroelectric double hysteresis loops have been observed in rare-earth substituted (RE_xBi_{1-x})FeO_3, with RE: Sm, Gd, Dy [50]. At room temperature, a structural transition from the rhombohedral ferroelectric phase of $BiFeO_3$ to an orthorhombic phase is observed with decreasing average ionic radii of the A-site cation. At the phase boundary, the orthorhombic phase exhibits double hysteresis loops and enhancement of electromechanical properties independent of the rare earth dopant species.

Double perovskites

Antiferroelectricity has been identified in several double perovskite compounds. The degree of cation disorder is a characteristic feature of double perovskites [51]. Cation disorder generally leads to relaxor behavior, while ordered system display normal ferroelectric or antiferroelectric behavior depending on the degree of coherence. An antiferroelectric phase, isostructural to the low-temperature ground state of $PbZrO_3$, has been observed in $Pb(In_{1/2}Nb_{1/2})O_3$ [52]. A phase sequence from paraelecric to antiferroelectric and to a low-temperature ferroelectric has been observed for a number of

double perovskites such as $Pb(Co_{1/2}W_{1/2})O_3$ and $Pb(Sc_{1/2}Ta_{1/2})O_3$ [53] and in non-lead containing compounds [7].

Other antiferroelectrics

For completeness, a couple of other oxides are mention where antiferroelectricity has been proposed. Indium manganese oxide ($InMnO_3$) has a paraelectric phase at high temperature, an antipolar structure between 950^oC and 750^oC and a ferroelectric phase below 550^oC [54]. The intermediate antipolar structure consists of antipolar displacements of In ions and small octahedral rotations. Antiferroelectricity in this compound can be presumed due to its proximity to the low-temperature ferroelectric phase. First principles calculations show a small energy difference between the polar and antipolar structures of $InMnO_3$, characteristic of antiferroelectricity [55].

Double hysteresis loops have been observed in thin-film zirconia (ZrO_2) [56]. Zirconia and Hafnia correspond to extensively investigated high-k dielectric materials with a wide range of technological applications. Surface effects inhibits the monoclinic ground state of ZrO_2 and promotes the competition between the intermediate tetragonal structure and a metastable orthorhombic ferroelectric phase. The new functionality displayed by ZrO_2 is the subject of first principles investigations in chapter 7.

3.5.1 Functional properties

Traditional functional properties such as ferromagnetism, ferroelectricity and piezoelectricity arise from a coupling between the relevant order parameter and its conjugated macroscopic field. Potential applications of antiferroelectric materials are less clear, because the antiferroic order parameter does not couple directly to a macroscopic field, but rather to a microscopic staggered field.

However, the field-induced antiferroelectric transition is a source of promising technological applications. In systems where the antiferroelectric and ferroelectric phases have different volumes, the abrupt change in polarization at the first order transition can be accompanied by a large nonlinear strain response [57]. The intensive research

interest on lead-free piezoelectric ceramics, has motivated the search of lead-free antiferroelectrics.

The large piezoelectric effect at the field-induced transition enable applications in high-strain actuators and transducers, force generators and electrostrictors. One application corresponds to the piezoelectronic transistor [58] shown in Fig. 3.15 (a). The application of an eternal voltage produces a large expansion of the piezoelectric material, compressing a piezoresistor against the high strength medium. The piezoresistor undergoes a metal-insulator transition, allowing a current through the device. The ideal antiferroelectric material requires a small critical electric field, large stain variation and large dielectric constant. The absence of depolarization fields in antiferroelectrics suggest a better performance in scaled devices compared to traditional ferroelectric based piezoelectric materials.

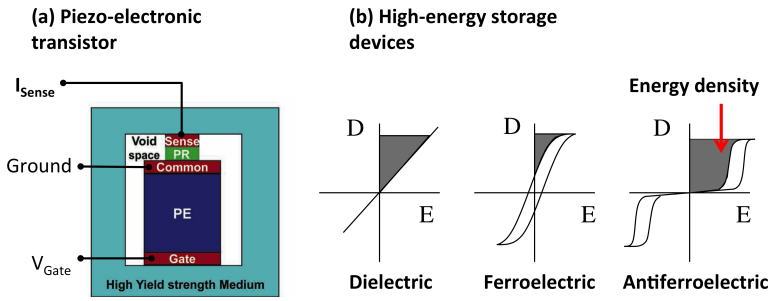

Figure 3.15: (a) Schematic of the piezo-electronic transistor. (b) Characteristic D-E measurements for a normal dielectric, ferroelectric and antiferroelectric. Figures from Refs. [58] and [6], respectively.

Other properties of antiferroelectric materials include large dielectric anomalies at the antiferroelectric-paraelectric transition temperature, large electrostriction coefficients and a giant electrocaloric effect [59]. Proposed applications include sensors, energy and charge storage devices, voltage regulators and electro optic devices.

The relevance to high-density energy storage applications comes from the shape of the double hysteresis. Antiferroelectrics are characterized by a small dielectric constant below T_c and a large capacitance response at high electric fields, suggesting a large energy density $W = (1/2)\int \vec{E} \cdot \vec{D} dD$. In this case, the use of ceramics requires small hysteresis and small volume variations at the transition. Large

values of energy densities have been obtained for La doped $Pb(Zr,Sn)O_3$ ceramics $W = 13.7$ J/cm^3 [60], equivalent to the best performance obtained with linear dielectric such as PVDF $W = 19$ J/cm^3 [61].

The application of antiferroelectric materials in real devices requires the optimization of a number of properties such as the operating temperature, critical field, strain change, switching time and reversibility. Tuning of functional properties has been explored extensively studied in La and Nb doped $Pb(Ti,Zr,Sn)O_3$ and in lead-free antiferroelectrics systems such as $(K,Ag)NbO_3$ and $(K,Na)NbO_3$ [7].

Chapter 4

Antiferroelectric perovskites

In this chapter, the physics of antiferroelectricity is reviewed in the perovskite family of compounds. The structures of specific antiferroelectric materials are described, emphasizing the differences between antiferroelectricity and antiferrodistortive phases with linear dielectric behavior.

The scarcity of pure perovskites compounds displaying antiferroelectricity leads to the natural question of why are there so few antiferroelectric perovskites? Based on first principles calculations, the microscopic structural origin of antiferroelectricity is investigated in the perovskite family of compounds. The search of more antiferroelectric perovskites is left for chapter 8.

4.1 The physics of ABO_3 perovskites

A large number of ABO_3 oxides compounds adopt the cubic perovskite structure shown in Fig 4.1 (left). The wide range of phenomena displayed by these compounds includes ferroelectricity, ferromagnetism, piezoelectricity, colossal magnetoresistance, superconductivity and metal-insulator transitions. The versatility of the ABO_3 perovskite structure is characterized by a high tunability of the ground state. Mechanical, electrical and chemical perturbations have a strong effect in the perovskite structure producing a rich variety of structural phase diagrams with important functional properties.

Ferroelectricity has been widely studied in perovskite oxides [3, 4]. Perovskite have a well known tendency to form polar distortions originated by the zone center polar mode shown in Fig. 4.1 (right). For example, $BaTiO_3$ undergoes a sequence of ferroelectric phase transitions with decreasing temperature, from cubic to successively:

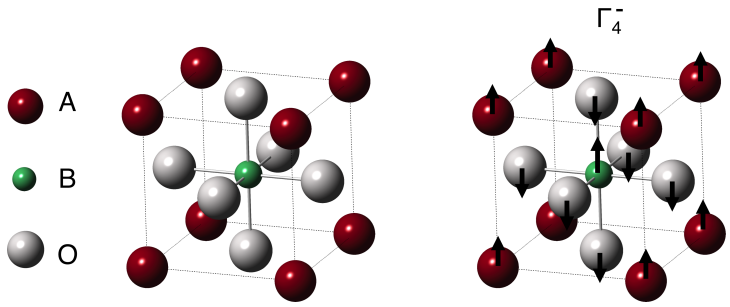

Figure 4.1: (left) Cubic perovskite structure. ((right) Representation of the zone-center Γ_4^- mode. This polar mode originates ferroelectricity in the perovskite family of compounds.

tetragonal ($T_C \backsimeq 130^o$C), orthorhombic ($T_C \backsimeq 0^o$C) and rhombohedral ($T_C \backsimeq -80^o$C). The microscopic origin of the structural transition can be explained by the displacement of the titanium Ti atom against the oxygen cage along the $\langle 001 \rangle$, $\langle 011 \rangle$ and $\langle 111 \rangle$ cubic directions, and a small change of shape of the unit cell.

Antiferrodistortive distortions consist of nonpolar displacements of the oxygen atoms in the perovskite structure. These distortions leave the shape and volume of the octahedron unchanged, and are interpreted as oxygen octahedron tilting. The simplest example corresponds to strontium titanate ($SrTiO_3$). $SrTiO_3$ has a single phase transition from the paraelectric cubic perovskite phase to a non-polar antiferrodistortive ground state ($T_C \backsimeq 100$ K). The low temperature phase of $SrTiO_3$ has a nonpolar tetragonal structure, which arises via oxygen octahedron rotations around the tetragonal axis. Dielectric measurements suggest a ferroelectric phase transition at very low temperatures. It has been demostrated that the metastable ferroelectric phase of $SrTiO_3$ is suppressed by quantum fluctuations [62], and therefore $SrTiO_3$ is an incipient ferroelectric.

The competition between polar and antiferrodistortive modes is explained by a delicate balance between short-range and long-range interactiones. While short-range ionic interactions tend to keep the atoms in their high-symmetry positions, long-range dipolar forces tend to destabilize the cubic structure and form polar structures [63]. The tendency of ABO_3 perovskites to be either ferroelectric or antiferrodistortive can be estimated using the Goldsmith tolerance factor:

$$\tau = \frac{R_A + R_O}{\sqrt{2}(R_b + R_A)},$$

where R_A, R_B and R_O correspond to the ionic radii of the A, B and oxygen ions in the cubic structure. Perovskites with tolerance factor > 1 tend to be ferroelectric (e.g. $BaTiO_3$), while a tolerance factor < 1 usually implies an antiferrodistorive phase with oxygen octahedron tiltings (e.g. $SrTiO_3$). However, this two type of distortions are not neccessarily exclusive and some perovskite compounds combine both of them.

Antiferroelectrc perovskites are characterized by an antipolar displacement of A-site cations, accompanied by a rather complex antiferrodistortive structures. As it is shown later, the antipolar zone-boundary mode is typically unstable in the cubic reference structure and have a strong coupling with oxygen octahedron rotations. As opposed to the case of $SrTiO_3$ and as is emphasized in section 4.3, antiferroelectric perovskites such as $PbZrO_3$ and $NaNbO_3$, have a very small energy difference between the nonpolar and mestastable polar phase, which is the key requirement of antiferroelectricity.

4.1.1 Glazer notation

In order to describe the structure of antiferroelectric perovskites, a special notation for oxygen octahedron rotations is introduced. Octahedral rotations are the most common antiferrodistortive distortions among perovskites. As shown in Fig. 4.2, oxygen octahedron rotations are classified according to their different tilting patterns [64–67].

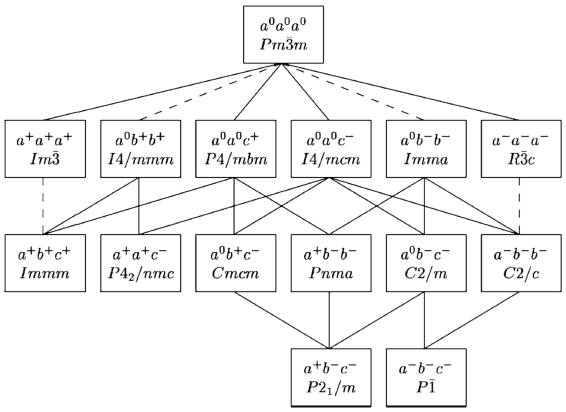

Figure 4.2: Group subgroup relationsip between the 15 possible octahedral tilting patterns. Solid lines represent second order transitions, while dashed lines represent first order transitions. From Ref. [65].

In Glazer notation [64], octahedral tilting is reported around each of the three axis

describing the array of octahedra. If succesive oxygen octahedron planes rotate in the same direction (in-phase) along a certain axis, a + sign is assigned to that axis. If succesive oxygen octahedra planes rotate in opposite directions (out-of-phase) along a certain axis, a − sign is assigned to that axis. If no rotation is present, the number 0 is assigned. The relative magnitude of the rotation is denoted by the letters a, b or c. The same letter is assigned for rotations axis with equal rotation ampltiudes.

4.1.2 Technical details

In this section, density-functional theory (DFT) calculations are performed using version 7.4.1 of `ABINIT` [30] package. The local-density approximation (LDA), a plane-wave energy cutoff of 680 eV, and a Monkhorst-Pack sampling of the Brillouin zone [25] are used for all structural optimizations. Norm-conserving pseudopotentials from the Bennett-Rappe library [68] are used, generated by the `OPIUM` code [108].

For selected compounds, phonon calculations and nudged elastic-band calculations were performed with `QUANTUM ESPRESSO`. The local-density approximation (LDA), a plane-wave energy cutoff of 680 eV and norm-conserving pseudopotentials are used in these calculations. Accurate energy differences are compared to density-functional theory (DFT) calculations performed using version 5.2 of `VASP` [32] package. The local-density approximation (LDA) and the generalized gradient approximation (GGA) are applied with the projected augmented wave (PAW) pseudpotentials provided by `VASP`.

4.1.3 Ferroelectric and antiferrodistortive distortions

In this section, the most common structural distortions displayed by perovskites are described. The phonon dispersion diagrams of relevant perovskites in their high temperature cubic perovskite structure are calculated. The results are in qualitative agreement with previous calculations [4, 69, 70].

Barium titanate $BaTiO_3$

The well known instabiltity at the Γ point [69] corresponds to vibrations of the Ti titanium against oxygen atoms. The associated polar displacement pattern, shown in Fig. 4.1, has Γ_4^- symmetry and originates the experimental ferroelectric phases: tetragonal (*P4mm*), orthorhombic (*Amm2*) and rhombohedral (*R3c*), mentioned earlier.

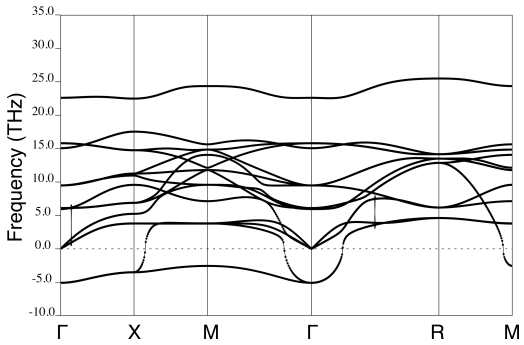

Figure 4.3: Phonon diagram for the cubic perovskite structure of $BaTiO_3$ with reference lattice constant $a_0 = 3.94$ Å.

The ferroelectric unstable mode remains unstable along the Γ-M path of the Brillouin zone. The small dispersion of the phonon branch suggests that zone-boundary modes can be stabilized through epitaxial strain or another external effect. The possibility of stabilizing Kittel-type of antiferroelectric phases is explored in section 4.3.1.

Strontium titanate $SrTiO_3$

The low-temperature phase of strontium titanate ($SrTiO_3$) corresponds to an antiferrodistortive phase. The ground state has a tetragonal (*I4/mcm*) structure corresponding to an $a^0a^0c^-$ oxygen octahedron rotation pattern, as shown in Fig. 4.4. The phonon diagram of $SrTiO_3$ has a weak ferroelectric instability at the Γ point as well as antiferrodistortive instabilites at the M and R points. These instabilities produce $a^0a^0a^+$ and $a^0a^0c^-$ oxygen octahedron rotations patterns, respectively.

In the case of $SrTiO_3$, antiferrodistortive and ferroelectric instabilities are present in the cubic reference phase, and each of them individually leads to a decrease of

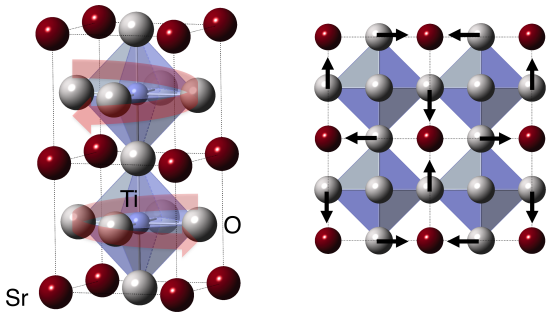

Figure 4.4: Represenation of the oxygen octahedron rotation pattern of the ground state of $SrTiO_3$.

energy. However, the final ground state involves the condensation of only one mode: the R point instability. This is interpreted as a competition between ferroelectric and antiferrodistorive instabilities [71], where the stabilization of one instability inhibits the stabilization of the other.

Calcium titanate $CaTiO_3$

As shown in Fig. 4.5, similar instabilities are present in the reference structure of calcium titanate ($CaTiO_3$). In the case of bulk $CaTiO_3$, these instabiltities are stronger and give rise to a more complex sequence of phase transitions with decreasing temperature [72].

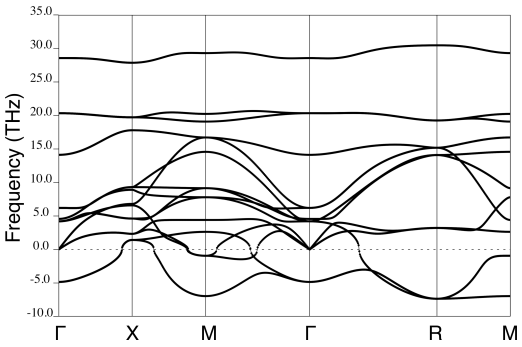

Figure 4.5: Phonon diagram for the cubic perovskite structure of $CaTiO_3$ with reference lattice constant $a_0 = 3.80$ Å.

The ground state structure of $CaTiO_3$ has an orthorhombic *Pnma* $GdFeO_3$-structure type, which is the most common ground state structure among distorted perovskites [73].

The orthorhombic *Pnma* structure is derived from the reference unit cell through rotations of the oxygen octahedron cage, denoted as $a^-a^-c^+$ in Glazer notation, and allows an antipolar displacement of the Ca atoms along the $\langle 110 \rangle$ cubic direction. In this case, despite the presence of ferroelectric instabilities, the ground state has only antiferrodistortive distortions.

4.2 Antiferroelectric perovskites

In this section, the experimental literature of antiferroelectric perovskites is reviewed. The phase transition sequence, dielectric and structural properties are described, as well as their potential technological applications. In chapter 5, the effect of epitaxial strain is investigated on the competition between ferroelectriciy and antiferroelectricity in $PbZrO_3$. In chapter 6, the field-induced antiferroelectric transition is studied in $NaNbO_3$ based ceramics.

Lead zirconate $PbZrO_3$

Lead zirconate ($PbZrO_3$) was the first material identified as antiferroelectric [2]. $PbZrO_3$ is by far the most extensively studied among the antiferroelectric perovskites [6]. In addition to the abrupt change in polarization, the antiferroelectric transition of $PbZrO_3$ has a large volume expansion. Optimal functional properties for transducers and actuators is an active area of research [57].

In bulk form, $PbZrO_3$ has a cubic perovskite structure at high temperatures and a nonpolar orthorhombic ground state below $T_c \sim 505$ K. Under an applied electric field, $PbZrO_3$ single crystals undergo a sequence of first-order phase transitions to rhombohedral ferroelectric phases [74]. In bulk polycrystalline ceramics, double hsyteresis loops are only observed in a narrow temperature window below the critical temperature [2].

The ground state has an orthorhombic *Pbam* structure with unit cell dimensions $\sqrt{2}a_0 \times 2\sqrt{2}a_0 \times 2a_0$ with respect to the pseudocubic lattice constant a_0 [75, 76]. Its distorted perovskite structure is derived from the cubic perovskite phase through oxygen octahedron rotation around the $\langle 110 \rangle$ cubic axis, denoted as $a^-a^-c^0$ in Glazer notation.

The rotation pattern allows an antipolar displacement of Pb^{+2} ions along the $\langle 110 \rangle$ cubic direction, as shown in Fig. 4.6.

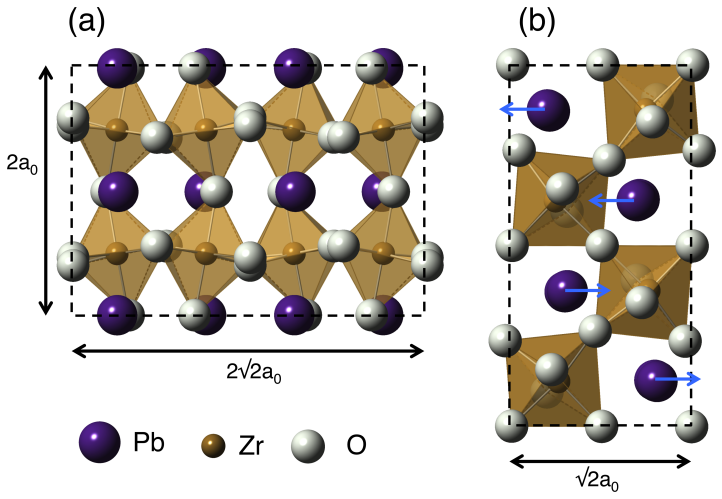

Figure 4.6: Crystal structure of the *Pbam* ground state of $PbZrO_3$. (a) and (b) correspond to the plane views with $\hat{x}$ and $\hat{z}$ as normal vectors.

$PbZrO_3$ is the end point member of the technologically important $Pb(Zr_xTi_{1-x})O_3$ (PZT) system [77, 112]. The morphotropic phase boundary at Ti/Zr $\sim$ 52/48 isovalent substitution separates a tetragonal ferroelectric phase in the Ti rich side, from a rhombohedral ferroelectric phase in Zr rich side of the boundary. The large polarizability change at the phase boundary has important applications in piezoelectric ceramic devices such as transducers and actuators.

Lead hafnate $PbHfO_3$

Lead Hafnate ($PbHfO_3$) display a similar sequence of phase transitions as $PbZrO_3$ [78, 79]. The structural similarities between these two compounds originate from the similar properties of the Hf and Zr atoms. The lanthanide contraction, which occurs because of poor shielding of the core by f electrons, results in a large decrease of ionic radii. Thus Hf^{+4} and Zr^{+4} are of similar size.

The ground state of $PbHfO_3$ has an orthorhombic *Pbam* structure, isostructural to the ground state of $PbZrO_3$. Between 163^{o}C and 215^{o}C, dielectric and structural studies report a tetragonal antiferroelectric phase. This antiferroelectric phase coexists

with a ferroelectric phase, similar in structure than the high-temperature rhombohedral ferroelectric phase observed in the PZT system.

Sodium niobate $NaNbO_3$

Sodium niobate ($NaNbO_3$) is a well known lead-free antiferroelectric material [80, 81]. $NaNbO_3$ has a low dielectric constant, large band gap, and a large capacitance at high DC bias, and is therefore the most promising candidate for high-temperature and high-voltage high energy density energy storage devices.

In bulk form, $NaNbO_3$ has a cubic perovskite structure at high temperature ($> 640^oC$) and a rather complex sequence of antiferrodistortive and antiferroelectric phase transitions at low temperatures [82, 83], shown in Table 4.1. The ground state of $NaNbO_3$ is ferroelectric ($< -100^oC$) and has a rhombohedral structure.

Table 4.1: Experimental phases of $NaNbO_3$. Table reproduced from Ref. [7].

Phase	Space Group	Temp.(^{o}C)
Cubic	$Pm\bar{3}m$	>640
Tetragonal	*P4/mbm*	575-640
Orthorhombic	*Ccmm*	520-575
Orthorhombic	*Pnmm*	480-520
Orthorhombic	*Pmmm*	360-480
Orthorhombic	*Pbcm*	−100-360
Rhombohedral	*R3c*	<−100

Extensive structural analysis have established an antiferroelectric phase of $NaNbO_3$ between -100^{o}C and 360^{o}C [7]. The antiferroelectric phase has an orthorhombic *Pbcm* structure and unit cell dimensions $\sqrt{2}a_0 \times \sqrt{2}a_0 \times 4a_0$ with respect to the cubic lattice constant a_0. Its distorted structure consists of a layered tilting of oxygen octahedrons with in-phase and out-of-phase rotations along the *c* axis, denoted as $(a^-b^-c^+)/(a^-b^-c^-)$ in Glazer notation. This octahedral rotation pattern allows for an antipolar displacement of the Na cations in the $\langle 110 \rangle$ cubic direction, as shown in Fig 4.7 (a).

Double hysteresis loops, characteristic of antiferroelectricity, have been observed in single crystal $NaNbO_3$ [84]. A critical electric field of ∼90 kV/cm is observed at

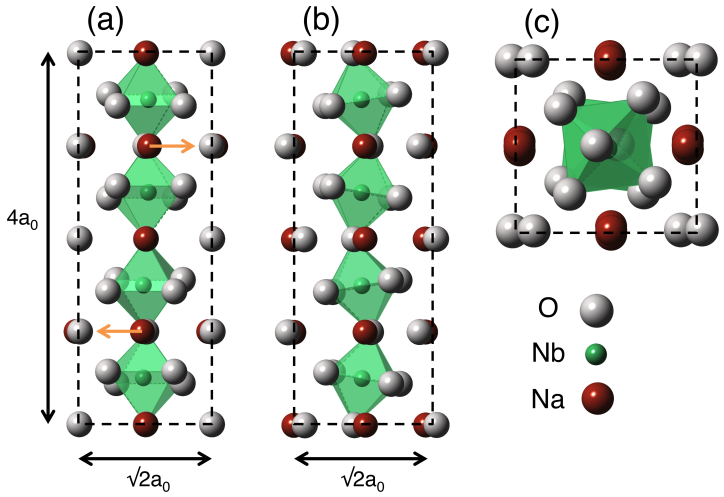

Figure 4.7: Crystal structure of the *Pbcm* ground state of $NaNbO_3$. (a), (b) and (c) correspond to the $\hat{x}$, $\hat{y}$ and $\hat{z}$ lattice vectors.

room temperature, and increases with decreasing temperature. The field induced ferroelectric phase has a polar orthorhombic $Pmc2_1$ structure [85, 86] between -100^oC and 257^oC [87]. Its distorted structure has an $a^-a^-c^+$ rotation pattern that couples to a polar displacement of Na cations along the $\langle 110 \rangle$ cubic direction.

Al low temperatures ($< -100^oC$), $NaNbO_3$ transforms to a different structure under an applied electric field. In this case, the field-induced ferroelectric phase has a rhombohedral *R3c* $LiNbO_3$-structure type, isostructural to the ground state of the system. This structure corresponds to a polar displacement of the Na and Nb atoms in the $\langle 111 \rangle$ cubic direction, accompanied by oxygen octahedral rotations denoted as $a^-a^-a^-$ in Glazer notation.

Silver niobate $AgNbO_3$

Silver niobate ($AgNbO_3$) has been widely studied as a microwave ceramic and photocatalytic antiferroelectric material [7]. In bulk form, $AgNbO_3$ has a similar sequence of antiferrodistortive and antiferroelectric phase transitions as $NaNbO_3$, shown in Table 4.2. First reports of antiferroelectricity in $AgNbO_3$ at room temperature were contradictory. Hysteresis measurements indicated weak ferroelectricity based on remanent polarization. Dielectric and structural similarities with $NaNbO_3$ suggested the

centrosymmetric orthorhombic *Pbcm* structure for the ground state.

Table 4.2: Experimental phases of $AgNbO_3$. Table reproduced from Ref. [7].

Phase	Space Group	Temp.(^{o}C)
Cubic	$Pm\bar{3}m$	>579
Tetragonal	*P4/mbm*	387-579
Orthorhombic	*Cmcm*	361-387
Orthorhombic	-	353-361
Orthorhombic	*Pbcm*	267-353
Orthorhombic	*Pbcm*	67-267
Orthorhombic	$Pmc2_1$	<67

However, detailed structural analysis revealed an uncompensated antiferroelectric, or ferrielectric, ground state of $AgNbO_3$ [7]. The ferrielectric structure has a polar orthorhombic $Pmc2_1$ space group and unit cell dimensions $\sqrt{2}a_0 \times \sqrt{2}a_0 \times 4a_0$ with respect to the cubic lattice constant a_0. Similar to the case of $NaNbO_3$, its distorted structure has a $(a^-b^-c^+)/(a^-b^-c^-)$ layered tilting of oxygen octahedrons rotations along the c axis. Unlike the case of $NaNbO_3$, the antipolar displacement of the Ag cations in the $\langle 110 \rangle$ cubic direction are uncompensated and produce a small but non-zero polarization.

High quality ceramic samples showed double-hysteresis loops, characteristic of antiferroelectricity. A critical electric field of 110 kV/cm and a saturation polarization 52 μC/cm^2 were observed, along with a small but nonzero remanent polarization under no external field. The remanent polarization is understood from the ferrielecric phase but the structure of the field induced ferroelectric phase remains unknown. As it is shown in section 4.3, the small energy difference between the ferrielectric ground state and the *R3c* $LiNbO_3$-structure suggest this phase as the most likely candidate for the field-induced ferroelectric transition.

4.3 Why are there so few antiferroelectric perovskites?

Since the discovery of $PbZrO_3$ by G. Shirane in 1951, only a few more examples have been added to the short list of pure antiferroelectric perovskites. The vast majority of

the perovskite compounds have an antiferrodistortive ground state with normal dielectric behavior. However, as is discussed earlier, the cubic perovskite reference structure has a strong tendency to form polar distortions. Compounds that exhibit a polar instability have metastable polar phases, which is a necessary condition for antiferroelectricity. This important insight from first principles, raises the question of: why are these non-polar materials not antiferroelectric?

As pointed out by G. Shirane [2, 47] and empashized in this work, antiferroelectric double hysteresis loops originate due to a small free energy difference between antiferroelectric and ferroelectric phases. Recent first principles results [88, 89] suggest that this energy difference is remarkably small, on the order of 1 meV/f.u. Table 4.3 summarizes first principles results for perovskite antiferroelectrics.

Table 4.3: Energy difference $\Delta E = E_{nonpolar} - E_{polar}$ (meV/f.u.) between the nonpolar and polar structures of known perovskites antiferroelectrics. Energy differences are calculated with: ABINIT, norm-conserving pseupodpotentials and LDA ($\Delta E_{(a)}$), and with VASP, the projected augmented method and LDA ($\Delta E_{(b)}$) or GGA ($\Delta E_{(c)}$).

Compound	Ground state	Polar phase	$\Delta E_{(a)}$	$\Delta E_{(b)}$	$\Delta E_{(c)}$
$PbZrO_3$	*Pbam*	*R3c*	−1	−5	9
$PbHfO_3$	*Pbam*	*R3c*	0	−4	6
$NaNbO_3$	*Pbcm*	$Pmc2_1$	−1	1	2
$AgNbO_3$	*Pbcm*	*R3c*	1	−2	1

Although this energy difference can in principle be engineered through chemical modification or other effects, it is remarkable that pure compounds display such a small energy difference with no tuning parameter. This small energy difference, originated from a delicate balance between short-range and long-range Coulomb interactions, is even smaller than the order of magnitude of the superconducting energy gap ($\backsimeq$10 meV).

In this section, first principles are used to investigate the microscopic structural origin of the small energy difference observed in antiferroelectric perovskites. The stability of Kittel type of antiferroelectrics is studied, along with the role of oxygen octahedral rotations in the stabilization of antiferroelectricity. The search for more

antiferroelectric in the perovskites and other families of compounds is left to chapter 8.

4.3.1 Kittel antiferroelectric phases

As a starting point, the stability of Kittel type of antiferroelectric phases is considered in the prototypical perovskite $BaTiO_3$. As mentioned earlier ans shown in Fig. 4.3, the unstable ferroelectric phonon branch of $BaTiO_3$ remains unstable along the Γ-X-M path of the Brillouin zone. The small dispersion of the unstable phonon branch suggests the stabilization of Kittel type antiferroelectric phases in pure $BaTiO_3$, under an external effect such as epitaxial strain, pressure or size effect.

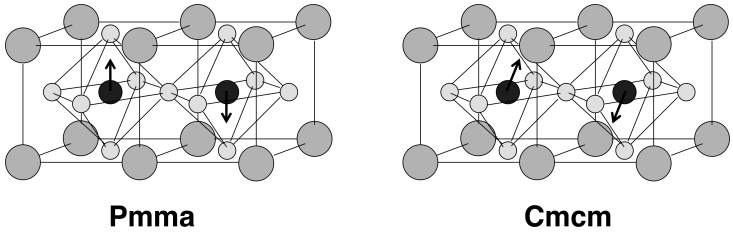

Figure 4.8: Antipolar structures with X point symmetry. The Ti ions are displaced in the $\langle 001 \rangle$ and $\langle 011 \rangle$ cubic directions.

Our first principles calculations show that highly-distorted structures such as the *Pnma* $GdFeO_3$-structure type reduce to more symmetrical structures due to the absence of antiferrodistortive instabilities in the reference cubic phase. Kittel type antiferroelectric phases, which entail antiparallel displacement of linear chains of ions, are generated by freezing-in the zone-boundary X and/or M modes, as depicted in Fig 4.8. The energy difference and relevant structural parameters of these structures are reported in Table 4.4.

The effect of epitaxial strain on polar and antipolar phases is reported in Fig. 4.9. At any epitaxial strain value, the ground state of $BaTiO_3$ is ferroelectric. The structure transforms from tetragonal to rhombohedral at compressive strains, and from rhombohedral to orthorhombic at tensile strains, in agreement with previous results [90]. The energy of antipolar phases with X point symmetry is lowered at compressive and

Table 4.4: Energy difference $\Delta E = E_{cubic} - E_{phase}$ (meV/f.u.), polarization P (μC/cm^2) and volume expansion $\Delta V/V$ (%) for polar and antipolar structures of $BaTiO_3$.

Phase	ΔE	P	$\Delta V/V$.
$Pm\bar{3}m$	0	0	0
$Pmma$	-1.7	0	0.30
$Cmcm$	-2.3	0	0.38
$P4mm$	-7.2	29	0.59
$Amm2$	-9.5	32	0.76
$R3m$	-10.3	33	0.83

tensile strains, but the energy gain is not enough to stabilize the structure. The energy of antipolar phases with M point symmetry is small and therefore are not shown.

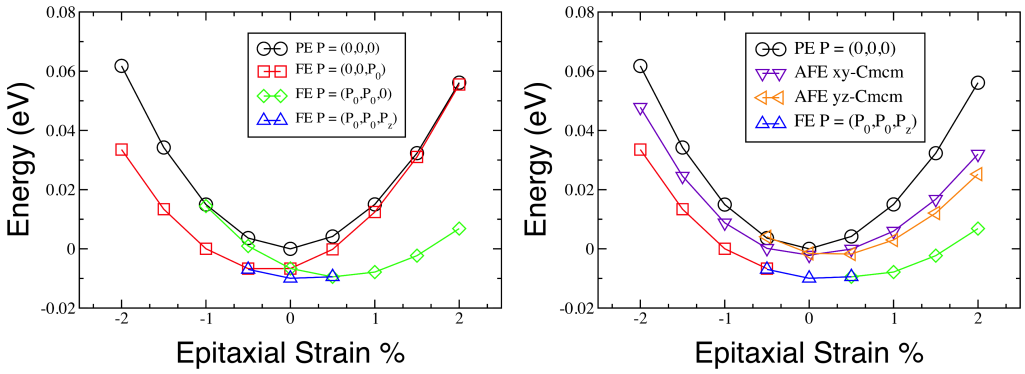

Figure 4.9: Epitaxial strain effect on polar structures (left) and antipolar structures (right) of $BaTiO_3$.

In antiferroelectric perovskites, hydrostatic pressure tends to stabilize the nonpolar ground state [7]. In the case of Kittel antiferroelectric phases, Fig. 4.10 shows that application of positive and negative pressure suppress the antipolar displacement of the ions.

From these results, it is concluded that Kittel type antiferroelectric phases are not stabilized in pure $BaTiO_3$ through epitaxial strain or pressure. The highly symmetric perovskite structure readily allows for a reorientation of the polarization, favoring the experimentally observed ferroelectric phases.

Finally, it is briefly mentioned that superlattices of $BaTiO_3$ and BaO have shown antipolar distortions [91]. Where the stabilization of antipolar states is originated by the

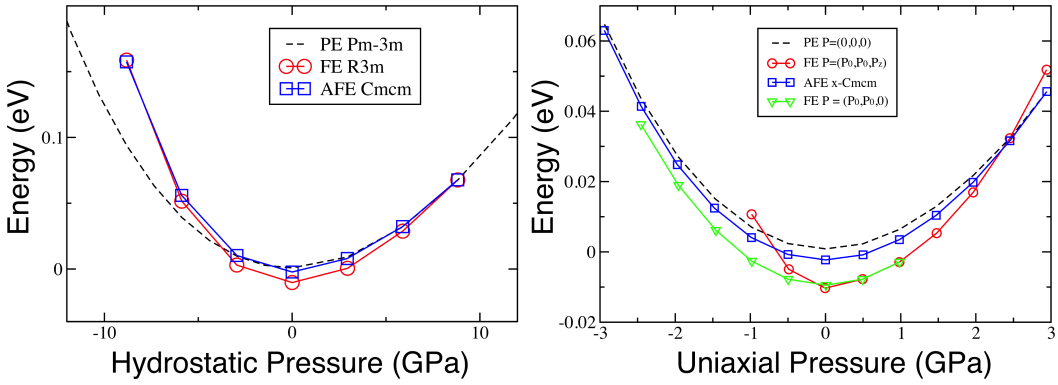

Figure 4.10: Effect of hydrostatic (left) and uniaxial (right) pressure on the polar and antipolar structures of $BaTiO_3$.

inhibition of the ferroelectric phase through the depolarization field of the paraelectric superlattice.

4.3.2 The role of oxygen octahedron rotations

Perovskites compounds are capable of lowering their total energy through simultaneous freezing of structural modes. As mentioned earlier, oxygen octahedral rotations play a dominant role in antiferroelectric perovskites. As shown in Table 4.5, first principles calculations show that artificial suppression of oxygen rotations in antiferroelectric perovskites favors the competing ferroelectric structure.

Table 4.5: Energy difference $\Delta E = E_{antipolar} - E_{polar}$ (meV/f.u.) and volume difference $\Delta V/V$ (%) between antipolar and polar structures under artificial supresion of oxygen octahedron rotations.

Compound	Antipolar	Polar	ΔE	$\Delta V/V$
$PbZrO_3$	*Pbam*	*R3m*	11	0.6
$PbHfO_3$	*Pbam*	*R3m*	13	0.3
$NaNbO_3$	*Cmcm*	*Amm2*	29	0.2
$AgNbO_3$	*Cmcm*	*R3m*	24	0.6

The absence of antiferrodistorive instabilities in $BaTiO_3$ results from the strong B-site character of the polar instability. The B-site character of the polar instability is incompatible with oxygen octahedral tiltings and originates competition between polar and antiferrodistortive distortions. It is concluded that in order to stabilize a Kittel

type antiferroelectric phase, perovskites with strong polar and antiferrodistortive A-site instabilitities must be consider.

In close analogy to the case of antiferroelectric perovskites, it is noticed that stabilization of the antipolar X mode is commonly observed in the case of orthorhombic *Pnma* perovskites with the $GdFeO_3$-structure type. As mentioned in section 4.1.3, the *Pnma* structure corresponds to the most common ground state among distorted perovskites [73]. The search for antiferroelectric compounds in this subclass of compounds is investigated in chapter 8.

Kittel type antiferroelectric phases and antiferrodistortive structures can be thought of two opposite extremes cases of the phase diagram. Antiferroelectric perovskites are therefore an intermediate case, where oxygen octahedron rotations stabilize the antipolar displacements of atoms in such a way that the energy difference between nonpolar and polar phases is negligibly small, on the order of 1 meV/f.u, right at the phase boundary.

4.3.3 Antiferroelectric energy barrier

The role of the energy barrier in the field-induced ferroelectric transition is investigated. The energy landscape separating the competing nonpolar and polar phases was studied with nudged elastic-band (NEB) calculations [92]. The NEB method is extensively used in computational chemistry to find reaction pathways and transition states.

In a nudged elastic band calculation, the minimum energy path between an initial and final states is found by performing relaxations of the intermediate structures obtained by linear interpolation of the atomic positions. Each of the intermediate structures is called an *image* and corresponds to a snapshot along the reaction path. The spacing constraint between adjacent images is imposed by simulated spring forces. The crystal structure of each image is relaxed in the projected space perpendicular to the energy barrier, along with the degrees of freedom of the springs. In the climbing image method [93], the highest energy image is pushed upwards during the optimization procedure in order to find the transition state.

The energy barrier for a uniform antiferroelectric to ferroelectric transition obtained for $PbZrO_3$ and $NaNbO_3$ are shown in Fig. 4.11. It is noticed that in our calculations, the volume of the initial, intermediate and final states is kept fixed to the corresponding calculated relaxed volume of the antiferroelectric phase.

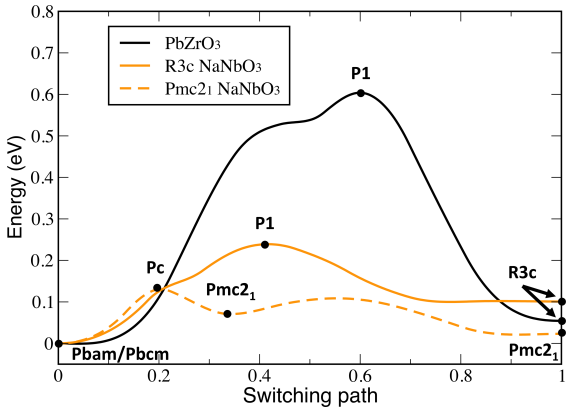

Figure 4.11: Energy barrier of uniform antiferroelectric transition for $PbZrO_3$ and $NaNbO_3$. The structure of the initial, final and metastable states are denoted.

From the results it can be observed that $PbZrO_3$ has a large energy barrier than $NaNbO_3$. The small energy barrier separating the *Pbcm* and *Pmc2*$_1$ structures of $NaNbO_3$ is consistent with the experimental observation of coexistence of phases. In the case of $NaNbO_3$, two competing ferroelectric phases are considered. The energy barrier corresponding to the *Pmc2*$_1$ polar phase is smaller, consistent with experiments. In addition, a metastable state is found in the energy barrier. The small energy difference between the metastable and field-induced phases can explain the experimental observation of of metastable ferroelectricity, described in chapter 6.

Further insights into the structural evolution can be obtained by studying the mode content of the intermediate structures. Fig. 4.12 shows the mode decomposition of the nudged-elastic band calculations for $PbZrO_3$ and $NaNbO_3$. The value of the mode amplitude at the end points is consistent with the relaxed value in the locally stable structures. Compared to the amplitude of the zone-boundary modes, the polar mode amplitude is larger in the case of $PbZrO_3$ than in the case of $NaNbO_3$. It is observed also that in both cases, the mode amplitude of the octahedral rotation mode R_5^- is rather constant. Finally, stabilization of the polar mode Γ_4^- suppresses the stabilization of

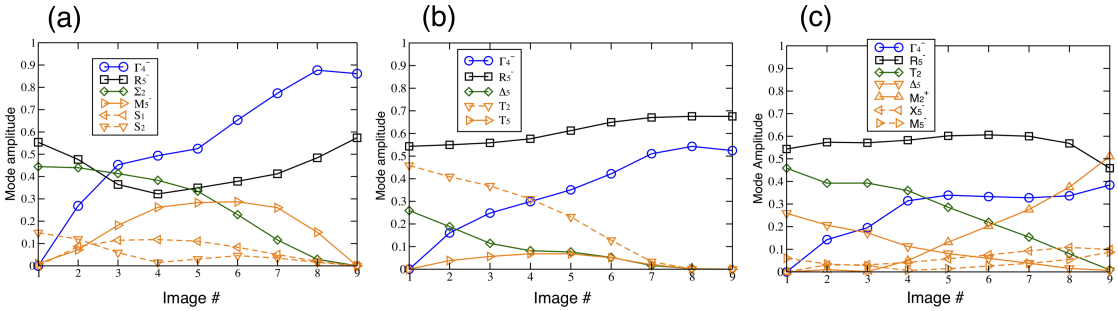

Figure 4.12: Mode amplitude evolution of the antiferroelectric transition in antiferroelectric perovskites. Structural transitions between (a) *Pbam* and *R3c* in $PbZrO_3$, (b) *Pbcm* and *R3c* in $NaNbO_3$, and (c) *Pbcm* and *Pmc2*$_1$ in $NaNbO_3$.

antipolar modes such as Σ_2, Δ_5 and T_2 in green.

4.3.4 Origin of the small energy difference

The calculated phonon dispersion diagram of $NaNbO_3$ and $PbZrO_3$ in their high-temperature cubic perovskite structure is shown in Fig 4.13. Several similarities are observed between the phonon diagrams. In addition to the strong ferroelectric instabilities, both materials display strong antiferrodistortive instabilities at the M and R points. The antipolar instability at the X point is rather weak and has A-site character, and the A-site displacement of atoms is due to the primary octahedral rotation mode at R.

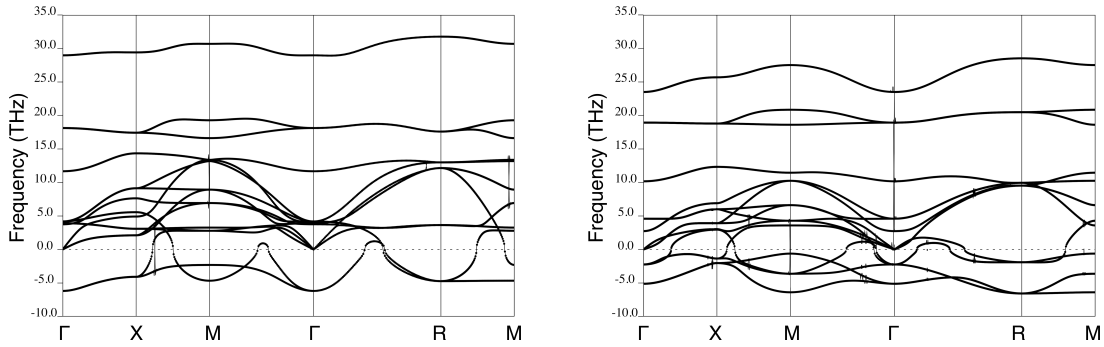

Figure 4.13: Phonon diagram for the cubic perovskite structure of $NaNbO_3$ and $PbZrO_3$, with reference lattice constant 3.93 Åand 4.11 Å, respectively.

In the case of $NaNbO_3$, the instability at R_5^- is weaker than the one at Γ_4^-, but the energy gain of freezing in the R_5^- mode is larger than the energy gain of freezing

the Γ_4^- [94]. In $NaNbO_3$ and $PbZrO_3$, the unstable phonon branch between the R and M points has no dispersion. This flat phonon curve describes independent octahedral rotations among successive layers, with negligible energy gain for octahedral rotations along the $\hat{z}$ axis.

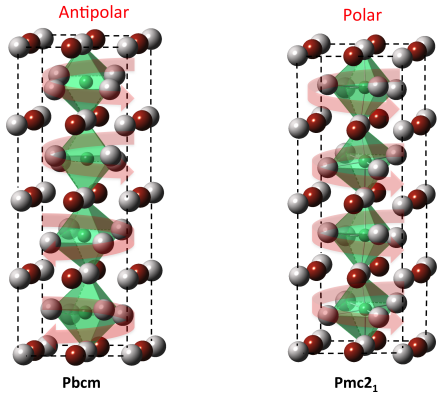

Figure 4.14: Relationship between oxygen octahedron rotations in the nonpolar (*Pbcm*) and polar (*Pmc2*$_1$) structures of $NaNbO_3$.

In the harmonic approximation, the origin of the small energy difference between nonpolar and polar structures is attributed to the absence of coupling between successive layers along the $\hat{z}$ axis. In the case of $NaNbO_3$, this corresponds to transformation from the layered $(a^-b^-c^+)/(a^-b^-c^-)$ structure generated by the T mode to the $a^-a^-c^+$ octahedral tilting observed in the field-induced *Pmc2*$_1$ phase (Fig. 4.14). In the case of $PbZrO_3$, a negligible energy gain is obtained when transforming from the $a^-a^-c^0$ tilting of the *Pbam* ground state to the $a^-a^-a^-$ tilitng of the *R3c* phase.

4.3.5 Conclusions

In conclusion, in the case of perovskites, oxygen octahedral rotation play an important role in the stabilization of antiferroelectricity. First, the nonpolar and polar structures are generated by R point octahedral rotations. Next, the antiferrodistortive distortion couples to A-site displacement of the cations under no external field. Stabilization of an antiferroelectric structure is expected therefore whenever the antipolar X mode is unstable in the phonon dispersion curve and symmetry-allowed by the other distortion modes.

Finally, the negligible energy gain of octahedral tiltings along the $\hat{z}$ direction explains the small energy difference between the nonpolar and polar structures. It is concluded, based on first principles calculations, that known antiferroelectric perovskites correspond to a intermediate case between Kittel-type of antiferroelectric phases and purely antiferrodistortive structures. The octahedron rotation pattern of antiferroelectric perovskites correspond to a flat energy region of the phonon space, allowing a small energy difference between alternative structures.

Chapter 5

Antiferroelectricity and ferroelectricity in epitaxially strained $PbZrO_3$ from first principles

Experimental and theoretical studies have shown the important role of epitaxial strain in the stabilization of ferroelectricity in thin films. In the particular case of complex oxides, the magnitude of the thin film polarization can be enhanced or suppressed with respect to its bulk value. As it is found in the case of $BaTiO_3$, epitaxial strain has a strong effect on the stability of the ferroelectric ground state. As a general rule for ferroelectric oxides, compressive strain favors the tetragonal ferroelectric phase with out-of-plane polarization, while tensile strain favors favors the orthorhombic ferroelectric phase with an in-plane orientation of the polarization.

Recent experimental results have been demonstrated a polarization increase of 250% with respect to bulk single crystals in $BaTiO_3$ epitaxial films [95]. Furthermore, epitaxial strain is able to stabilize ferroelectricity in non-ferroelectric bulk materials [96, 97]. When antiferrodistortive instabilities are also present, the sequence of phase transitions can be modified, producing to rich structural phase diagrams.

Lead zirconate $PbZrO_3$ correspond to a prototypical antiferroelectric material. In bulk form, $PbZrO_3$ has a cubic perovskite structure at high temperatures and a non-polar orthorhombic *Pbam* ground state below $T_c \sim 505$ K. Under an applied electric field, $PbZrO_3$ single crystals undergo a first order phase transition into a sequence of polar phases with rhombohedral symmetry. In thin films, the competition between the rhombohedral low-energy structures and the ground state is less studied.

In this chapter [88], first principles calculations are performed to investigate the effect of epitaxial strain on the structure and stability of antiferroelectric $PbZrO_3$. The concept of equilibrium energy strain (σ) is introduced to estimate the position of the

energy minimum for a given structure in the epitaxial strain diagram. This concept proved to be extremely useful for subsequent projects, in particular for the prediction of epitaxial strain stabilization of antiferroelectricity in high-throughput search of materials.

5.1 Thin film $PbZrO_3$

There is a renewed interest in antiferroelectric materials driven by potential technological applications. An antiferroelectric [5] is like a ferroelectric [3, 4] in that its structure is obtained through distortion of a nonpolar high-symmetry reference structure; for ferroelectrics the distortion is polar, while for antiferroelectrics it is nonpolar. However, not all nonpolar phases thus obtained are antiferroelectric; in addition, there must be an alternative ferroelectric phase obtained by a polar distortion of the same reference structure, close enough in free energy so that an applied electric field can induce a first-order phase transition from the antiferroelectric to the ferroelectric phase, producing a characteristic polarization-electric field (P-E) double-hysteresis loop. The electric-field-induced transition is the source of functional properties and promising technological applications. Non-linear strain and dielectric responses at the phase switching are useful for transducers and electro-optic applications [98, 99]. The shape of the double hysteresis loop suggests applications in high-energy storage capacitors [100, 101]. In addition, an effective electro-caloric effect can also be induced in systems with a large entropy change between the two phases [59].

Lead zirconate $PbZrO_3$ (PZO) was the first material identified as antiferroelectric [2]. Despite extensive studies and characterization, PZO continues to offer insights into the origin and complexity of antiferroelectricity [6, 7]. In bulk form, PZO has a cubic perovskite structure at high temperatures and a nonpolar orthorhombic ground state below $T_c \sim 505$ K. The ground state has space group *Pbam* [75, 76] and unit cell dimensions $\sqrt{2}a_0 \times 2\sqrt{2}a_0 \times 2a_0$ with respect to the reference lattice constant a_0. Its distorted perovskite structure is derived from the cubic (C) unit cell through a nonpolar Σ_2

distortion mode of Pb^{+2} ion displacements in the $\langle 110 \rangle_C$ direction, combined with oxygen octahedron rotation R_5^- modes around the $\langle 110 \rangle_C$ axis ($a^-a^-c^0$ in Glazer notation). Under an applied electric field, PZO single crystals undergo a first order phase transition into a sequence of polar phases with rhombohedral symmetry [74]. Similar rhombohedral polar phases are observed in the polycrystalline ceramic system $Pb(Zr_{1-x}Ti_x)O_3$ under small 5-10 % isovalent substitution of zirconium for titanium [77, 102]. In thin films, the competition between the rhombohedral low-energy structures and the PZO ground state is less studied. Room temperature ferroelectricity have been reported below a certain critical thickness [103] and under large compressive epitaxial strain [104]. Under different circumstances, large remnant polarizations $P_r \sim$ 5-20 $\mu C/cm^2$ have been measured in P-E antiferroelectric-like double hysteresis loops [104–107], suggesting coexistence of ferroelectricity with antiferroelectricity.

In this paper, we present first principles calculations performed to investigate the effect of epitaxial strain on the structure and stability of PZO. In bulk, we find a small energy difference of $\sim$ 1 meV/f.u between the nonpolar ground state *Pbam* and the alternative polar phase *R3c*. Under epitaxial strain, a small energy difference between these two competing low-energy phases persists over a remarkably wide range of experimentally accessible epitaxial strain. While ferroelectricity is favored at compressive strains, the nonpolar ground state is favored at tensile strains. In the strain regime where the nonpolar phase is lower in energy, the small energy difference between the nonpolar and polar phases ensures antiferroelectricity. The coexistence of ferroelectricity and antiferroelectricity observed in thin films is attributed to a combination of strain and depolarization field effects.

5.1.1 Technical details and notations

Density-functional calculations are performed using version 6.4.1 of `ABINIT` [30] package. The local-density approximation (LDA), a plane-wave energy cutoff of 680 eV, and a $4 \times 4 \times 4$ Monkhorst-Pack sampling of the Brillouin zone [25] were used for all structural optimizations. Polarization was calculated in a $10 \times 10 \times 10$ grid using the

modern theory of polarization [22] as implemented in `ABINIT`. Norm-conserving pseudopotentials are used from the Bennett-Rappe library [68] with reference configurations: $Pb([Hg]6p^0)$, $Zr([Kr]4d^05s^0)$ and $O(1s^22s^22p^4)$, generated by the `OPIUM` code [108]. In order to allow direct comparison with experiments, the epitaxial strain diagram was constructed with respect to $a_0 = 4.1$ $\mathring{A}$, which is the cube root of the calculated volume per f.u. of the *Pbam* ground state. This reference lattice constant coincides with the optimized lattice constant of the cubic perovskite structure, and underestimate the experimental value of 4.16 $\mathring{A}$ [109] by 1.5 %.

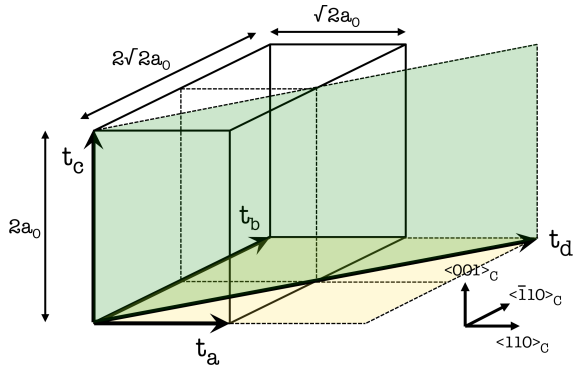

Figure 5.1: Lattice vectors of the *Pbam* ground state structure. The $\sqrt{2}a_0 \times 2\sqrt{2}a_0 \times 2a_0$ unit cell is shown with solid lines. While the (001) plane is defined by the lattice vectors $\mathtt{t}_a$ and $\mathtt{t}_b$, the (120) plane is defined by the lattice vectors $\mathtt{t}_c$ and $\mathtt{t}_d$.

The effect of epitaxial strain was investigated through "strained-bulk" calculations [110, 111]. As shown in Fig. 5.1, the unit cell of the *Pbam* ground state structure contains two symmetry-inequivalent primitive perovskite planes, (001) and (120) ($(001)_C$ and $(010)_C$ with respect to the cubic perovskite vectors), and therefore allows two distinct orientations for epitaxial growth over a square terminated $(001)_C$ perovskite substrate. Epitaxial strain is imposed on the structure by fixing the two lattice vectors defining the matching plane and optimizing the length and direction of the third, out-of-plane, lattice vector, along with the atom positions, until the forces on the atoms are less than 0.05 meV/A.

Epitaxially strained phases are designated as *ePbam* to distinguish them from bulk *Pbam*. It is stressed that while the space group is preserved as *Pbam* when (001) is chosen as the matching plane (*c-ePbam*), the symmetry is lowered to *P2/m* when the

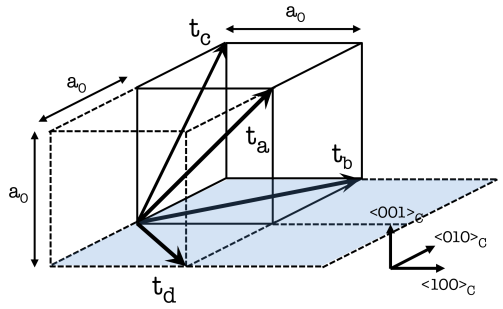

Figure 5.2: Lattice vectors of the *R3c* phase. The epitaxial plane (001) is defined by the lattice vectors $\mathtt{t}_b$ and $\mathtt{t}_d$.

(120) plane is chosen as the matching plane (*ab-ePbam*). Similarly, the symmetry of the rhombohedral phase *R3c* is lowered to monoclinic *Cc* by epitaxial strain on a square substrate, and it is refer to this phase as *eR3c* in the rest of the paper. For epitaxial strain calculations, the *eR3c* structure is maped into the unit cell defined by $\{\mathtt{t}_a,\mathtt{t}_b,\mathtt{t}_d\}$ in Fig. 5.2, where the lattice vectors $\mathtt{t}_b$ and $\mathtt{t}_d$ define the (001) matching plane.

5.1.2 Bulk results

The low-energy bulk PZO structures obtained by distortion of the cubic perovskite structure are identified through unstable modes, as calculated in the phonon spectrum by linear response DFT [69]. The focus of the attention are on the polar and nonpolar structures generated by the unstable polar mode and by unstable oxygen octahedron rotation modes. In close analogy with $PbTiO_3$, the strong instability of PZO at Γ is a result of the well-known lone-pair stereochemical activity of Pb atoms. In the absence of zone boundary modes, freezing-in the polar Γ_4^- mode leads to ferroelectric phases similar to $BaTiO_3$, see Table 5.1. In the hypothetical *P4mm* structure, the polar instability induces a large displacement ~ 0.65 $\mathring{A}$ of Pb^{+2} ions against the oxygen octahedron network and a large polarization, comparable to $PbTiO_3$. The addition of out-of-phase octahedron rotations along the $\langle 111\rangle_C$ direction of *R3m* ($c^-c^-c^-$ in Glazer notation) leads to the metastable *R3c* phase, with the $LiNbO_3$ structure type. The small energy difference between this phase and the *Pbam* ground state suggests this structure as the most promising candidate for the field induced ferroelectric phase [7].

The strong rotational instability of PZO produces low-energy structures even in

Table 5.1: Space group, energy gain $\Delta E = E_{cubic} - E_{phase}$ (meV/f.u.), polarization magnitude P (μC/cm^2), estimated equilibrium strain for the $(001)_C$ (σ_c) and $(100)_C$ (σ_a) matching planes, and volume expansion $\Delta V/V$ (%) of selected polar structures.

Space group	ΔE	P	σ_c	σ_a	$\Delta V/V$
$Pm\bar{3}m$	0	0	0	0	0
P4mm	248	78	-0.74	1.43	2.07
Amm2	272	77	1.59	0.45	2.50
R3m	299	80	0.94	0.94	2.83
R3c	344	102	0.14	-	0.51

the absence of polar distortions. As shown in Table 5.2, coupling between R and M point octahedron rotations can further decrease the energy of the system by inducing displacement of Pb atoms. The symmetry lowering from combinations of oxygen octahedron rotation modes can induce additional zone-boundary distortions, such as the X_5^- mode in *Pnma* ($a^+b^-b^-$) and *P4$_2$/nmc* ($a^+a^+c^-$), and the R_4^- mode in *Cmcm* ($a^0b^+c^-$).

Table 5.2: Space group, formula units (f.u.), Glazer notation, energy gain $\Delta E = E_{cubic} - E_{phase}$ (meV/f.u.), estimated equilibrium strain for the $(001)_C$ (σ_c) and $(010)_C$ (σ_b) matching planes, and volume expansion $\Delta V/V$ (%) of 15 possible [178] combinations of M and R point rotation modes. ($*$) refers to convergence to this high-symmetry structure.

Space group	f.u.	Glazer not.	ΔE	σ_c	σ_b	$\Delta V/V$
$Pm\bar{3}m$	1	$a^0a^0a^0$	0	0	0	0
$Im\bar{3}$	8	$a^+a^+a^+$	212	-0.24	-0.24	-0.61
$R\bar{3}c$	2	$c^-c^-c^-$	270	-0.39	-	-1.07
I4/mcm	4	$a^0a^0c^-$	234	-1.36	0.02	-1.25
I4/mmm	8	$a^0b^+b^+$	216	0.08	-0.47	-0.77
P4$_2$/nmc	8	$a^+a^+c^-$	276	-0.68	-0.21	-0.99
P4/mbm	2	$a^0a^0c^+$	214	-1.38	0.10	-1.11
Imma	4	$a^0b^-b^-$	291	0.09	-0.64	-1.09
Immm	8	$a^+b^+c^+$	$^*Im\bar{3}$			
Cmcm	8	$a^0b^+c^-$	282	-0.66	-0.61	-1.12
Pnma	4	$a^+b^-b^-$	306	-0.45	-0.49	-1.32
C2/c	4	$a^-b^-b^-$	$^*Imma$			
C2/m	4	$a^0b^-c^-$	$^*Imma$			
P2$_1$/m	4	$a^+b^-c^-$	$^*Pnma$			
$P\bar{1}$	4	$a^-b^-c^-$	$^*Imma$			

Structures obtained by freezing-in selected additional unstable zone-boundary modes

are reported in Table 5.3. In the absence of octahedral rotations, the polar *R3m* structure has a lower energy than the four f.u. *Pbam* structure (see Table 5.1 and 5.3). While the addition of out-of-phase octahedral rotations in the *R3m* structure leads to the *R3c* phase with $\sim$ 45 meV/f.u. energy gain, addition of $a^-a^-c^0$ octahedron rotations in the four f.u. *Pbam* structure produces the observed eight f.u. *Pbam* structure with $\sim$ 65 meV/f.u. energy gain, favoring the nonpolar ground state.

Table 5.3: Space group, formula units (f.u.), relevant mode content, energy gain $\Delta E = E_{cubic} - E_{phase}$ (meV/f.u.), estimated equilibrium strain for the $(001)_C$ (σ_c) and $(010)_C$ (σ_{ab}) matching planes, and volume expansion $\Delta V/V$ (%) of selected nonpolar structures.

Space group	f.u.	mode	ΔE	σ_c	σ_{ab}	$\Delta V/V$
Cmcm	2	X_5^-	71	0.72	0.71	2.22
Pmma	2	M_5^-	147	1.49	-0.35	2.08
Pbam	4	Σ_2-M_5^-	288	1.56	0.35	2.37
Pbam	8	Σ_2-R_5^-	345	0.62	-0.33	0.05

Fully relaxation of the *Pbam* and *R3c* structures leads to a remarkably small energy difference of $\sim$ 1 meV/f.u. between them. The volume of the *R3c* polar structure is slightly larger (0.47 %) than that of the nonpolar *Pbam* structure. The experimental lattice constants of *Pbam*, a = 5.8736 $\mathring{A}$, b = 11.7770 $\mathring{A}$ and c = 8.1909 $\mathring{A}$, at 10 K [113] are underestimated by the calculated lattice constants, a = 5.8253 $\mathring{A}$, b = 11.7199 $\mathring{A}$ and c = 8.1072 $\mathring{A}$, by 1 %, typical of LDA. For comparison, it is also calculated the energy difference using the experimental *Pbam* volume and found that the energy difference between the observed *Pbam* and the hypothetical field-induced *R3c* structure is also $\sim$ 1 meV/f.u., comparable to previous results [114–116].

5.1.3 Epitaxial strain

Next, the effect of epitaxial strain is considered on the relative stability of various structures. The degree of stabilization of a certain structure can be determined by comparing the shape and dimensions of its relaxed structure with the epitaxial strain conditions. For a given structure, with relaxed unit cell lattice vectors $\{\mathtt{t}_a,\mathtt{t}_b,\mathtt{t}_c\}$, and a given matching plane, with out-of-plane lattice vector $\mathtt{t}_j$, the equilibrium energy

minimum is estimated at $\sigma_j = 100 \times (1/2) \times \sum_i (\mathtt{t}_i - \mathtt{t}_{i0})/\mathtt{t}_{i0}$ epitaxial strain; where i denotes the two lattice vectors defining the matching plane, and the reference lattice vectors $\{\mathtt{t}_{a0},\mathtt{t}_{b0},\mathtt{t}_{c0}\}$ are the relevant linear combination of the cubic perovskite vectors with $a_0 = 4.1$ $\mathring{A}$. As an example, the relaxed lattice parameters of the *Pbam* ground state are compared with the corresponding edges of the $\sqrt{2}a_0 \times 2\sqrt{2}a_0 \times 2a_0$ unit cell (see Fig. 5.1). The results are in Table 5.3; while σ_c estimates the energy minimum of *c-ePbam* at ~ 0.62 % tensile strain, σ_{ab} estimates the energy minimum of *ab-ePbam* at ~ 0.33 % compressive strain. This illustrates how this approach can help identify phases that would be favored by nonzero epitaxial strain.

The bulk energies of the calculated structures and their σ values for the relevant matching planes are shown in Table 5.1, 5.2 and 5.3. Based on the assumption that these phases have comparable effective elastic constants to those of *Pbam* and *R3c*, we note that the energy gain ΔE at the optimal equilibrium strain σ of these structures is not large enough to overcome the energy cost relative to *Pbam* and *R3c*. Through this simple argument, it is concluded therefore that they will not be stabilized at $|\eta| < 4$ % epitaxial strain; this has been verified for the case of *Pnma*. The effects of epitaxial strain on *R3c* and *Pbam*, the lowest-energy structures of PZO, are shown in Fig. 5.3 (a). The relaxed structure of *Pbam* has a large contraction of ~ 1.27 % in the $\mathtt{t}_c$ axis and a large expansion of ~ 0.3 % and ~ 0.9 % in the $\mathtt{t}_a$ and $\mathtt{t}_b$ axis, explaining the large separation between energy minima of *ePbam* (large value of $\sigma_c - \sigma_{ab}$ as discussed in the previous paragraph) and the robust ground state at tensile strain. Around 0 % strain, the in-plane lattice constants of the *Pbam* structure are less compatible with the square-lattice epitaxial constraint, and the elastic energy costs of deforming the bulk equilibrium state lift the *c-ePbam* energy curve above the energy curve of the *eR3c* phase. Phonon eigenfrequencies of *c-Pbam* calculated at selected values of 1 and 3 % tensile strain show no further instabilities and confirm its stability against polar distortions.

The focus is now on the remarkably small energy difference between *ePbam* and *eR3c* over nearly the entire range of strain. While the ferroelectric *eR3c* phase is

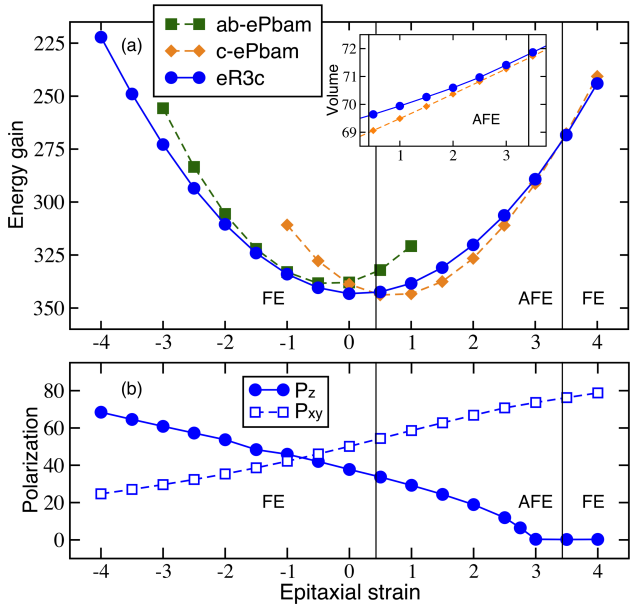

Figure 5.3: (a) Energy (meV/f.u.) vs epitaxial strain (%) diagram. Epitaxial strain is computed as described in the text. FE and AFE refers here to ferroelectric and antiferroelectric ground state, respectively. Inset: Volume per f.u. ($\mathring{A}^3$) vs epitaxial strain (%) in the AFE region. (b) Polarization (μC/cm^2) components of the *eR3c* phase as a function of epitaxial strain (%). P_z and P_{xy} denote the perpendicular and parallel components with respect to the matching plane.

favored for strains less than 0.4 %, between 0.4 % and 3.4 % tensile strain, the *c-ePbam* phase is favored over the *eR3c* phase. Throughout this range, the energy difference between the nonpolar and polar structures is smaller than $\sim$ 7 meV/f.u., leading to antiferroelectricity. The ferroelectric *eR3c* phase is again stabilized between 3.4 % and 5 % strain, while the four f.u. *Pbam* structure is the lowest energy state above 5 %. While within the accuracy of the calculations it is not possible precisely to predict the critical strains that will be observed in experiments, a semiquantitative agreement is expected. In the region where antiferroelectricity is stabilized, the antiferroelectric-ferroelectric field induced transition between the *c-ePbam* ground state and the *eR3c* phase has a maximum volume expansion of $\sim$ 0.85 % at $\sim$ 0.4 % tensile strain (see inset of Fig. 5.3 (a)). The effect of epitaxial strain on the polarization of the *eR3c* phase is shown in Fig. 5.3 (b).

5.1.4 Discussion

The computed epitaxial strain diagram can be used to interpret P-E hysteresis loops observed in PZO films. Films under tensile strain exhibit classic double hysteresis loops [117], consistent with our results. Under compressive strain, antiferroelectric-like double loops with non-zero remanent polarization have been observed [104,106,107,117] with a magnitude P_r proportional to the film conductivity. This apparent inconsistency with the results can be resolved by recognizing that observation of ferroelectricity in a film requires compensation of the depolarization field. In highly insulating high-quality films, with negligible compensation of the depolarization field, electrostatic energy would suppress the ferroelectric phase in favor of a nonpolar antiferroelectric phase [117]. In samples with free carriers available to compensate the depolarization field, nonzero remanent polarization would arise from the ferroelectric phase present in the coherently strained region near the interface [104]. In highly coherent thin films, compensation of the depolarization field would favor ferroelectric behavior. Finally, in thick films, relaxation of the majority of the film to the bulk antiferroelectric *Pbam* phase can also account for the observed double loops.

5.2 Conclusions

In summary, two different structures of PZO, one nonpolar *ePbam* and one polar *eR3c*, are very close in energy and compete under the effect of epitaxial strain. While ferroelectricity is stabilized at compressive epitaxial strain, antiferroelectricity is favored at tensile strains.

Chapter 6

Nonlinear increase of critical electric-field in doped antiferroelectric $NaNbO_3$

Sodium niobate ($NaNbO_3$) is a well known antiferroelectric material [81, 151]. As mentioned in section 4.2, $NaNbO_3$ is a promising lead-free candidate for high-temperature and high-voltage energy density storage devices.

In $NaNbO_3$ based ceramics, the application of an external electric field stabilizes a low-energy ferroelectric phase. Upon removal of the electric field, ferroelectric and antiferroelectric phases coexist. Recent experimental results have shown the appearance of antiferroelectric double hysteresis loops in (Ca,Zr) substituted $NaNbO_3$ ceramics [152], where a small ($\sim$ 2-5 %) chemical doping has a large effect in the energy landscape of the system.

In this chapter, first principles calculations are performed to study the field-induced ferroelectric transition of $NaNbO_3$. The effect of chemical modification in the antiferroelectric energy barrier is studied with experimental measurements and first principles calculations. A phenomenological model is proposed to explain the appearance of double hysteresis loops in (Ca,Zr) doped $NaNbO_3$.

6.1 Field-induced ferroelectric transition in $NaNbO_3$

In bulk form, $NaNbO_3$ has a cubic perovskite structure at high temperature ($> 640^oC$) and a rather complex sequence of antiferrodistortive and antiferroelectric phase transitions at low temperatures [82, 83]. The ground state of $NaNbO_3$ is ferroelectric ($< -100^oC$) and has a rhombohedral structure. Table 6.1 summarize experimental information for the relevant phases [153–155].

Table 6.1: Relevant experimental phases of $NaNbO_3$. Space group, lattice constants (Å) and polarization P ($\mu C/cm^2$) of the observed phases.

Phase	Sp.Grp.	a	b	c	P
C	$Pm\bar{3}m$	3.944			0
Q	$Pmc2_1$	5.513	5.571	7.766	12
P	$Pbcm$	5.511	5.573	15.526	0
N	$R3c$	5.56		$\beta = 59.1^o$	-

Extensive structural analysis have established an antiferroelectric phase of $NaNbO_3$ between -100^{o}C and 360^{o}C [7]. The antiferroelectric phase has an orthorhombic $Pbcm$ structure, which is obtained from the reference cubic structure by the simultaneous condensation of the incommensurate T_2 mode and the R_5^- octahedron rotation mode [94]. The in-phase and out-of-phase $(a^-b^-c^+)/(a^-b^-c^-)$ layered rotation pattern allows an antipolar displacement of the Na cations with Δ_5 symmetry, as shown in Fig 6.1.

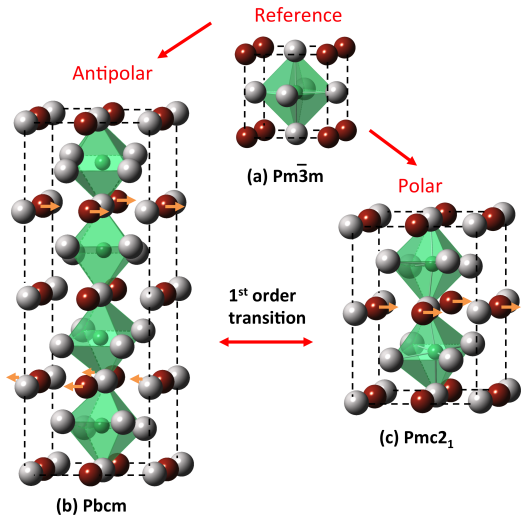

Figure 6.1: Experimentally reported phases of $NaNbO_3$: (a) reference $Pm\bar{3}m$, (b) antipolar $Pbcm$ and (c) polar $Pmc2_1$ structures.

Double hysteresis loops, characteristic of antiferroelectricity, have been observed in single crystal $NaNbO_3$ [84]. A critical electric field of ∼90 kV/cm is observed at room temperature along the crystal direction perpendicular to the c axis, and increases with decreasing temperature. The field induced ferroelectric phase has a polar orthorhombic $Pmc2_1$ structure [85, 86] between -100^oC and 257^{o}C [87]. Its distorted structure has unit cell dimensions $\sqrt{2}a_0 \times \sqrt{2}a_0 \times 2a_0$ with respect to a_0, and consist of an $a^-a^-c^+$

octahedron rotation pattern accompanied by a polar displacement of Na cations along the $\langle 110 \rangle$ cubic direction.

At low temperatures ($< -100^{o}$C), $NaNbO_3$ transforms to a different structure under an applied electric field. In this case, the field induced ferroelectric phase has a rhombohedral *R3c* $LiNbO_3$-structure type, isostructural to the ground state of the system. This structure corresponds to a polar displacement of the Na and Nb atoms in the $\langle 111 \rangle$ cubic directions, accompanied by oxygen octahedron rotations denoted as $a^-a^-a^-$ in Glazer notation.

However, the antiferroelectric phase of $NaNbO_3$ is extremely sensitive to stoichiometry. In single crystals, a small (0.6 mol%) K substitution of Na decreases the critical electric field of $(Na_{1-x}K_x)NbO_3$ to 20 kV/cm, an continuous cycling of the applied field stabilizes the ferroelectric phase [156]. Polycrystalline $NaNbO_3$ displays coexistence of antiferroelectric and ferroelectric phases [157,158], and the system transforms to a ferroelectric phase under a strong electric field. Antiferroelectric $[(Ag_{0.05}Na_{0.95})_{1-x}K_x]NbO_3$ can be driven to an antiferroelectric-ferroelectric phase boundary at $x = 2.3\%$, where kinetic competition between antiferroelectric transitions and ferroelectric domain reversal is observed [159]. As pointed out by Xu *et al.*, the rather slow kinetic of antiferroelectric switching competes with ferroelectric domain transitions.

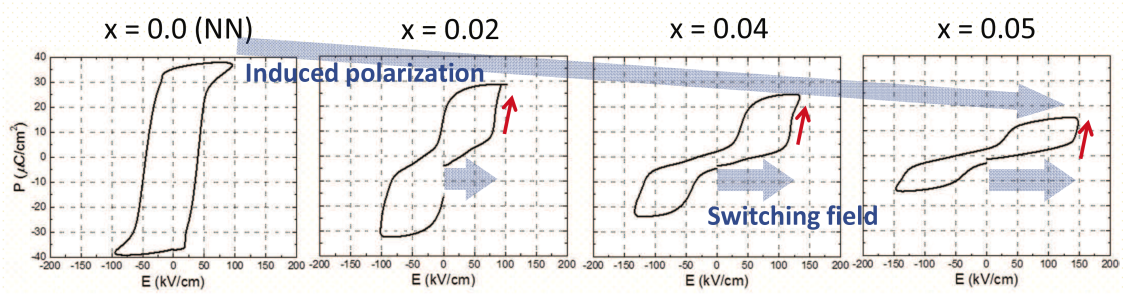

Figure 6.2: Experimental hysteresis measurements for the $(Na_{1-x}Ca_x)(Nb_{1-x}Zr_x)O_3$ system. Reproduced with permission from Ref. [152].

As shown in Fig. 6.2, recent experimental results [152] show that Ca and Zr doped polycrystalline $NaNbO_3$ develops antiferroelectric-like double hysteresis loops. At small ($\sim$ 2-5 %) chemical doping level, $(Na_{1-x}Ca_x)(Nb_{1-x}Zr_x)O_3$ display double hysteresis

loops, with increasing critical electric field ($\Delta E_c \sim 100$ kV/cm) and decreasing total induced polarization ($\Delta P \sim 25$ μC/cm^2) as a function of doping.

In this work, first principles calculations are performed to investigate the effect of chemical modification in the field-induced transition of $NaNbO_3$. The appearance of double hysteresis loops in Ca and Zr doped polycrystalline $NaNbO_3$ are explained as a result of a small increase of dielectric response at the working temperature. The increase of dielectric permittivity modifies the energy landscape, decreasing the energy barrier between the nonpolar and polar structures, and effectively increasing the rate of antiferroelectric switching. Based on experimental measurements and first principles calculations, the effect of chemical modification in the energy landscape is described, and a model is proposed to quantify the increase of critical electric field as a function of chemical substitution.

6.2 Technical details

Density-functional calculations are performed using version 7.4.1 of `ABINIT` [30]. The local-density approximation (LDA), a plane-wave energy cutoff of 680 eV, and a $4\times4\times4$ Monkhorst-Pack sampling of the Brillouin zone [25] were used for all structural optimizations of $NaNbO_3$. Polarization was calculated in a denser $8 \times 8 \times 8$ grid using the modern theory of polarization [22] as implemented in `ABINIT`. Norm-conserving pseudopotentials are used from the Bennett-Rappe library [68] with reference configurations: $Na([Ne]3s^0)$, $Nb([Kr]4d^0\ 5s^0)$ and $O(1s^2 2s^2 2p^4)$, generated by the `OPIUM` code [108].

Accurate energy differences are compared to density-functional theory (DFT) calculations performed using version 5.2 of `VASP` [32] package. The local-density approximation (LDA), the projected augmented wave (PAW) method and a plane-wave energy cutoff of 500 eV are used for all structural optimizations. The electronic and ionic contributions to the dielectric tensor are calculated using density functional perturbation theory, as implemented in `VASP` and described in section 2.3.

6.3 First principles results

The relative stability of the relevant phases is first explored in a perfectly homogeneous crystal using first principles calculations. Table 6.2 shows the total energy, lattice constants, polarization and volume difference for the relevant low energy structures. The computed structural parameters show good agreement with the experimental values reported in Table 6.1, with the 1% underestimate of lattice constants characteristic of *LDA* calculations. The ground state is the ferroelectric *R3c* phase, in agreement with experiments.

Table 6.2: Space group symmetry, lattice constants (Å) and polarization P (μC/cm^2) of the relevant structures of $NaNbO_3$. Energy per formula unit $\Delta E = E_{cubic} - E_{phase}$ (meV/f.u.) with respect to the reference perovskite structure. Volume difference $\Delta V/V$ (%) with respect to the antiferroelectric *Pbcm* phase.

Phase	Modes	ΔE	a	b	c	P	$\Delta V/V$
$Pm\bar{3}m$		0	3.94			0	4.41
$R\bar{3}c$	R_4^+	-102	5.48		13.54	0	0.27
Pnma	X_5^+ M_3^+ R_4^+	-126	5.51	5.44	7.75	0	-0.94
$Pmc2_1$	Γ_4^- M_3^+ R_4^+	-150	5.49	5.55	7.71	60	0.18
Pbcm	Δ_5 R_5^- T_2	-151	5.48	5.55	15.41	0	0
R3c	Γ_4^- R_4^+	-155	5.55		$\beta = 59.05^o$	50	0.95

A remarkably small energy difference is found between the nonpolar *Pbcm* phase and the polar $Pmc2_1$ structures. This small energy difference ($\sim$ 1 meV/f.u.) is characteristic of antiferroelectricity [88, 89, 114], and suggest that the polar $Pmc2_1$ structure is the most probable structure for the field induced ferroelectric phase. Assuming that the critical field E_C required to overcome the energy barrier is given by $E_C \sim \Delta E$ / V P, with V and P the volume and polarization of the $Pmc2_1$ phase (V=58.6 Å^3/f.u.), the critical field is estimated as $E_C \sim 146$ kV/cm.

6.3.1 Energy landscape

The energy landscape is explored between *Pbcm* and $Pmc2_1$ by performing structural relaxations at different values of the polar mode amplitude $Q_{\Gamma_4^-}$. Fig. 6.3 (squares) shows the energy of the intermediate polar structures as a function of their total polarization. For small values of $Q_{\Gamma_4^-}$, the energy of the system increases, as expected for

freezing in a stable mode. The induced polar structure (before the energy barrier) has an orthorhombic space group $Pmc2_1$ with 8 formula units, twice the size of the unit cell of the field-induced ferroelectric $Pmc2_1$ phase.

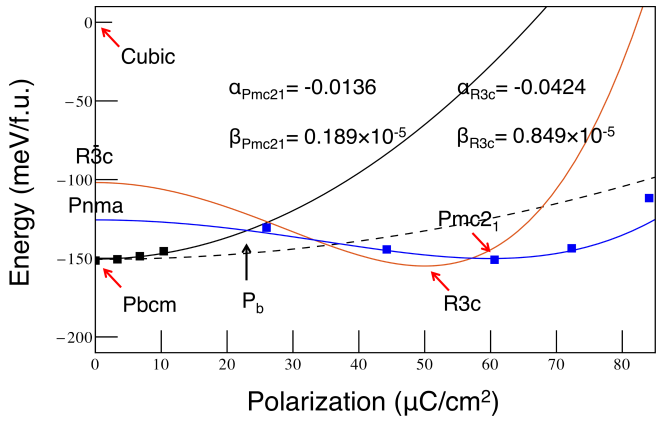

Figure 6.3: Energy barrier separating the antiferroelectric *Pbcm* and the ferroelectric $Pmc2_1$ and *R3c* phases.

At $P_b \sim 23\ \mu$C/cm^2, an energy barrier with magnitude $E_b \sim 18$ meV/f.u. is found, which separates the antiferroelectric *Pbcm* phase, from the field-induced ferroelectric $Pmc2_1$ phase. Above this threshold value, the layered rotation pattern is isometrically reorientated around the *c* lattice vector as shown in Fig. 4.14, and the structure relaxes to the polar orthorhombic $Pmc2_1$ phase if the constraint is removed.

Table 6.3: Static dielectric matrix for the nonpolar *Pbcm* and polar $Pmc2_1$ structures. Electronic and ionic contributions are computed using perturbation density functional theory (PDFT) and the relations introduced in section 2.3.

Phase	ϵ^{el}_{xx}	ϵ^{el}_{yy}	ϵ^{el}_{zz}	ϵ^{ion}_{xx}	ϵ^{ion}_{yy}	ϵ^{ion}_{zz}
$Pmc2_1$	5.80	5.76	6.07	108.79	80.51	3047.09
Pbcm	5.69	5.58	5.97	61.1	69.7	2415.5

As shown in Fig. 6.3, the antiferroelectric energy barrier can also be found by intersecting the energy profile corresponding to the *Pbcm* and $Pmc2_1$ structures. For small values of polarization, the nonpolar *Pbcm* phase correspond to a linear dielectric, whose energy is described by:

$$E(P) = E_{Pbcm} + \frac{1}{2}\frac{\epsilon}{(\epsilon - \epsilon_0)^2}P^2,$$

with E_{Pbcm} the energy of the $Pbcm$ phase and ϵ the dielectric constant of the structure. Table 6.3 shows the calculated static dielectric tensor for the nonpolar and polar structures. For the $Pbcm$ structure, the in-plane value of ϵ^{ion} is consistent with the experimental value $\epsilon_r^{exp} = 76$ (at room temperature) for single crystals [156, 160].

Similarly, the energy curve for the ferroelectric $Pmc2_1$ structure is described by:

$$E(P) = E_{Pnma} + \alpha_{Pmc2_1} P^2 + \beta_{Pmc2_1} P^4,$$

where E_{Pnma} corresponds to the energy of the auxiliary reference structure $Pnma$ and the constants α_{Pmc2_1} and β_{Pmc2_1} are found from the conditions $E|_{P_0} = E_{Pmc2_1}$ and $\partial E/\partial P|_{P_0} = 0$, where $P_0 = P_{Pmc2_1}$. As shown in Fig. 6.3, the energy expansion reproduces the first principles constrained calculations.

For comparison, the energy barrier for the rhombohedral phase $E_b^{R3c} = 24$ meV/f.u. is 33% larger, with a critical electric field of 354 kV/cm. In this case, the energy versus polarization curve $E(P) = E_{R\bar{3}c} + \alpha_{R3c} P^2 + \beta_{R3c} P^4$ is constructed using the nonpolar rhombohedral $R\bar{3}c$ $NdAlO_3$-structure type as the auxiliary reference structure.

6.3.2 Chemical substitution

The task is now to explain the large increase of critical electric field observed in $NaNbO_3$ under ∼5 % Ca and Zr doping. The small change in tolerance factor and microscopic polarizability is described by the small increase of dielectric response of the nonpolar phase.

As the polycrystalline system is chemically doped, the position of the Curie temperature (T_C) is lowered from 350^{o}C to 200^{o}C, effectively increasing the dielectric permittivity of the system from 300 to 350 (at 120^{o}C). As can be seen from Fig.6.3, the change in dielectric response modifies the position P_b and height E_b of the antiferroelectric energy barrier. Using the experimental values for the permittivity $\epsilon_r \sim$ 300-350 at 120^{o}C, the antiferroelectric energy barrier decreases by 8 % relative to its original value at ϵ_r =300.

The effect of chemical modification in $NaNbO_3$ is explained as follows. In pure polycrystalline $NaNbO_3$, the energy barrier for ferroelectric polarization reversal is smaller than the antiferroelectric energy barrier for field-induced transitions, explaining the single hysteresis loop shown in Fig. 6.2. As a function of chemical doping, the antiferroelectric energy barrier decreases, increasing the density of antiferroelectric domains and the rate of antiferroelectric switching during electric field cycling.

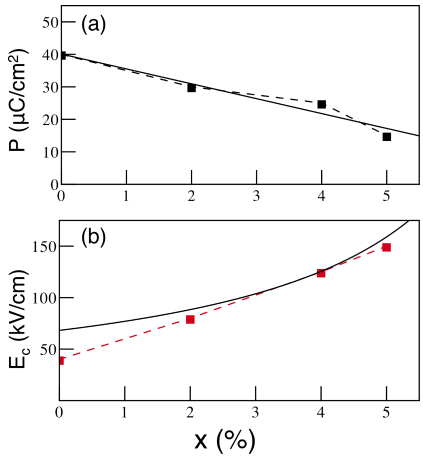

Figure 6.4: As a function of chemical doping x (%): (a) fitting to the experimental polarization and (b) experimental and estimation of the phenomenological model for the critical electric field.

A simple phenomenological model is proposed to describe the effect of chemical doping (x) in $NaNbO_3$ based ceramics. If the volume fraction of polar and nonpolar domains in the sample is described by:

$$n_p(x) = e^{-\Delta E_p(x)/kT} \qquad n_{np}(x) = e^{-\Delta E_{np}(x)/kT},$$

where $\Delta E_p(x)$ and $\Delta E_p(x)$ are the energy barriers for polar or nonpolar switching ($n_p(x) + n_{np}(x) = 1$), the macroscopic polarization of the system is therefore given by:

$$P(x) = P_0(1 - e^{-\Delta E_{np}(x)/k_B T})$$

with P_0 the microscopic polarization of a single domain, k_B is Boltzmann's constant and T the temperature.

Assuming a simple linear decrease of the antiferroelectric energy barrier as a function of doping $\Delta E_{np}(x) = \Delta E_{np}(0) - \alpha x$, the macroscopic polarization for small values of

substitution $x \ll 1$ is given by:

$$P(x) = P - \frac{\alpha}{k_B T} e^{-\Delta E_{np}(0)/kT} x.$$

This linear relationship is fitted to the experimental polarization measurements in Fig. 6.4 (a), from where it is obtained $k_B T = 34$ meV and $\alpha = 15.6$ eV, since $n_{np}(0) = e^{-\Delta E_{np}(0)/kT} \backsimeq 1$. From this result the critical electric field $E_c(x)$ can be estimated as seen in Fig. 6.4 (b), as well as the volume fraction of polar and nonpolar domains at different doping values. Finally, it is noticed that further knowledge of the ferroelectric energy barrier allows the estimation of the critical chemical doping $n_c(x)$ for the appearance of the antiferroelectric double hysteresis loops.

6.4 Conclusions

In conclusion, the large increase of critical electric field in $NaNbO_3$ under small chemical doping of Ca and Zr is explained by the increase of dielectric response of the nonpolar structure. The antiferroelectric energy barrier is decreased, effectively increasing the probability of switching to the nonpolar state. The increase of critical electric field and the decrease of total polarization in the sample are therefore explained by the increasing number of domains that switch to the antiferroelectric phase, which do not contribute to the total polarization of the system.

Chapter 7

Antiferroelectricity in thin film ZrO_2 from first principles

Zirconia (ZrO_2) is an extensively investigated high-K dielectric with a wide range of significant technological applications in electronics and materials science. In the bulk, ZrO_2 has three well-known experimental phases: cubic, tetragonal and monoclinic. Recently, experimental reports have shown antiferroelectric-like double-hysteresis loops in thin-film ZrO_2 and ferroelectricity in thin film $(Zr_{0.5}Hf_{0.5})O_2$ [56]. The structure of the field-induced polar phase is orthorhombic ($Pca2_1$) and corresponds to a distortion of the high-symmetry cubic structure. These observations have aroused interest, but the question of whether this new functional behavior corresponds to an intrinsic or extrinsic property remained open.

In this chapter, first-principles density-functional calculations are performed to demonstrate that the observed behavior corresponds to an intrinsic property of ZrO_2. It is concluded that the tetragonal phase of ZrO_2, which is stabilized by the thin-film geometry, is a previously unrecognized lead-free antiferroelectric.

Unlike other known antiferroelectrics, the field-induced ferroelectric phase does not arise from a polar instability of a high-symmetry reference structure. This corresponds to a novel structural mechanism, which is described using a Landau-Devonshire model, providing a basis for broader searches for antiferroelectric materials with optimal functional properties. In addition, it is demonstrated that the ferroelectric phase of ZrO_2 can be stabilized through epitaxial strain or continuous substitution of Zr by Hf, inviting further experimental investigation.

These results are of interest both in the fundamental physics of functional materials and in the discovery and development of new materials with potential technological importance. In particular, the field-induced switching mechanism of ZrO_2 represents a

new class of antiferroelectrics, inviting for the exploration of more ZrO_2-like antiferroelectrics in the AXY family of compounds.

7.1 Thin film ZrO_2

Zirconia (ZrO_2) is a high-k dielectric [118], chemically and structurally similar to HfO_2, and likewise is a candidate for dynamic random access memory (DRAM) applications [119, 120] and complementary metal-oxide-semiconductor (CMOS) devices [121, 122]. Bulk ZrO_2 has a high-symmetry cubic ($Fm\bar{3}m$) structure (Fig. 7.1(a)) above 2400 K, and a tetragonal ($P4_2/nmc$) structure (Fig. 7.1(b)) between 2400 K and 1200 K [123]. The tetragonal structure is related to the cubic structure by freezing in an unstable X_2^- mode [124] and is nonpolar. Below 1200 K, ZrO_2 is monoclinic ($P2_1/c$) (Fig. 7.1(c)). The first-order transition from the tetragonal phase to the monoclinic phase changes the coordination number of Zr from 8 to 7 and increases the volume by ~ 5 %.

In light of the extensive research which has been conducted over the past fifty years on this relatively simple dielectric, the recent report of antiferroelectric-like double-hysteresis loops in thin film ZrO_2 [56] at first seems rather surprising. In thin film ZrO_2, the tetragonal-monoclinic transition temperature is suppressed and the structure is tetragonal at room temperature [125–127]; in contrast, thin film HfO_2 is monoclinic at room temperature and exhibits simple dielectric behavior. The field-induced polar phase in ZrO_2, which appears above a critical field on the order of 2 MV/cm, is isostructural with the ferroelectric phases that have been observed in thin films of HfO_2 doped with Al [128], Y [129], Gd [130], Si [131, 132] and Sr [133], as well as in $(Hf_{1/2}Zr_{1/2})O_2$ thin films [134, 135]. The structure of the polar phase is orthorhombic ($Pca2_1$) [136] and corresponds to a distortion of the high-symmetry cubic structure, as depicted in Fig. 7.1.

Antiferroelectrics have recently been the subject of increasing interest [5]. The characteristic electric-field-induced transition from a nonpolar to a strongly polar phase is the source of functional properties and promising technological applications. Non-linear strain and dielectric responses due to the phase switching are useful for transducers

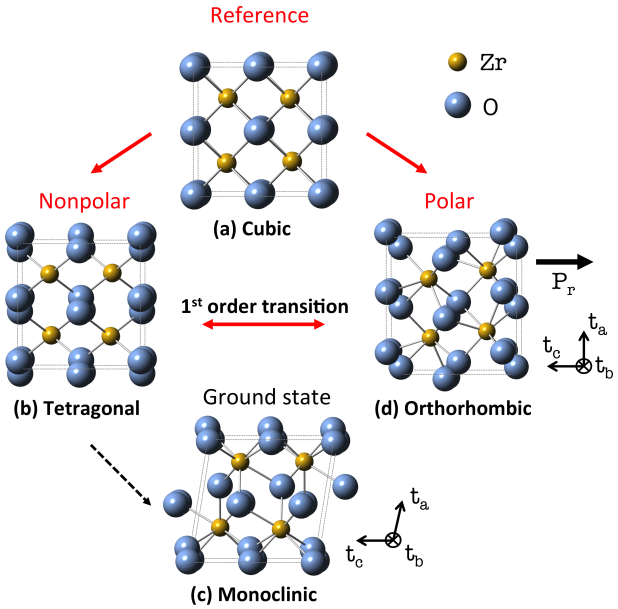

Figure 7.1: Experimentally reported phases of ZrO_2: (a) Cubic ($Fm\bar{3}m$), (b) Tetragonal ($P4_2/nmc$), (c) Monoclinic ($P2_1/c$) and (d) Orthorhombic ($Pca2_1$).

and electro-optic applications [98, 99]. The shape of the double hysteresis loop suggests applications in high-energy storage capacitors [100, 101]. In addition, an electrocaloric effect can be observed in systems with a large entropy change between the two phases [59]. While most attention has focused on $PbZrO_3$ and related perovskites [7], a recent theoretical materials design search [137] suggested that there are many more antiferroelectric compounds to be discovered.

In this work, first-principles calculations are used to provide clear evidence that the tetragonal phase of ZrO_2 is a previously unrecognized antiferroelectric material, and that the behavior observed in thin films is intrinsic. A remarkably small energy difference of $\sim$ 1 meV per formula unit (meV/f.u.) is found between the nonpolar tetragonal and polar orthorhombic structures, which is a key characteristic of antiferroelectricity [88, 114, 115, 138]. It is shown with a Landau-Devonshire model that the requisite first-order transition between nonpolar and polar phases, which in the present case, atypically for antiferroelectrics, have a group-subgroup relation, results from coupling to other zone-boundary modes. This novel mechanism for antiferroelectricity provides a basis for broader searches for antiferroelectric materials with optimal functional properties. In addition, it is demonstrated that the polar phase of ZrO_2 can

be stabilized through epitaxial strain, and the possibility of ferroelectricity in the solid solution $(Zr_{1-x}Hf_x)O_2$ is discussed.

7.2 Technical details

Density-functional calculations are performed using version 7.4.1 of `ABINIT` [30] and the local-density approximation (LDA). A plane-wave energy cutoff of 680 eV, and a $4\times4\times4$ Monkhorst-Pack sampling of the Brillouin zone [25] are used for all structural optimizations. Polarization was calculated on a $10 \times 10 \times 10$ grid using the modern theory of polarization [22] as implemented in `ABINIT`. Norm-conserving pseudopotentials are used from the Bennett-Rappe library [68] with reference configurations: *Zr* ($[Kr]4d^05s^0$), *Hf* ($[Xe]4f^{14}5d^{0.5}6s^0$) and *O* ($[He]2s^22p^4$), generated by the `OPIUM` code [108].

7.3 First principles results

Table 7.1 reports relaxed bulk energies and lattice constants for the experimentally observed bulk phases of ZrO_2. Our results are in good agreement with previous first principles results [139–142]. The monoclinic phase is the lowest energy structure, consistent with experiments. Experimental lattice constants [136, 143–145] are underestimated by 1 %, typical for LDA. The spontaneous polarization of the orthorhombic structure was found to be $P_r \sim 58\ \mu C/cm^2$.

The energy-lowering distortions of the cubic phase of ZrO_2 are discussed first. The zone-boundary X_2^- mode corresponds to an antipolar displacement of oxygen atoms in the $\hat{x}$ direction. It is the single instability exhibited in the first-principles phonon dispersion of the high-symmetry cubic structure [146] and, as mentioned above, leads to the tetragonal $P4_2/nmc$ phase with amplitude 0.319 Å and 4-fold axis along $\hat{x}$. It is found that the tetragonal structure is a local minimum, with no unstable modes. Therefore, even though the polar orthorhombic $Pca2_1$ phase can be obtained by symmetry-breaking distortions of the tetragonal phase, the field-induced transition is expected to be first order.

Table 7.1: Energy $\Delta E = E_{cubic} - E_{phase}$ (meV/f.u.), volume expansion $\Delta V/V$ (%) and lattice parameters (latt.) in Å (β: monoclinic angle) of the experimental phases of ZrO_2. (*a*) Refs. [141, 142], (*b*) Refs. [136, 143–145].

Phase	ΔE	$\Delta V/V$	latt.	This work	Prev. work[a]	Exp.[b]
$Fm\bar{3}m$	0	0	a_0	5.03	5.04	5.03
$P4_2/nmc$	-47.8	2.0	a	5.04	5.03	5.09
			c	5.12	5.10	5.19
$Pca2_1$	-48.2	3.6	a	5.22	5.26	5.26
			b	5.02	5.07	5.07
			c	5.04	5.08	5.08
$P2_1/c$	-82.0	7.2	a	5.09	5.11	5.14
			b	5.20	5.17	5.20
			c	5.24	5.27	5.31
			β	99.39^o	99.21^o	99.17^o

Table 7.2: Wave-vector (q) in reciprocal lattice units ($2\pi/a_0$) and eigenvector of the structural modes contained in the $Pca2_1$ structure, specified by the independent non zero displacements. With Zr at the origin, O_1 at $a_0/4(111)$ and O_2 at $a_0/4(1\bar{1}1)$. Q_{th} and Q_{ex} are the computed and experimental mode amplitudes, defined as described in the text.

	Γ_4^-	X_2^-	$X_{5,x}^+$	$X_{5,y}^+$	$X_{5,z}^+$	X_5^-		X_3^-
q	$\hat{0}$	$\hat{x}$	$\hat{z}$	$\hat{x}$	$\hat{y}$	$\hat{z}$		$\hat{y}$
Zr	u_z	0	0	0	0	0	u_x	u_y
O_1	$-u_z$	$-u_x$	$-u_x$	u_y	u_z	u_y	0	0
O_2	$-u_z$	u_x	$-u_x$	u_y	$-u_z$	$-u_y$	0	0
Q_{th}	0.259	0.499	0.377	0.394	0.392	0.119	0.159	0.089
Q_{ex}	0.233	0.491	0.335	0.376	0.381	0.111	0.158	0.086

The distortion relating the tetragonal $P4_2/nmc$ structure to the polar orthorhombic $Pca2_1$ phase can be decomposed into symmetry-adapted modes of the high-symmetry cubic $Fm\bar{3}m$ structure. Mode amplitudes are computed with respect to eigenvectors normalized to 1 Å. Table 7.2 shows excellent agreement between first principles (Q_{th}) and experimental (Q_{ex}) values of the mode amplitudes. There are four nonzero modes in addition to the X_2^- mode: Γ_4^-, X_5^+, X_5^- and X_3^-. The zone-center Γ_4^- mode corresponds to a polar displacement of the zirconium atoms relative to the oxygen atoms in the $\hat{z}$ direction. The zone-boundary X_5^+ mode has three components, and each involves an antipolar displacement of planes of oxygen atoms. The amplitudes of the X_5^- and X_3^- modes are relatively small.

7.3.1 Energy barrier

The field-induced tetragonal-to-orthorhombic transition is explored by performing relaxations of the structures obtained by linear interpolation of the atomic positions, holding fixed the value of the polar mode amplitude $Q_{\Gamma_4^-}$. Fig. 7.2 shows the energy of the polar structure as a function of $Q_{\Gamma_4^-}$. For small values of $Q_{\Gamma_4^-}$, the energy of the system increases, as expected for freezing in a stable mode. The induced polar structure has an orthorhombic space group *Aba2*, different from that of the polar orthorhombic $Pca2_1$ phase, and relaxes back to the tetragonal phase if the constraint is removed. At $Q_{\Gamma_4^-} \sim 0.134$ Å, it is found an energy cusp with magnitude δE $\sim$ 35 meV/f.u., which separates the *Aba2* structure with $Q_{X^+_{5,y}} \neq 0$ and $Q_{X^+_{5,x,z}} = 0$, from the $Pca2_1$ phase with $Q_{X^+_{5,x,y,z}} \neq 0$. Above this threshold value, the system volume expands ($\sim$ 1.5 %), and the structure relaxes to the polar orthorhombic $Pca2_1$ phase if the constraint is removed. Assuming that the critical field E_C required to overcome the energy barrier is given by $E_C \sim \delta E / V_C P_C$ (with $P_C = 36$ μC/cm^2 and V_C=32.9 Å^3/f.u., the first principles values of polarization and volume at the barrier), the critical field is estimated as $E_C \sim 4.7$ MV/cm.

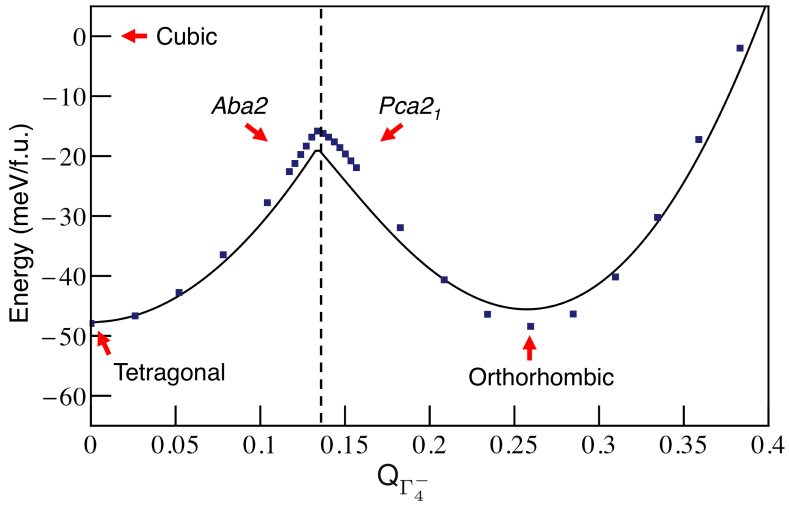

Figure 7.2: First-principles calculations (squares) and Landau-Devonshire model (solid line) of the energy profile between tetragonal and orthorhombic phases.

7.3.2 Landau-Devonshire model

In order to characterize this unusual energy surface, a Landau-Devonshire model has been constructed based on an expansion around the minimum-energy tetragonal $P4_2/nmc$ structure using modes of the high-symmetry $Fm\bar{3}m$ structure as a basis set:

$$E_T(Q_{\Gamma_4^-}, Q_{X^+_{5,a,b,c}}) = E_T^0 + a_1 Q^2_{\Gamma_4^-} + a_2 Q_{\Gamma_4^-} Q_{X^+_{5,y}} + S(Q_{X^+_{5,x}}, Q_{X^+_{5,y}}, Q_{X^+_{5,z}}),$$

where S is a function to be determined below. The invariance of the term $a_2 Q_{\Gamma_4^-} Q_{X^+_{5,y}}$ originates in the fact that the expansion is around a structure of lower symmetry than the structure used to construct and label the modes.

The values of the coefficients are obtained by fitting the model to first principles calculations. By freezing in $Q_{\Gamma_4^-}$ in the tetragonal phase, and relaxing the structure with $Q_{X^+_{5,y}}$ constrained to zero, the values of E_T^0 and a_1 are extracted (Fig. 7.4 (a)). For the two sets of structures obtained by freezing in $Q_{X^+_{5,y}}$, and separately $Q_{X^+_{5,x}}$=$Q_{X^+_{5,y}}$=$Q_{X^+_{5,z}}$, and relaxing, the energies and the relaxed values of $Q_{\Gamma_4^-}$ are obtained. By fitting the relaxed values of $Q_{\Gamma_4^-}$ to the expression $Q_{\Gamma_4^-}$=$-(a_2/2a_1)Q_{X^+_{5,y}}$ obtained for both structures by minimizing Eq. (1) with respect to $Q_{\Gamma_4^-}$, the value of a_2 is extracted (Fig. 7.4 (b)). Finally, the computed energies of these two sets of structures is used to obtain $S(0,Q,0)$=a_3Q^2 and $S(Q,Q,Q)$ as a spline interpolation (Fig. 7.4 (c)).

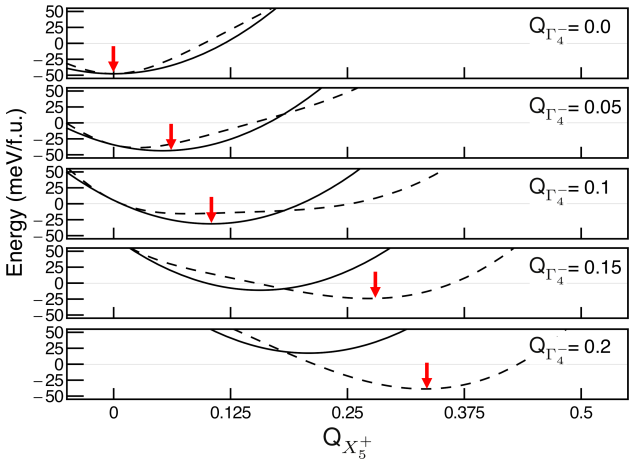

Figure 7.3: Energy (E_T) as a function of $Q_{X^+_{5,y}} = Q_{X_5^+}$ (solid line) and $Q_{X^+_{5,x,y,z}} = Q_{X_5^+}$ (dashed line) at fixed values of the mode amplitude $Q_{\Gamma_4^-}$. The red arrows show the global energy minimum for each value of $Q_{\Gamma_4^-}$.

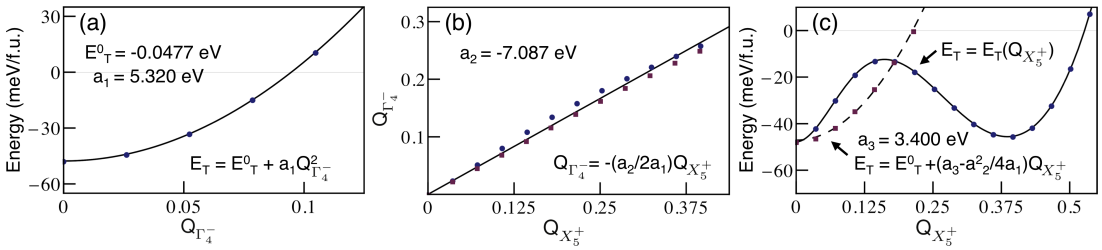

Figure 7.4: First-principles calculations (circles and squares) and model fitting (solid and dashed lines). (a) Energy of the polar *Aba2* structure as a function of $Q_{\Gamma_4^-}$ with $Q_{X_{5,y}^+}$=0. (b) $Q_{\Gamma_4^-}$ as a function of $Q_{X_{5,x,y,z}^+}$=$Q_{X_5^+}$ (circles) and $Q_{X_{5,y}^+}$=$Q_{X_5^+}$ (squares) (c) Energy of the polar $Pca2_1$ structure as a function of $Q_{X_{5,x,y,z}^+}$=$Q_{X_5^+}$ (circles) and $Q_{X_{5,y}^+}$=$Q_{X_5^+}$ (squares).

Using the model it is possible to reproduce the energy cusp of Fig. 7.2 by plotting

$$\min_{Q_{X_{5,x,y,z}^+}} E_T(Q_{\Gamma_4^-}, Q_{X_{5,x,y,z}^+}) \tag{7.1}$$

as a function of $Q_{\Gamma_4^-}$. As shown in Fig. 7.2, the model is able to capture the essential elements of the energy landscape: the position and height of the energy barrier, the two local minima and the energy difference between them. The disagreement between first principles and the model can be attributed to the truncation of the expansion in Eq. (1). The cusp is caused by the multiple local minima displayed by the energy as a function of the X_5^+ mode, with a small change in the value of $Q_{\Gamma_4^-}$ causing a switch between two local minima (Fig. 7.3).

7.3.3 Epitaxial strain

The effect of epitaxial strain is investigated on the relative stability of the tetragonal, orthorhombic, and monoclinic phases. Epitaxial strain is simulated through "strained-bulk" calculations [110,111]. The epitaxially (e) strained $Pca2_1$ structure is denoted as $ePca2_1$, and indicate the matching plane by a prefix labelling the normal to the plane (for example, normal vector $\mathtt{t}_a$ yields *a*-$ePca2_1$).

Fig. 7.5 shows the calculated epitaxial strain diagram for ZrO_2. As expected from the dissimilar lattice constants, the equilibrium energy strains (σ) for the three phases

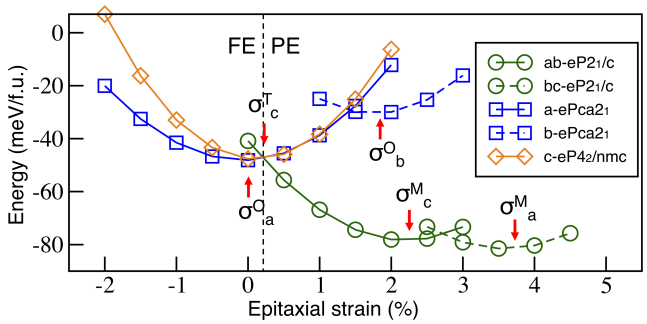

Figure 7.5: Epitaxial strain diagram for ZrO_2. FE and PE refer to ferroelectric and paraelectric ground state.

and various matching planes are quite different (σ_c^M=2.3% and σ_a^M=3.8% for monoclinic, σ_a^O=0.0% and σ_b^O=1.9% for orthorhombic, and σ_c^T=0.2% for tetragonal phases, respectively). The computed values of σ are in excellent agreement with the estimates obtained by comparing the relevant relaxed lattice vectors with the reference lattice constant a_0=5.03 Å, as discussed in [88].

For large values of tensile strain ($> 1\%$), the monoclinic phases are highly favorable in energy. As the strain is decreased, the relative stability of the monoclinic phase is reduced and the tetragonal and orthorhombic phases become favorable. In the strain range from -1.0% to $+1.5\%$, the tetragonal and orthorhombic phases are very close in energy. In this regime, if the appearance of the lower-energy monoclinic phase is suppressed by surface effects [125–127] or other means [147,148], the system is expected to be antiferroelectric. For large values of compressive strain ($< -1\%$), the ferroelectric structure *a-ePca2*$_1$ is favored. While within the accuracy of the calculations it is not possible precisely to predict the critical strains that will be observed in experiments, stabilization of ferroelectricity is expected at accessible values of compressive strain.

7.3.4 Comparison with hafnia (HfO_2)

Finally, as an illuminating comparison with ZrO_2, the stability of the corresponding tetragonal, orthorhombic, and monoclinic structures is considered in HfO_2. The calculated lattice constants for the structures of HfO_2 are shown in Table 7.3. The smaller ion size of Hf^{+4} compared to Zr^{+4} explains the reduced lattice constants of HfO_2, in

Table 7.3: Energy ΔE (meV/f.u.), lattice constants (Å), monoclinic angle (β), and volume expansion $\Delta V/V$ (%) for the ZrO_2-type phases of HfO_2.

Phase	ΔE	a	b	c	β	$\Delta V/V$
Cubic	0	4.89				0
Tetragonal	-22.5	4.90		4.95		1.3
Orthorhombic	-45.1	5.07	4.88	4.89		3.4
Monoclinic	-93.2	4.95	5.06	5.08	99.53^o	7.0

good agreement with previous calculations [149]. The computed spontaneous polarization of 60 μC/cm^2 is consistent with previous results [150]. The main difference between ZrO_2 and HfO_2 is the higher relative energy of the tetragonal structure in HfO_2, so that the polar orthorhombic structure is favored over the nonpolar tetragonal phase by $\sim$ 23 meV/f.u. This suggests that isovalent substitution of Zr by Hf will favor the polar orthorhombic phase in thin films of $(Zr_{1-x}Hf_x)O_2$, consistent with Refs. [56, 134, 135].

Estimation of the minimum energy strains for the relevant structures of HfO_2 gives similar values to the case of ZrO_2 (σ_c^M=2.4% and σ_a^M=3.7% for monoclinic, σ_a^O=$-$0.1% and σ_b^O=$-$1.0% for orthorhombic, and σ_c^T=0.2% for tetragonal structures, respectively). Therefore, the epitaxial strain diagram should be similar to that of ZrO_2 (Fig. 7.5) but with the epitaxial strain curve of the tetragonal structure shifted higher by $\sim$ 23 meV/f.u. Based on this, it is speculated that ferroelectricity would be observed in HfO_2 over a wide range of epitaxial strain if the monoclinic ground state were suppressed.

7.4 Conclusions

In summary, the experimentally observed field-induced ferroelectric transition corresponds to an intrinsic behavior of thin-film ZrO_2. The tetragonal-to-orthorhombic antiferroelectric transition is explained as a field-induced first-order transition where the polar mode is stabilized from the cubic phase by a coupling with two zone-boundary

modes. The results suggest that a ferroelectric phase could be favored over the antiferroelectric phase by appropriate epitaxial strain or isovalent substitution of Zr for Hf. The absence of toxic elements and the compatibility of ZrO_2 with silicon make these results especially relevant for technological applications.

Chapter 8

High-throughput search of antiferroelectric oxides

As a result of the progress in synthesis and first principles methods, there is a strong interest in integrated database first principles methods for the discovery of new functional materials [161]. First principles calculations can efficiently screen and characterize a large family of compounds, selecting promising candidates for experimental verification. In this chapter, a high-throughput search of antiferroelectric materials is presented in the perovskite and other family of compounds.

The ABO_3 perovskites compounds correspond to a large family of oxides with a wide range of functional properties. The well known tendency of this structure to form polar distortions have stimulated an extensive investigation of ferroelectricity in this class of materials [3, 4]. The versatility of the ABO_3 perovskite structure is characterized by a high tunability of its ground state. Epitaxial strain and chemical modification are traditionally the main routes to control dielectric properties and engineer optimal functional properties in perovskites [7].

As mentioned earlier, bismuth ferrite ($BiFeO_3$) is a well known multiferroic with a rhombohedral *R3c* $LiNbO_3$-structure type ground state. However, antiferroelectric double hysteresis loops has been observed in rare-earth substituted $(RE_xBi_{1-x})FeO_3$, with RE: Sm, Gd, Dy [50]. At room temperature, a structural transition from a rhombohedral ferroelectric phase to an orthorhombic paraelectric phase is observed with decreasing average ionic radii of the A-site cation. At the phase boundary, the orthorhombic phase exhibits double hysteresis loops and enhancement of electromechanical properties independent of the rare earth dopant species.

First principles calculations established a small energy difference between the orthorhombic *Pnma* structure and the rhombohedral *R3c* ground state in pure $BiFeO_3$.The

origin of the double hysteresis is explained by the small free energy difference between these phases at the phase boundary, allowing a field-induced transition from the orthorhombic *Pnma* structure to a ferroelectric phase, isostructural with pure $BiFeO_3$.

8.1 Technical details

First principles total-energy calculations were performed using projector augmented-wave (PAW) pseudopotentials [28, 29] and the local spin density approximation [15] plus Hubbard U (LSDA+U) method [162] as implemented in version 5.3.2 of `VASP` [32, 163, 164]. Weakly correlated f orbitals were treated as part of the core with using the generalized gradient approximation plus Hubbard U method (GGA+U) [18, 19]. In a few cases, the pseudopotential was not available and f electrons were calculated with the LSDA+U method. The effect of magnetism is considered secondary and therefore all magnetic calculations are carried using a G-type antiferromagnetic order and standard on-site Coulomb interaction U=5.5, 2.5 and 6.5 eV for $3d$, $4d-5d$ and $4f$ orbitals, with exchange parameter J=0.8 eV.

A plane-wave energy cutoff of 500 eV and a $4 \times 4 \times 4$ Monkhorst-Pack sampling of the Brillouin zone [25] were used for all structural optimizations. Energy band gaps and total polarizations were calculated on a denser $10 \times 10 \times 10$ grid. The dielectric matrix constant and polarization were calculated using perturbation density functional theory [20] and the modern theory of polarization [22], respectively, as implemented in `VASP`.

8.2 Orthorhombic ABO_3 as perovskite antiferroelectrics

The orthorhombic *Pnma* $GdFeO_3$-structure type is the most common ground state among distorted perovskites [73]. Its centrosymmetric structure is derived from the reference unit cell through rotations of the oxygen octahedron cage, denoted as $a^-a^-c^+$ in Glazer notation and shown in Fig. 8.1. The rotation pattern allows an antipolar displacement of the A-site cations that further decreases the energy of the structure.

ABO_3 compounds with *Pnma* structure have typically a cubic perovskite structure with a tolerance Goldsmith factor τ in the range $0.75-1.00$, which favors a centrosymmetric, instead of a polar, ground state.

Recently, several perovskites compounds with orthorhombic *Pnma* structure have been referred as antiferroelectrics [167]. This denotation relies in the observation that artificial suppression of the antipolar A-site cation displacement would favor the stabilization of a low-energy metastable ferroelectric phase [168]. This ferroelectric phase has a rhombohedral *R3c* $LiNbO_3$-structure type and corresponds to a polar distortion of the reference cubic structure in the $\langle 111 \rangle$ cubic direction, accompanied by a $a^-a^-a^-$ octahedron rotation pattern.

Experimentally, only a few materials stabilize in the *R3c* $LiNbO_3$-structure type in pure form. Stabilization of polar rhombohedral ABO_3 compounds has been pursued through chemical modification and applied fields [165], producing large polarization, comparable to that of $PbTiO_3$. As an example, the prototypical antiferroelectric $PbZrO_3$ [2] transforms from its nonpolar *Pbam* ground state to a rhombohedral structure, isostructural to $LiNbO_3$, through a high electric field [74] or under 5 % Ti substitution in the $PbZr_{1-x}Ti_xO_3$ system [77, 178].

However, a nonpolar ground state and a metastable polar phase are not sufficient condition for antiferroelectricity. As is emphasized earlier in section 4.3, the appearance of the double hysteresis loops requires a small energy difference between the competing structures. Furthermore, little has been reported about the response of these orthorhombic materials to an applied electric field. Double hysteresis loops, characteristic of antiferroelectricity, have been measured in orthorhombic Sm, Gd and Dy doped $BiFeO_3$ [50] and in thin-film $BiCrO_3$ [169]. In the case of $BiFeO_3$, the small energy difference between the orthorhombic *Pnma* metastable phase and the rhombohedral *R3c* ground state allows a stabilization of the *Pnma* structure under chemical modification. This suggest that an analogous stabilization of the polar *R3c* structure can be achieved out of orthorhombic *Pnma* materials by the same procedure, suggesting that many other perovskites can be driven to previously-unrecognized antiferroelectric

phases.

Antiferroelectrics have recently been the subject of increasing interest [5]. The characteristic electric-field-induced transition from a nonpolar to a strongly polar phase is the source of functional properties and promising technological applications. Non-linear strain and dielectric responses due to the phase switching are useful for transducers and electro-optic applications [98, 99]. The shape of the double hysteresis loop suggests applications in high-energy storage capacitors [100,101]. In addition, an electro-caloric effect can be observed in systems with a large entropy change between the two phases [59].

While most attention has focused on traditional antiferroelectric perovskites such as $PbZrO_3$ [6] and non-lead containing compounds [7], a recent theoretical materials design search [137] suggested that there are many more antiferroelectric compounds to be discovered. Evidence is starting to emerge that antiferroelectricity requires a small energy difference, on the order of $\sim$ 1 meV/f.u., between the competing nonpolar and polar phases [88,89]. First principles screening of experimentally reported orthorhombic perovskites can shed light onto specific compounds satisfying the necessary conditions for antiferroelectricity, selecting promising candidates for targeted experimental investigation.

In this work, a first-principles high-throughput search of ABO_3 perovskite antiferroelectrics is presented. Structural parameters, nonpolar and polar distortions, band gaps, and energy differences are computed for a search set comprising 250 ABO_3 compounds experimentally reported with the orthorhombic *Pnma* $GdFeO_3$-structure type. A number 20 promising pure materials are identified for which both the ferroelectric and antiferroelectric phases are insulating and have an energy difference below 100 meV/f.u. The antiferroelectric energy barrier in these compounds are estimated through first principles calculations. In addition, it is shown that antiferroelectric properties can be identified through epitaxial strain. Using a simple linear interpolation antiferroelectric phases are predicted through the formation of solid solutions with ABO_3 compounds experimentally reported with the rhombohedral *R3c* $LiNbO_3$-structure type.

Table 8.1: Perovskite compounds experimentally reported as *R3c* in pure form or under an external effect. In bold, compounds that have also been reported as *Pnma* in pure form or under an external effect. Lattice constant a (Å), polarization P ($\mu C/cm^2$) and energy gap E_g (eV) of the *R3c* structure. Energy $\Delta E = E_{Pnma} - E_{R3c}$ (eV/f.u.) and volume $\Delta V/V$ (%) difference between the *Pnma* and *R3c* structures. Refs. (a-l) correspond to [155, 179–189] and − represent no entry in ICSD.

ABO_3	a_{th}	a_{ex}	E_g	P	ΔE	$\Delta V/V$
$BiInO_3$	4.13	−	3.036	84	4.1	4.57
$NaNbO_3$	3.89	3.93[a]	2.695	43	1.1	1.74
$BiFeO_3$	3.90	3.94[b]	2.107	91	16.5	2.69
$BiCoO_3$	3.71	−	1.272	36	18.6	-2.74
$HgTiO_3$	3.86	3.88[c]	1.516	18	34.1	0.98
$LiNbO_3$	3.84	3.88[d]	3.437	75	136.1	0.32
$LiTaO_3$	3.84	3.87[e]	3.723	56	94.5	-0.14
$PbHfO_3$	4.08	4.11[f]	2.888	50	12.2	1.36
$PbZrO_3$	4.11	4.10[g]	2.928	59	26.2	1.73
$ZnSnO_3$	3.91	3.94[h]	1.426	64	189.6	2.14
$MnTiO_3$	3.82	3.87[i]	2.020	81	54.3	4.05
$AgTaO_3$	3.92	3.94[j]	-	0	10.5	0.23
$CuTaO_3$	3.93	3.91[k]	0.779	0	90.3	-2.20
$ScFeO_3$	3.85	3.93[l]	2.551	40	813.8	15.59

Our search set of candidate $GdFeO_3$-type antiferroelectrics consists of ABO_3 compounds drawn from the *Inorganic Crystal Structural Database* (ICSD) [170]. The ICSD includes approximately 250 oxide perovskites reported with the orthorhombic *Pnma* structure. In the calculations, all the compounds observed in the $GdFeO_3$-structure and the $LiNbO_3$-structure are included in either pure form or through an external effect such as pressure, chemical modification, solid solution or size effect. All the orthorhombic compounds considered are insulating, with a balanced total charge state.

Table 8.1 shows compounds reported with the rhombohedral *R3c* $LiNbO_3$ structure type as the ground state. The computed structural parameters of the rhombohedral structure show good agreement with experimental values, with a 1% underestimate of lattice constants characteristic of LDA calculations. The calculations agree with the experimental determinations of the ground state structure. The only exceptions are $ZnSnO_3$ and $MnTiO_3$, which have an ilmenite ground state. It is also noted that $AgTaO_3$ and $CuTaO_3$ are ferroelectric under pressure, and relax to the nonpolar $R\bar{3}c$

Table 8.2: Perovskite compounds experimentally reported as *Pnma* in pure form or under an external effect. Calculated reference lattice constant a_0 (Å). Energy $\Delta E = E_{Pnma} - E_{R3c}$ (eV/f.u.) and volume $\Delta V/V$ (%) difference between the *Pnma* and *R3c* structures. Polarization P ($\mu C/cm^2$) and indirect energy band gap E_g (eV) of the *R3c* structure. Calculated dielectric constant ϵ of the *Pnma* structure. Estimated polarization P_b at the antiferroelectric energy barrier E_b.

ABO_3	a_0	ΔE	$\Delta V/V$	E_g	P	ϵ	P_b	E_b
$CaTiO_3$	3.81	-73.1	1.42	2.71	44	43	21	82.6
$CdSnO_3$	3.98	-38.6	2.39	0.92	35	48	19	68.6
$BaThO_3$	4.54	-54.4	0.71	3.69	16	62	16	54.4
$CaZrO_3$	4.07	-66.5	2.77	4.44	53	40	25	148.8
$CdTiO_3$	3.81	-46.1	2.40	2.49	53	48	21	69.4
$NaTaO_3$	3.92	-24.3	1.28	2.87	23	19	7	26.2
$SrZrO_3$	4.10	-51.1	0.57	3.73	12	33	13	51.1
$MgSiO_3$	3.48	-96.1	2.89	5.83	54	10	17	202.5
$SrCeO_3$	4.34	-87.0	2.01	2.25	34	38	20	123.1
$BiCrO_3$	3.82	-41.1	1.58	2.28	67	42	23	109.2
$BiRhO_3$	3.89	-57.4	0.68	0.81	35	167	34	57.6
$SrPrO_3$	4.43	-61.9	2.17	2.14	32	70	22	81.4
$LaLuO_3$	4.22	-87.1	2.69	4.42	53	42	25	160.0
$LaTmO_3$	4.26	-63.3	3.00	4.31	57	49	27	163.0
$EuZrO_3$	4.13	-72.6	1.68	4.09	37	36	19	92.7
$LaErO_3$	4.29	-48.8	3.12	4.25	59	53	28	164.0

structure. In bold are highlighted compounds that have also been experimentally observed in the orthorhombic *Pnma* structure under some external effect, such as pressure in the case of $BiInO_3$ [171] and $BiCoO_3$ [172], or chemical modification such as $BiFeO_3$ [50] and $NaNbO_3$ [173].

For each orthorhombic ABO_3 perovskite in the search set, structural parameters are optimized for the three structures: $GdFeO_3$ (*Pnma*), $LiNbO_3$ (*R3c*), and $CaTiO_3$ ($Pm\bar{3}m$). The most promising candidate antiferroelectrics, shown in Table 8.2, fulfill the following criteria: a) the ground state is experimentally reported with the nonpolar orthorhombic *Pnma* $GdFeO_3$ structure type, b) the polar *R3c* $LiNbO_3$ structure type is metastable with an energy difference smaller than 100 meV/f.u. with respect to the ground state, and c) both phases are insulating, with an energy band gap $E_g > 0.01$ eV.

The orthorhombic and rhombohedral structures correspond to small distortions of the reference perovskite structure, these distortions can be decomposed into symmetry

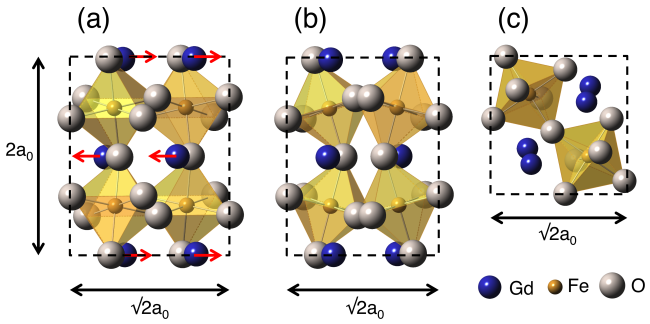

Figure 8.1: Crystal structure of the *Pnma* $GdFeO_3$-structure type. (a), (b) and (c) correspond to views along the $\hat{x}$, $\hat{y}$ and $\hat{z}$ lattice vectors.

adapted modes. The orthorhombic structure contains zone-boundary modes with R_4^+ and M_3^+ symmetry. These modes generates octahedral rotations around the $\langle 110 \rangle$ and $\langle 001 \rangle$ cubic directions. The rotation pattern allows a zone-boundary X_5^+ mode corresponding to an antipolar displacement of the A-site cations in the $\langle 110 \rangle$ cubic axis, as shown in Fig. 8.1. The rhombohedral ferroelectric phase is obtained through a polar distortion with Γ_4^- symmetry, corresponding to a diagonal displacement of the A and B cations against the oxygen cage in the $\langle 111 \rangle$ direction, this zone center mode is accompanied by a zone boundary with R_5^- symmetry and an $a^-a^-a^-$ oxygen octahedron rotation.

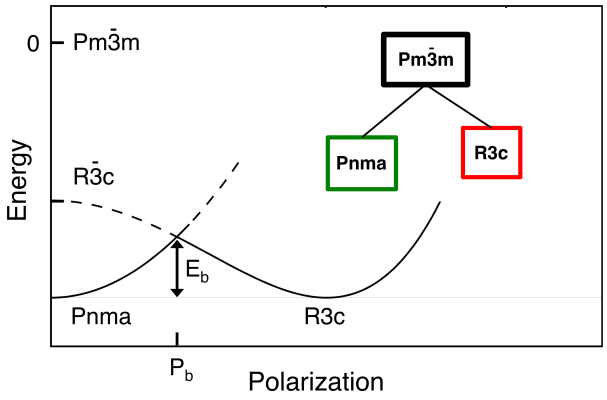

Figure 8.2: Diagrammatic representation of the energy barrier between the nonpolar orthorhombic and polar rhombohedral phases.

The energy landscape separating the orthorhombic and rhombohedral phases is explored. The energy versus polarization diagram is represented in Fig. 8.6, where P_b and E_b correspond to the position and height of the energy barrier. At the polarization

threshold P_b, the induced polar orthorhombic structure with $a^-a^-c^+$ rotation pattern undergoes a first order transition to the polar rhombohedral phase with $a^-a^-a^-$ rotation pattern.

The value of P_b and E_b are estimated for each specific material using first principles. As a function of polarization, the energy of the orthorhombic structure can be described by $E_O(P) = E_{Pnma} + (1/2)\alpha_O P^2$, where E_{Pnma} is the energy of the orthorhombic $Pnma$ phase, $\alpha_O = \epsilon/(\epsilon - \epsilon_0)^2$ and ϵ is the maximum of the diagonal dielectric constants $\epsilon_{\alpha\alpha}$. The energy of the rhombohedral phase as a function of polarization can be described by $E_R(P) = E_{R\bar{3}c} + \alpha_R P^2 + \beta_R P^4$. The auxiliary reference structure $R\bar{3}c$, with energy $E_{R\bar{3}c}$, has a centrosymmetric rhombohedral $NdAlO_3$-structure type.

8.2.1 Epitaxial strain

Next, the effect of epitaxial strain is investigated on the relative stability of the orthorhombic (O) and rhombohedral (R) phases. Epitaxial strain is simulated through "strained-bulk" calculations [110, 111]. The position of the equilibrium energy strain $\sigma^{(O,R)}$, reported in Table 8.3, are obtained by comparing the relevant relaxed lattice vectors with the reference lattice constant a_0, as discussed in [88]. The matching plane of the orthorhombic structure is indicated by a prefix labelling the corresponding normal vector.

In ferroelectric compounds such as $BaTiO_3$, competing ground states have large $\Delta\sigma > 1$ values, so that different polar structures are favored at different values of epitaxial strain [111]. For antiferroelectrics, a small energy difference ΔE and small $\Delta\sigma < 1$ are expected, a signature of competition between the polar and nonpolar structures in a certain range of epitaxial strain [88].

8.2.2 Chemical modification

Finally, the effect of isovalent substitution is investigated through the formation of solid solutions. The energy difference between the orthorhombic and rhombohedral

Table 8.3: Effect of epitaxial strain in antiferroelectric candidates. Reference lattice constant a_0 (Å) and differences on equilibrium energy points between orthorhombic and rhombohedral structures.

ABO$_3$	a_0	$\sigma_c^O - \sigma^R$	$\sigma_{ab}^O - \sigma^R$
$CaTiO_3$	3.81	0.36	0.55
$NaNbO_3$	3.92	1.35	1.30
$BaThO_3$	4.54	-0.37	-0.19
$NaTaO_3$	3.92	0.99	0.94
$SrZrO_3$	4.10	-0.28	-0.13
$BiFeO_3$	3.85	0.77	1.14
$SrCeO_3$	4.34	0.71	0.87
$BiCrO_3$	3.82	0.2	0.36
$SrPrO_3$	4.43	1.34	1.38
$EuZrO_3$	4.13	0.7	0.87

phases at a isovalent substitution x is estimated through a linear interpolation $\Delta E = (1-x)\Delta E_1 + x\Delta E_2$, where ΔE_1 and ΔE_2 correspond to the energy differences of the end point compounds with x=0 and x=1. In the linear model, depicted in Fig. 8.3, an antiferroelectric phase is expected at the critical isovalent substitution x_c where $\Delta E \sim 1$ meV/f.u. The volume difference between the competing phases, polarization of the polar phase and critical electric field at the critical substitution x_c are reported in Table 8.4. The critical electric field is estimated by assuming $E_c \sim \Delta E / V_c\ P_c$ at the critical substitution x_c, where the of V_c and P_c is approximated by the volume and polarization of the relaxed rhombohedral structure.

Experimental information regarding the substitutional system of Table 8.4 is very limited. The competition between ferroelectricity and antiferroelectricity has been studied in the (Pb,Sr)ZrO_3 and (Pb,Ba)ZrO_3 substitutional systems [47]. Above 100^{o}C, an antiferroelectric phase is observed at 25% substitution of Sr for Pb. The structure of the antiferroelectric phase is unknown, but different from the *Pbam* ground state of $PbZrO_3$.

The linear model is consistent with the experimental results of Bi(Fe,Sm)O_3. In this case, the model predicts an structural transition at 9%, whereas experimentally, the phase boundary is located at 14% substitution. The value of the critical electric field is also consistent with the value obtained experimentally.

Table 8.4: Solid solutions with *Pnma* and *R3c* compounds as an end point. Critical isovalent substitution x_c, volume difference $\Delta V/V$, polarization P and critical field E_c at the critical substitution x_c.

ABO$_3$	x_c	$\Delta V/V(x_c)$	$P(x_c)$	$E_c(x_c)$
(Zn,Cd)SnO$_3$	0.83	2.35	40	6.7
(Pb,Ca)ZrO$_3$	0.29	2.03	57	4.2
(Pb,Sr)ZrO$_3$	0.35	1.32	42	5.6
(Pb,Eu)ZrO$_3$	0.28	1.72	53	4.4
(Li,Na)TaO$_3$	0.80	1.00	29	9.7
(Bi,Na)TaO$_3$	0.08	1.70	41	6.8
Bi(In,Cr)O$_3$	0.11	4.24	82	2.9
Bi(In,Rh)O$_3$	0.08	4.25	80	2.9
Bi(Co,Cr)O$_3$	0.33	-1.32	46	6.4
Bi(Co,Rh)O$_3$	0.26	-1.86	36	8.4
Bi(Fe,Cr)O$_3$	0.30	2.35	84	3.3
Bi(Fe,Rh)O$_3$	0.24	2.21	77	3.5
(Bi,Tl)FeO$_3$	0.28	2.66	65	4.2
(Bi,Sm)FeO$_3$	0.09	2.54	82	3.0
(Hg,Ca)TiO$_3$	0.33	1.12	26	11.0
(Hg,Cd)TiO$_3$	0.44	1.60	33	8.8
(Mn,Ca)TiO$_3$	0.43	2.91	65	4.7
(Mn,Cd)TiO$_3$	0.55	3.14	65	4.6

For completeness, compounds with toxic elements such as Hg, Cd and Tl are included, although these have only academic importance. Further experimental investigation of the present systems is suggested in order to corroborate the first principles results.

8.3 Ferroic order in orthorhombic *AXY* compounds

The search for antiferroelectric materials outside the perovskite family of compounds is briefly described in the *AXY* system. As described in section 7, first-principles calculations established that antiferroelectricity corresponded to an intrinsic property of tetragonal thin film ZrO_2, and suggested the stabilization of ferroelectricity in HfO_2 upon suppression of the monoclinic ground state [89]. These results stimulates the exploration of compounds with similar polar orthorhombic structure in the wider class of *AXY* compounds with X and Y either oxygen, fluorine or sulfur.

Unlike other known antiferroelectrics, the field induced ferroelectric phase of ZrO_2,

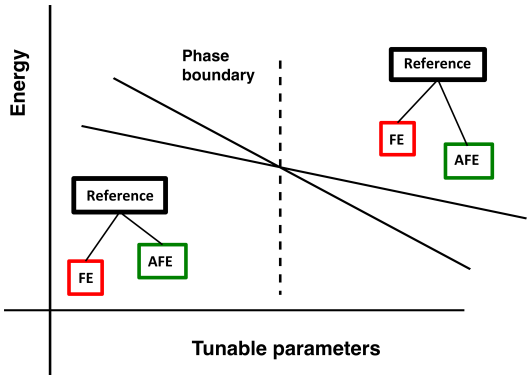

Figure 8.3: Linear energy model interpolating ferroelectric and antiferroelectric compounds. Possible tunable parameters include epitaxial strain, pressure and chemical modification.

with structure $Pca2_1$ [136], arises through couplings between the polar mode and zone-boundary modes. This novel mechanism represents a new class of antiferroelectrics, and possibly of ferroelectrics. In the case of HfO_2, the polar orthorhombic $Pca2_1$ structure lies 48 meV/f.u. above the monoclinic $P2_1/c$ ground state. This suggests that tuning of the energy difference between the polar and nonpolar structures through an external mean could lead to competition, a signature of antiferroelectricity.

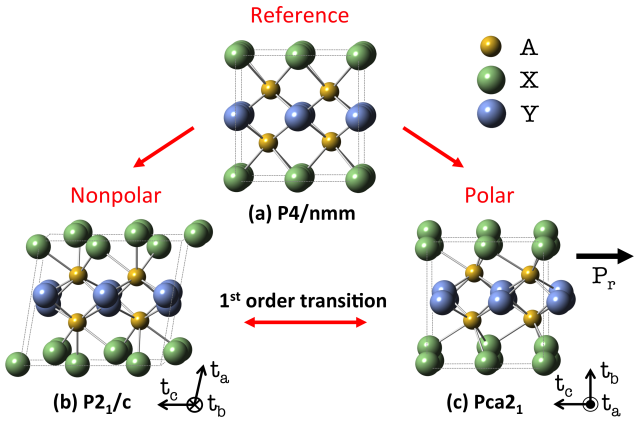

Figure 8.4: AXY Antiferroelectric class: (a) Reference structure ($P4/nmm$), (b) Monoclinic ($P2_1/c$) and (c) Orthorhombic ($Pca2_1$).

Oxyfluorides display functional properties such as ferroelectricity and ferromagnetism [166]. Nitrogen and sulfur are commonly used to enhance ferroelectric properties in oxides. Oxygen has a similar ion radius and/or electron affinity as fluorine (F), nitrogen (N) and sulfur (S), making these elements specially suitable to study the relative

stability of structures as a function of ion size and oxidation state. Analogously to the case of orthorhombic perovskites, tuning parameters such as epitaxial strain, chemical modification and size effects can be used to enhanced antiferroelectric properties.

The generalization of the structure types of ZrO_2 to the AXY stoichiometry with X≠Y are shown in Fig. 8.4. The space group symmetry of the polar orthorhombic ($Pca2_1$) and monoclinic ($P2_1/c$) structures remains unchanged when three different atoms are considered for the three different Wyckoff positions. The Wyckoff positions of the low-symmetry orthorhombic and monoclinic structures determine the high-symmetry reference structure as tetragonal, with space group *P4/nmm* (129). While the reference structure has been observed experimentally for *LaOF* and *YOF* [174], the monoclinic $P2_1/c$ structure has been observed experimentally for *ScFO*, *YbOF*, *TaON* and *NbON*.

Table 8.5: Energy difference $\Delta E = E_{Pca2_1} - E_{P2_1/c}$ (meV/f.u.) between orthorhombic and monoclinic structures and lattice constants (Å) (experimental lattice constants and angles in parenthesis) for AXY compounds reported in the ICSD with experimental monoclinic ground state.

AXY	ΔE	a	b	c	β
HfO_2	51	5.03(5.09)	5.13(5.18)	5.19(5.24)	$99.6^o(99.1^o)$
ScFO	58	5.06(5.17)	5.04(5.15)	5.13(5.25)	$100.3^o(99.7^o)$
YbOF	40	5.53(5.51)	5.39(5.43)	5.50(5.52)	$100.0^o(99.7^o)$
NbNO	140	4.96(4.98)	5.03(5.03)	5.18(5.21)	$100.0^o(100.8^o)$
TaON	179	4.93(4.99)	5.00(5.06)	5.15(5.21)	$99.9^o(99.7^o)$

In this work, a first-principles high-throughput investigation of ferroic order is performed in the AXY family of compounds, with X and Y either O, S, N or F. The relative stability of the polar orthorhombic $Pca2_1$ structure is explored in known and yet unsynthesized compounds. A previously unrecognized class of ferroelectrics is identified, where the orthorhombic $Pca2_1$ structure corresponds to the lowest energy structure and the polar mode is stabilized through coupling with zone-boundary modes. Furthermore, a previously unrecognized class of antiferroelectric compounds is found, where the lowest energy monoclinic $P2_1/c$ structure has a small energy difference with the polar orthorhombic $Pca2_1$ phase, a signature of antiferroelectricity. The corresponding ferroelectric switching field and the antiferroelectric critical field are estimated through first

principles calculations.

Table 8.5 contains AXY compounds reported as ZrO_2-type monoclinic ($P2_1/c$) in the Inorganic Crystal Structure Database (ICSD). The energy difference between orthorhombic and monoclinic structures shows that the monoclinic phase is the lowest energy structure, consistent with experiments. The computed lattice constants underestimate the experimental lattice constants [175–177], reported in parenthesis, by 1 %, typical for LDA.

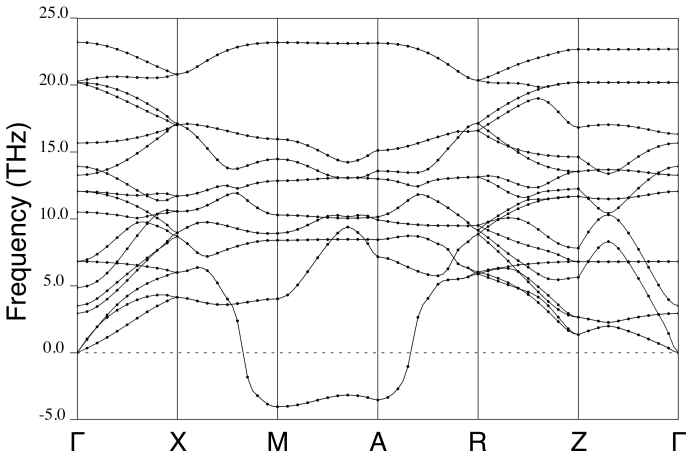

Figure 8.5: First-principles calculation of the phonon spectrum of the reference structure of *ScFO*.

As an example, the particular case of *ScFO* is considered. Fig. 8.5 shows the first-principles phonon spectrum of the high-symmetry *P4/nmm* structure of *ScFO*. As it is shown later, the single instability at the M point is responsible for the stabilization of the orthorhombic and monoclinic structures, which therefore arise through first order transitions.

The distortion that relates the reference structure with the polar orthorhombic structure can be decomposed into symmetry adapted modes. These modes are reported in Table 8.6. The polar orthorhombic structure contains two zone-center modes: Γ_1^+ and Γ_5^-, and two zone-boundary M modes: M_1 and M_4. The polar mode Γ_5^- corresponds to the simultaneous displacement of A and Y atoms against X atoms in the $\hat{z}$ direction. The zone boundary M_4 mode corresponds to an antipolar motion of the X and Y atoms in the $\hat{x}$ direction. Finally, the zone boundary M_1 mode corresponds to an antipolar

Table 8.6: Wave-vector (q) in reciprocal lattice units ($2\pi/a_0$) and eigenvector of the symmetry-adapted structural modes contained in the polar orthorhombic structure $Pca2_1$, specified by the independent non zero displacements. With A at the origin, X at $1/4(1-1-1)$ and Y at $1/4(111)$. Q is the computed mode amplitude, defined as described in the text.

	Γ_1^+	Γ_5^-	M_1			M_4	
$\hat{q}$	$\hat{0}$	$\hat{0}$	$(\hat{x}+\hat{y})/2$			$(\hat{x}+\hat{y})/2$	
A	u_y	0	u_x	0	0	0	0
X	0	u_z	0	u_y	0	u_x	0
Y	0	0	0	0	u_y	0	u_x
Q	0.26	0.60	0.13	0.31	0.18	0.56	0.03

motion of X and Y atoms in the $\hat{y}$ axis, which couple with an antipolar motion of the A atoms in the $\hat{x}$ direction.

Freezing in the unstable M_4 mode in the reference structure leads to a centrosymmetric structure with space group $Pcca$. Simultaneous freezing of M_1 and M_4 breaks inversion symmetry through a trilinear term of the form $\Gamma_5^- M_1 M_4$ and produces the polar orthorhombic $Pca2_1$ structure. The monoclinic structure of *ScFO* lies 50 meV/f.u. lower in energy and is obtained from the reference structure by freezing of the M_1 and M_4 modes, together with a monoclinic distortion of the unit cell produced by the zone-center Γ_5^+ mode.

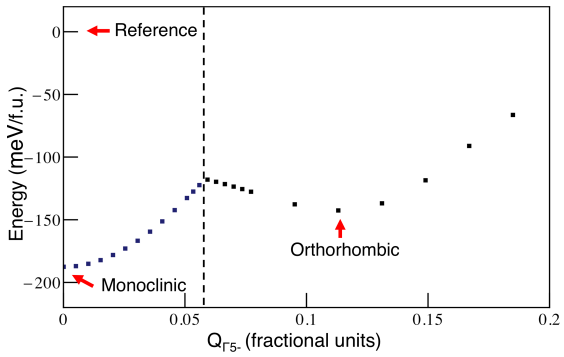

Figure 8.6: First-principles calculation of the energy barrier between the nonpolar monoclinic and polar orthorhombic phases of *ScFO*.

The field-induced monoclinic to orthorhombic transition is explored by performing relaxations of the structures obtained by linear interpolation of the atomic positions, holding fixed the value of the polar mode amplitude $Q_{\Gamma_5^-}$. Fig. 8.6 shows the energy profile of *ScFO* as a function of $Q_{\Gamma_5^-}$. For small values of $Q_{\Gamma_5^-}$, the energy increases, as

expected for freezing in a stable mode. The induced polar structure has a monoclinic space group $P2_1$, different from that of the polar orthorhombic $Pca2_1$ phase, and relaxes back to the monoclinic phase if the constraint is removed. At $Q_{\Gamma_5^-} \sim 0.059$ (fractional units), an energy cusp is found with magnitude δE $\sim$ 70 meV/f.u., which separates the $P2_1$ structure with $\Gamma_5^+ \neq 0$, from the $Pca2_1$ phase with $\Gamma_5^+ = 0$. Above this threshold value, the structure relaxes to the polar orthorhombic $Pca2_1$ phase if the constraint is removed.

Table 8.7: AXY compounds with polar orthorhombic $Pca2_1$ structure as the lowest phase. Energy ΔE (meV/f.u.) difference between polar and nonpolar structures. Polarization P ($\mu C/cm^2$), indirect band gap E_g (eV) and switching energy E_{sw} (eV/f.u.) of the polar phase.

AXY	ΔE	P	E_g	E_{sw}
FeOF	-8	45	1.4	0.45
VON	-14	58	1.2	0.47
BiON	-37	52	0.1	0.42
GaOF	-50	43	2.5	0.92
PbO_2	-63	39	0.1	0.17
SbON	-65	46	0.1	1.16
CrOF	-73	30	2.3	1.23

Table 8.8: AXY compounds with a small energy $\Delta E = E_{Pca2_1} - E_{P2_1/c}$ (meV/f.u.) and volume $\Delta V/V$ (%) difference between polar and nonpolar structures. Polarization P ($\mu C/cm^2$) and indirect band gap E_g (eV) of the polar phase.

AXY	ΔE	P	E_g	$\Delta V/V$
SbOF	21	38	3.4	-2.4
YbOF	40	61	0.9	-2.5
YOF	42	56	5.0	-2.8
InOF	49	87	0.7	-2.4
HfO_2	51	58	4.9	-3.5
ScOF	58	92	4.6	-2.4

The relative stability of the polar orthorhombic $Pca2_1$ and monoclinic $P2_1/c$ structures is considered now for the stoichiometry AXY. It is found that only compounds containing oxygen have the desired properties, and since the oxygen atom has two possible Wyckoff positions in the orthorhombic and monoclinic structures, both cases (AOY

and *AXO*) are considered. It is stressed that the high-symmetry *P4/nmm* reference structure is not require to be either experimentally observable or insulating, and is thus only required that the low-symmetry structures are insulator.

Preliminary results are shown in Table 8.7 and Table 8.8. Table 8.7 reports compounds with the polar orthorhombic structure as the lowest energy structure. Table 8.8 reports compounds with an energy difference $\leq$ 100 meV/f.u. and a volume difference $\leq$ 5% between the polar orthorhombic and monoclinic structures. Analogously to the case of orthorhombic ABO_3 perovskites, optimal antiferroeletric properties are expected experimentally through epitaxial strain or the formation solid solutions.

8.4 Conclusions

In summary, a high-throughput search for more antiferroelectric materials was presented in the perovskite and in the *AXY* family of compounds. The main factor that promotes antiferroelectricity is a small energy difference between the nonpolar and polar structures. Other intrinsic properties of the compounds, such as the antiferroelectric energy barrier, were calculated in order to study possible transition paths. Specific candidates were selected for further experimental verification. Tuning parameters such as epitaxial strain and chemical modification were used to find optimal candidates.

Chapter 9

Conclusions

In the present thesis, a first principles study of the fundamental physics of antiferroelectricity in complex oxides was presented. The effect of epitaxial strain, pressure, and isovalent substitution on the relative stability of the structures and the energy landscape was explored using first principles calculations.

In chapter 2, the basic concepts of density functional theory used throughout the work were briefly reviewed. The theoretical formalism was introduced as well as the numerical techniques used to compute physical properties in solid state physics. Then in chapter 3, the physics of ferroelectricity and antiferroelectricity was described, highlighting different approaches to study real materials.

The difficulties in the formulation of a precise definition of antiferroelectricity in complex oxides arise from the continuous nature of the charge density. Perovskite and other complex oxides display a wide range of structural distortions depending on the specific chemistry of the crystal. It was found that a low-energy metastable ferroelectric phase is a fundamental requirement for the existence of antiferroelectricity.

In chapter 4, the microscopic origin of antiferroelectricity in traditional perovskite antiferroelectrics was investigated. The scarcity of pure antiferroelectric perovskite arises from the small energy difference between the competing nonpolar and polar structures. The relative stability of the competing structures was calculated for several antiferroelectrics using first principles calculations. A remarkably small energy difference on the order of 1 meV/f.u. was found, and established this energy difference as a necessary condition for the observation of antiferroelectric double hysteresis loops.

Perovskite compounds have a complex energy landscape with a rich variety of low-energy structures. In the case of perovskite antiferroelectrics, the small energy difference between nonpolar and polar structures can be explained by a negligible gain of energy for certain oxygen octahedron rotations that connect the nonpolar and polar structures. It was concluded, based on first principles calculations, that oxygen octahedral rotations play an important role in the stabilization of antiferroelectricity in perovskites, by allowing antipolar displacement of A-site cations through anharmonic coupling terms.

In chapter 5, the effect of epitaxial strain in the prototypical antiferroelectric $PbZrO_3$ was explored. It was found that epitaxial strain promote structural and energetic competition between ferroelectricity and antiferroelectricity. In the particular case of $PbZrO_3$, epitaxial strain favors ferroelectricity at compressive strain and antiferroelectricity at tensile strain. The effect of epitaxial strain in highly distorted structures can be estimated from the magnitude of the relaxed lattice vectors. This simple technique was later generalized to identify other antiferroelectric candidates among oxide compounds.

In chapter 7, the work on thin film ZrO_2 was presented. This well known and extensively investigated compound has a wide range of technological applications, and despite its simple structure, still displays a new functional property. Using first principles methods, it was established that antiferroelectricity corresponded to an intrinsic property of the material. The small energy difference between nonpolar and polar structures confirms the experimental observation of double hysteresis loops in thin film form. The energy landscape of the field-induced ferroelectric transition was described with a Landau-Devonshire model.

In chapter 6, the field-induced ferroelectric transition was studied in $NaNbO_3$-based ceramics. The appearance of double hysteresis loops in chemically doped $NaNbO_3$ is explained by the decrease in the energy barrier separating the corresponding nonpolar and polar phases. The small increase in the polarizability of the material, produces a large increase in the rate of antiferroelectric switching, producing coexistence of ferroelectricity and antiferroelectricity.

Finally, in chapter 8, a high-throughput search for more antiferroelectric materials was presented in the perovskite and other families of compounds. Factors that promote antiferroelectricity were identified and specific candidates were selected for further experimental verification. Tuning parameters such as epitaxial strain and chemical modification were used to find optimal candidates and enhanced the properties of interest.

References

[1] C. Kittel, *Theory of antiferroelectric crystals*, Phys. Rev. **82**, 729 (1951).

[2] G. Shirane, E. Sawaguchi, and Y. Takagi, *Dielectric properties of lead zirconate*, Phys. Rev. **84**, 476 (1951).

[3] M. E. Lines, A. M. Glass, *Principles and applications of ferroelectrics and related materials*, Clarendon Press, Oxford, (1977).

[4] K. M. Rabe, Ch. H. Ahn, J. -M. Triscone (Eds.), *Physics of Ferroelectrics: A Modern Perspective*, Springer-Verlag (2007).

[5] K. M. Rabe, *Antiferroelectricity in oxides: a reexamination*, in Functional Metal Oxides: New Science and Novel Applications, Wiley (2013).

[6] H. Liu and B. Dkhil, *A brief review on the model antiferroelectric $PbZrO_3$ perovskite-like material*, Z. Kristallogr. **226**, 163 (2011).

[7] X. Tan, C. Ma, J. Frederick, S. Beckman, and K. G. Webber, *The antiferroelectric $\leftrightarrow$ ferroelectric phase transition in lead-containing and lead-free perovskite ceramics*, J. Am. Ceram. Soc. **94** (12), 4091 (2011).

[8] E. Schrodinger, *An undulatory theory of the mechanics of atoms and molecules*, Phys. Rev. **28**, 1049 (1926).

[9] G. Grosso and G. P. Parravicini, *Solid State Physics*, Academic Press (2000).

[10] M. Born and J. R. Oppenheimer, *On the quantum theory of molecules*, Anna. Phys. **389**, 457 (1927).

[11] R. P. Feynman, *Forces in molecules*, Phys. Rev. **56**, 340 (1939).

[12] M. C. Payne, M. P. Teter, D. C. Allan, T. A. Arias, and J. D. Joannopoulos, *Iterative minimization techniques for ab initio total-energy calculations: molecular dynamics and conjugate gradients*, Rev. Mod. Phys. **64**, 1045 (1992).

[13] P. Hohenberg and W. Kohn, *Inhomogeneous electron gas*, Phys Rev. **136** B864 (1964).

[14] W. Kohn and L. J. Sham, *Self-consistence equations including exchange and correlation effects*, Phys. Rev. **140**, A1133 (1965).

[15] J. P. Perdew and A. Zunger, *Self-interaction correction to density-functional approximations for many-electron systems*, Phys. Rev. B **23** 5048 (1981).

[16] D. M. Ceperley and B. J. Alder, *Ground state of the electron gas by a stochastic method*, Phys Rev. Lett. **45**, 566 (1980).

[17] R. O. Jones and O. Gunnarson, *The density functional formalism, its applications and prospects*, Rev. Mod. Phys. **61** 689 (1989).

[18] J. P. Perdew, K. Burke and M. Ernzerhof, *Generalized gradient approximation made simple*, Phys. Rev. Lett. **77** 3865 (1996).

[19] J. P. Perdew, K. Burke and Y. Wang, *Generalized gradient approximation for the exchange-correlation hole of a many-electron system*, Phys. Rev. B **54** 16533 (1996).

[20] S. Baroni, S. de Gironcoli, A. Dal Corso and P. Giannozzi, *Phonons and related crystal properties from density-functional perturbation theory*, Rev Mod Phys **73** 515 (2001).

[21] R. M. Sternheimer, *Electronic polarizabilities of ions from the Hartree-Fock wave functions*, Phys. Rev. **96**, 951 (1954)

[22] R. D. King-Smith and D. Vanderbilt, *Theory of polarization of crystalline solids*, Phys. Rev. B **47**, 1651(R) (1993).

[23] K. M. Rabe, *Theoretical investigations of epitaxial strain effects in ferroelectric oxide thin films and superlattices*, Current Opinion in Solid State and Materials Science **9**, 122 (2005).

[24] D. G. Schlom, L.-Q. Chen, C.-B. Eom, K. M. Rabe, S. K. Streiffer and J.-M. Triscone, *Strain tuning of ferroelectric thin films*, Annu. Rev. Mater. Res. **37**, 589 (2007).

[25] H. J. Monkhorst and J. D. Pack, *Special points for Brillouin-zone integrations*, Phys. Rev. B **13**, 5188 (1976).

[26] R. M. Martin, *Electronic Structure: Basic Theory and Practical Methods*, Cambridge University Press (2008).

[27] M. S. Dresselhaus, G. Dresselhaus and A. Jorio, *Group theory: Application to the physics of condensed matter*, Springer-Verlag (2008).

[28] P. E. Blochl, *Projector augmented-wave method*, Phys. Rev. B **50**, 17953, (1994).

[29] G. Kresse and D. Joubert, *From ultrasoft pseudopotentials to the projector augmented-wave method*, Phys. Rev. B **59** 1758, (1999).

[30] X. Gonze, B. Amadon, P. Anglade, J. M. Beuken, F. Bottin, P. Boulanger, F. Bruneval, D. Caliste, R. Caracas, M. Cote *et al.*, *ABINIT: First-principles approach to material and nanosystem properties*, Comput. Phys. Commun. **180**, 2582 (2009).

[31] P. Giannozzi *et al.*, *QUANTUM ESPRESSO: a modular and open-source software project for quantum simulations of materials*, J. Phys.:Condens. Matter **21**, 395502 (2009).

[32] G. Kresse and J. Hafner, *Ab initio molecular dynamics for liquid metals*, Phys. Rev. B **47** 558, (1993); G. Kresse and J. Furthmller, *Efficient iterative schemes for ab initio total-energy calculations using a plane-wave basis set*, Phys. Rev. B **54**, 11169 (1996).

[33] ISOTROPY Software Suite, iso.byu.edu.

[34] M. I. Aroyo, J. M. Perez-Mato, D. Orobengoa, E. Tasci, G. de la Flor, A. Kirov, *Crystallography online: Bilbao Crystallographic Server*, Bulg. Chem. Commun. **43**, 183 (2011).

[35] B. A. Strukov and A. P. Levanyuk, *Ferroelectric phenomena in crystals: Physical foundations*, Springer-Verlag, Berlin, (1998).

[36] W. Zhong, D. Vanderbilt, and K. M. Rabe, *Phase transitions in $BaTiO_3$ from first principles*, Phys. Rev. Lett. **73**, 1861 (1994).

[37] W. Zhong, D. Vanderbilt, and K. M. Rabe, *First-principles theory of ferroelectric phase transitions for perovskites: The case of $BaTiO_3$*, Phys. Rev. B **52**, 6301 (1995).

[38] W. Cochran, *Crystal stability and the theory of ferroelectricity*, Phys. Rev. Lett. **3**, 412 (1959).

[39] R. H. Lyddane, R. G. Sachs, and E. Teller, *On the polar vibrations of alkali halides*, Phys. Rev. **59**, 673 (1941).

[40] K. M. Rabe and J. D. Joannopoulos, *Theory of the structural phase transition of GeTe*, Phys. Rev. B **36**, 6631 (1987).

[41] K. M. Rabe and U. V. Waghmare, *Localized basis for effective lattice Hamiltonians: Lattice Wannier functions*, Phys. Rev. B **52**, 13236 (1995).

[42] U. V. Waghmare and K. M. Rabe, *Lattice instabilities, anharmonicity and phase transitions in $PbZrO_3$ from first principles*, Ferro. **194**, 135 (1997).

[43] L. E. Cross, *Antiferroelectric-ferroelectric switching in a simple "Kittel" antiferroelectric*, J. Phys. Soc. Jpn. **23**, 77 (1967).

[44] W. J. Merz, *Double hysteresis loop of $BaTiO_3$ at the Curie point*, Phys. Rev. **91**, 513 (1953).

[45] K. Okada, *Phenomenological theory of antiferroelectric transition. I. Second-order transition*, J. Phys. Soc. Jpn. **27**, 420 (1969).

[46] K. Uchino, L. E. Cross and R. E. Newnham, *Electrostrictive effects in antiferroelectric perovskites*, J. Appl.Phys **52**, 1455 (1981).

[47] G. Shirane, *Ferroelectricity and antiferroelectricity in ceramic $PbZrO_3$ containing Ba or Sr*, Phys. Rev. **86**, 219 (1952).

[48] A. P. Levanyuk and D. G. Sannikov, *Anomalies in dielectric properties in phase transitions*, Sov. Phys. JETP **28**, 134 (1968).

[49] R. Ranjan, D. Pandey, and N. P. Lalla, *Novel features of $Sr_{1x}Ca_xTiO_3$ phase diagram: evidence for competing antiferroelectric and ferroelectric interactions*, Phys. Rev. Lett. **84**, 3726 (2000).

[50] D. Kan, L. Plov, V. Anbusathaiah, C. J. Cheng, S. Fujino, V. Nagarajan, K. M. Rabe and I. Takeuchi, *Universal behavior and electric-field-induced structural transition in rare-earth-substituted $BiFeO_3$*, Adv. Funct. Mater. **20**, 1108 (2010).

[51] C. A. Randall, A. S. Bhalla, T. R. Shrout and L. E. Cross, *Classification and consequences of complex lead perovskite ferroelectrics with regard to B-site cation order*, J. Mater. Res. **5**, 829 (1990).

[52] C. A. Randall, D. J. Barber, P. Groves and R. W. Whatmore, *TEM study of the disorder-order perovskite, $Pb(In_{1/2}Nb_{1/2})O_3$*, J. Mater Sci. **23**, 3678 (1988).

[53] C. A. Randall, S. A. Markgraf, A. S. Bhalla, and K. Baba-Kishi, *Incommensurate structures in highly ordered complex perovskites $Pb(Co_{1/2}W_{1/2})O_3$ and $Pb(Sc_{1/2}Ta_{1/2})O_3$*, Phys. Rev. B **40**, 413 (1989).

[54] F.-T. Huang, X. Wang, Y. S. Oh, K. Kurushima, S. Mori, Y. Horibe, and S.-W. Cheong, *Delicate balance between ferroelectricity and antiferroelectricity in hexagonal $InMnO_3$*, Phys. Rev. B **87**, 184109 (2013).

[55] Y. Kumagai, A. A. Belik, M. Lilienblum, N. Leo, M. Fiebig, and N. A. Spaldin, *Observation of persistent centrosymmetricity in the hexagonal manganite family*, Phys. Rev. B **85**, 174422 (2012).

[56] J. Müller, T. S. Böscke, U. Schröder, S. Mueller, D. Bräuhaus, U. Böttger, L. Frey, and T. Mikolajick, *Ferroelectricity in simple binary ZrO_2 and HfO_2*, Nano. Lett. **12**, 4318 (2012).

[57] W. Y. Pan, C. Q. Dam, Q. M. Zhang, and L. E. Cross, *Large displacement transducers based on electric field forced phase transition in the tetragonal $(Pb_{0.97}La_{0.02})(Ti,Zr,Sn)O_3$ family of ceramics*, J. Appl. Phys. **66**, 6014 (1989).

[58] D. M. Newns, B. G. Elmegreen, X.-H. Liu and G. J. Martyna, *High response piezoelectric and piezoresistive materials for fast, low voltage switching: simulation and theory of transduction physics at the nanometer-scale*, Adv. Mater. **24**, 3672 (2012).

[59] A. S. Mischenko, Q. Zhang, J. F. Scott, R. W. Whatmore, N. D. Mathur, *Giant electrocaloric effect in thin-film $PbZr_{0.95}Ti_{0.05}O_3$*, Science **311**, 1270 (2006).

[60] M. S. Mirshekarloo, K. Yao and T. Sritharan, *Large strain and high energy storage density in orthorhombic perovskite $(Pb_{0.97}La_{0.02})(Zr_{1xy}Sn_xTi_y)O_3$ antiferroelectric thin films*, Appl. Phys. Lett. **97**, 142902 (2010).

[61] V. Tomer, E. Manias and C. A. Randall, *High field properties and energy storage in nanocomposite dielectrics of poly(vinylidene fluoride-hexafluoropropylene)*, J. Appl. Phys. **110**, 044107 (2011).

[62] K. A. Müller and H. Burkard, *$SrTiO_3$: An intrinsic quantum paraeletric below 4 K*, Phys. Rev. B **19**, 3593 (1979).

[63] W. Cochran, *Crystal stability and the theory of ferroelectricity*, Adv. Phys. **9**, 387 (1960).

[64] A. M. Glazer, *The classification of tilted octahedra in perovskites*, Acta Cryst. B **28**, 3384 (1972).

[65] C. J. Howard and H. T. Stokes, *Group-theoretical analysis of octahedral tiltings in perovskites*, Acta Cryst. B **54**, 782 (1998).

[66] P. M. Woodward, *Octahedral tilting in perovskites, I geometrical considerations*, Acta Cryst. B **53**, 32 (1997).

[67] P. M. Woodward, *Octahedral tilting in perovskites, II structure stabilizing forces*, Acta Cryst. B **53**, 44 (1997).

[68] J. W. Bennett, *Discovery and design of functional materials: Integration of database searching and first principles calculations*, Phys. Procedia **34**, 14 (2012).

[69] P. Ghosez, E. Cockayne, U. V. Waghmare, K. M. Rabe, *Lattice dynamics of* $BaTiO_3$, $PbTiO_3$, *and* $PbZrO_3$*: A comparative first-principles study*, Phys. Rev. B **60**, 836 (1999).

[70] E. Cockayne and B. P. Burton, *Phonons and static dielectric constant in* $CaTiO_3$ *from first principles*, Phys. Rev. B **62**, 3735 (2000).

[71] W. Zhong and D. Vanderbilt, *Competing structural instabilities in cubic perovskites*, Phys. Rev. Lett. **74**, 2587 (1995).

[72] S. A. T. Redfern, *High-temperature structural phase transitions in perovskite* $CaTiO_3$, J. Phys.: Conden. Matt. **8**, 8267 (1996).

[73] M. W. Lufaso and P. M. Woodward, *Prediction of the crystal structures of perovskites using the software program SPuDS*, Acta Cryst. B **57**, 725 (2001).

[74] O. E. Fesenko, R. V. Kolesova, and Y. G. Sindeyev, *The structural phase transitions in lead zirconate in super-high electric fields*, Ferroelectrics **20**, 177 (1978).

[75] H. Fujishita, Y. Shiozaki, N. Achiwa and E. Sawaguchi, *Crystal structure determination of antiferroelectric* $PbZrO_3$ *−Application of profile analysis method to powder method of X-ray and neutron diffraction*, J. Phys. Soc. Jpn. **51**, 3583 (1982).

[76] H. Fujishita and S. Hoshino, *A study of structural phase transitions in antiferroelectric* $PbZrO_3$ *by neutron diffraction*, J. Phys. Soc. Jpn. **53**, 226 (1984).

[77] E. Sawaguchi, *Ferroelectricity versus antiferroelectricity in the solid solutions of* $PbZrO_3$ *and* $PbTiO_3$, J. Phys. Soc. Jpn. **8**, 615 (1953).

[78] H. Fujishita, Y. Ishikawa, A. Ogawaguchi, K. Kato, E. Nishibori, M. Takata, M. Sakata, *Temperature dependence of structures and order parameters in antiferroelectric* $PbHfO_3$, Ferro. **301**, 139 (2004).

[79] H. Fujishita, Y. Ishikawa, A. Ogawaguchi, K. Kato, E. Nishibori, M. Takata, M. Sakata, *A study of structures and order parameters in antiferroelectric $PbHfO_3$ by synchrotron radiation*, J. Phys. Soc. Jpn. **74**, 2743 (2005).

[80] G. Shirane and S. Hoshino, *X-ray study of phase transitions in $PbZrO_3$ containing Ba or Sr*, Acta Cryst. **7**, 203 (1954).

[81] H. D. Megaw, *The seven phases of sodium niobate*, Ferro. **7**, 87 (1974).

[82] I. Lefkowitz, K. Lukaszewicz, and H. D. Megaw, *Hight-temperature phases of sodium niobate and nature of transitions in pseudosymmetric structures*, Acta Cryst. **20**, 670 (1966).

[83] Yu. I. Yuzyuk *et al.*, *Modulated phases in $NaNbO_3$: Raman scattering, synchrotron x-ray diffraction, and dielectric investigations*, Phys. Condens. Matter. **17**, 4977 (2005).

[84] L. E. Cross and B. J. Nicholson, *The optical and electrical properties of single crystals of sodium niobate*, Philos. Mag. **46**, 45366 (1955).

[85] E. A. Wood, R. C. Miller, and J. P. Remeika, *Field-induced ferroelectric phase of sodium niobate*, Acta Cryst. **15**, 1273 (1962).

[86] V. A. Shuvaeva, M. Yu. Antipin, S. V. Lindeman, O. E. Fesenko, V. G. Smotrakov, and Yu. T. Struchkov, Kristallografiya, **37**, 1502 (1992).

[87] A. V. Ulinzheyev, O. E. Fesenko and V. G. Smotrakov, *Super-high field-induced phase transitions in $NaNbO_3$ crystals*, Ferro. Lett. **12**, 17 (1990).

[88] S. E. Reyes-Lillo and K. M. Rabe, *Antiferroelectricity and ferroelectricity in epitaxially strained $PbZrO_3$ from first principles* Phys. Rev. B **88**, 180102 (2013).

[89] S. E. Reyes-Lillo, K. F. Garrity and K. M. Rabe, *Antiferroelectricity in thin film ZrO_2 from first principles*, ArXiv:1403.3878 (2014).

[90] O. Dieguez, S. Tinte, A. Antons, C. Bungaro, J. B. Neaton, K. M. Rabe, and D. Vanderbilt, *Ab initio study of the phase diagram of epitaxial $BaTiO_3$*, Phys. Rev. B **69**, 212101 (2004).

[91] E. Bousquet, J. Junquera and P. Ghosez, *First-principles study of competing ferroelectric and antiferroelectric instabilities in $BaTiO_3/BaO$ superlattices*, Phys. Rev. B **82**, 045426 (2010).

[92] G. Henkelman and H. Jonsson, *Improved tangent estimate in the nudged elastic band method for finding minimum energy paths and saddle points*, J. Chem. Phys. **113**, 9978 (2000).

[93] G. Henkelman, B. P. Uberuaga, and H. Jonsson, *A climbing image nudged elastic band method for finding saddle points and minimum energy paths*, J. Chem. Phys. **113**, 9901 (2000).

[94] R. Machado, M. Sepliarsky, and M. G. Stachiotti, *Relative phase stability and lattice dynamics of $NaNbO_3$ from first-principles calculations*, Phys. Rev. B **84**, 134107 (2011).

[95] K. J. Choi, M. Biegalski, Y. L. Li, A. Sharan, J. Schubert, R. Uecker, P. Reiche, Y. B. Chen, X. Q. Pan, V. Gopalan, L.-Q. Chen, D. G. Schlom, and C. B. Eom, *Enhancement of ferroelectricity in strained $BaTiO_3$ thin films*, Science **306**, 1005 (2004).

[96] N. A. Pertsev, A. K. Tagantsev, and N. Setter, *Phase transitions and strain-induced ferroelectricity in $SrTiO_3$ epitaxial thin films*, Phys. Rev. B **61**, R825 (2000).

[97] C.-J. Eklund, C. J. Fennie, and K. M. Rabe, *Strain-induced ferroelectricity in orthorhombic $CaTiO_3$ from first principles*, Phys. Rev. B **79**, 220101 (2009).

[98] D. Berlincourt, *Transducers using forced transitions between ferroelectric and antiferroelectric states*, IEEE Trans. Sonics Ultrason. **13**, 116 (1966).

[99] S-T. Zhang, A. B. Kounga, W. Jo, C. Jamin, K. Seifert, T. Granzow, J. Rödel, and D. Damjanovic, *High-strain lead-free antiferroelectric electrostrictors*, Adv. Mater. **21**, 4716 (2009).

[100] B. Jaffe, *Antiferroelectric ceramics with field-enforced transitions: New nonlinear circuit elements*, Proc. IRE **49**, 1264 (1961).

[101] G. R. Love, *Energy storage in ceramic dielectrics*, J. Am. Ceram. Soc. **73**, 323 (1990).

[102] D. Viehland, *Transmission electron microscopy study of high-Zr-content lead zirconate titanate*, Phys. Rev. B **52**, 778 (1995).

[103] P. Ayyub, S. Chattopadhyay, R. Pinto and M. S. Multani, *Ferroelectric behavior in thin films of antiferroelectric materials*, Phys. Rev. B **57**, R5559 (1998).

[104] A. Roy Chaudhuri, M. Arredondo, A. Hahnel, A. Morelli, M. Becker, M. Alexe, and I. Vrejoiu, *Epitaxial strain stabilization of a ferroelectric phase in $PbZrO_3$ thin films*, Phys. Rev. B **84**, 054112 (2011).

[105] K. Yamakawa, K. Wa. Gachigi, S. Trolier-McKinstry, and J. P. Dougherty, *Phase transitions of antiferroelectric lead zirconate thin films in high electric field*, Ferro. Lett. **20**, 149 (1996).

[106] L. Pintilie, K. Boldyreva, M. Alexe and D. Hesse, *Coexistence of ferroelectricity and antiferroelectricity in epitaxial $PbZrO_3$ films with different orientations*, J. Appl. Phys. **103**, 024101 (2008).

[107] Y. Liu, X. Lu, Y. Jin, S. Peng, F. Huang, Y. Kan, T. Xu, K. Min, and J. Zhu, *Tunable electric properties of $PbZrO_3$ films related to the coexistence of ferroelectricity and antiferroelectricity at room temperature*, Appl. Phys. Lett. **100**, 212902 (2012).

[108] http://opium.sourceforge.net

[109] N. Zhang, H. Yokota, A. M. Glazer and P. A. Thomas, *The not so simple cubic structure of $PbZr_{1-x}Ti_xO_3$ (PZT): complex local structural effects in perovskites*, Acta Cryst. B **67**, 461 (2011).

[110] N. A. Pertsev, A. G. Zembilgotov, and A. K. Tagantsev, *Effect of mechanical boundary conditions on phase diagrams of epitaxial ferroelectric thin films*, Phys. Rev. Lett. **80**, 1988 (1998).

[111] O. Dieguez, K. M. Rabe and D. Vanderbilt, *First-principles study of epitaxial strain in perovskites*, Phys. Rev. B **72**, 144101 (2005).

[112] D. I. Woodward and I. M. Reaney, *Electron diffraction of tilted perovskites*, Acta Cryst. B **61**, 387 (2005).

[113] H. Fujishita, Y. Ishikawa, S. Tanaka, A. Ogawaguchi and S. Katano, *Crystal structure and order parameters in the phase transition of antiferroelectric $PbZrO_3$*, J. Phys. Soc. Jpn. **72**, 1426 (2003).

[114] D. J. Singh, *Structure and energetics of antiferroelectric* $PbZrO_3$, Phys. Rev. B **52**, 12559 (1995).

[115] M. D. Johannes and D. J. Singh, *Crystal structure and electric field gradients of* $PbZrO_3$ *from density functional calculations*, Phys. Rev. B **71**, 212101 (2005).

[116] R. Kagimura and D. J. Singh, *First-principles investigations of elastic properties and energetics of antiferroelectric and ferroelectric phases of $PbZrO_3$*, Phys. Rev. B **77**, 104113 (2008).

[117] K. Boldyreva1, D. Bao, G. Le Rhun, L. Pintilie, M. Alexe, and D. Hesse, *Microstructure and electrical properties of $(120)_O$-oriented and of $(001)_O$ oriented epitaxial antiferroelectric $PbZrO_3$ thin films on (100) $SrTiO_3$ substrates covered with different oxide bottom electrodes*, J. Appl. Phys. **102**, 044111 (2007).

[118] M. T. Bohr, R. S. Chau, T. Ghani and K. Mistry, *The high-k solution*, IEEE Spectrum **44** (10), 29 (2007).

[119] J. A. Kittl *et al.*, *High-k dielectrics for future generation memory devices*, Microelectron. Eng. **86** (7-9), 1789 (2009).

[120] S. K. Kim, S. W. Lee, J. H. Han, B. Lee, S. Han and C. S. Hwang, *Capacitors with an equivalent oxide thickness of* <0.5 *nm for nanoscale electronic semiconductor memory*, Adv. Funct. Mater. **20** 2989 (2010).

[121] D. Panda and T. -Y. Tseng, *Growth, dielectric properties, and memory device applications of ZrO_2 thin films*, Thin Solid Films **531**, 1 (2013).

[122] J. H. Choi, Y. Mao, J. P. Chang, *Development of hafnium based high-k materials−A review*, Mater. Sci. Eng. R **72**, 97 (2011).

[123] R. Ruh, H. J. Garrett, R. F. Domagala and N. M. Tallan, *System zirconia-hafnia*, J. Am. Ceram. Soc. **51** (1), 23 (1968).

[124] A. P. Mirgorodsky, M. B. Smirnov, P. E. Quintard and T. Merle-Mejean, *Strain-induced destabilization of crystals: Lattice dynamics of the cubic-tetragonal phase transition in ZrO_2*, Phys. Rev. B **52**, 9111 (1995).

[125] K. S. Keun and C. S. Hwang, *Atomic layer deposition of ZrO_2 thin films with high dielectric constant on TiN substrates*, Electrochem. and Solid-State Lett. **11** (3), G9 (2008).

[126] H. Kim, P. C. McIntyre, K. C. Saraswat, *Microstructural evolution of ZrO_2-HfO_2 nanolaminate structures grown by atomic layer deposition*, J. Mater. Res. **19** (2), 643 (2004).

[127] R. C. Garvie, *Stabilization of the tetragonal structure in zirconia microcrystals*, J. Phys. Chem. **82**, 218 (1978).

[128] S. Mueller, J. Mueller, A. Singh, S. Riedel, J. Sundqvist, U. Schroeder, and T. Mikolajick, *Incipient ferroelectricity in Al-doped HfO_2 thin films*, Adv. Funct. Mater. **22**, 2412 (2012).

[129] J. Müller, U. Schröder, T. S. Böscke, I. Müller, U. Böttger, L. Wilde, J. Sundqvist, M. Lemberger, P. Kücher, T. Mikolajick, and L. Frey, *Ferroelectricity in yttrium-doped hafnium oxide*, J. Appl. Phys. **110**, 114113 (2011).

[130] S. Mueller, C. Adelmann, A. Singh, S. Van Elshocht, U. Schroeder and T. Mikolajick, *Ferroelectricity in Gd-doped HfO_2 thin films*, ECS J. Solid State Sci. Technol. **1**, N123 (2012).

[131] T. S. Böscke, St. Teichert, D. Bräuhaus, J. Müller, U. Schröder, U. Böttger, and T. Mikolajick, *Phase transitions in ferroelectric silicon doped hafnium oxide*, Appl. Phys. Lett. **99**, 112904 (2011).

[132] T. S. Böscke, J. Müller, D. Bräuhaus, U. Schröder and U. Böttger, *Ferroelectricity in hafnium oxide thin films*, Appl. Phys. Lett. **99**, 102903 (2011).

[133] T. Schenk, S. Mueller, U. Schroeder, R. Materlik, A. Kersch, M. Popovici, C. Adelmann, S. Van Elshocht, and T. Mikolajick, *Strontium doped hafnium oxide thin films: wide process window for ferroelectric memories*, ESSDERC (2013).

[134] J. Müller, T. S. Böscke, D. Bräuhaus, U. Schröder, U. Böttger, J. Sundqvist, P. Kücher, T. Mikolajick, and L. Frey, *Ferroelectric $Hf_{0.5}Zr_{0.5}O_2$ thin films for nonvolatile memory applications*, Appl. Phys. Lett. **99**, 112901 (2011).

[135] M. H. Park, H. J. Kim, Y. J. Kim, W. Lee, T. Moon, and C. S. Hwang, *Evolution of phases and ferroelectric properties of thin $Hf_{0.5}Zr_{0.5}O_2$ films according to the thickness and annealing temperature*, Appl. Phys. Lett. **102**, 242905 (2013).

[136] E. H. Kisi, C. J. Howard and R. J. Hill, *Crystal-structure of orthorhombic zirconia in partially stabilized zirconia*, J. Am. Ceram. Soc. **72**, 1757 (1989).

[137] J. W. Bennett, K. F. Garrity, K. M. Rabe, and D. Vanderbilt, *Orthorhombic ABC Semiconductors as Antiferroelectrics*, Phys. Rev. **110**, 017603 (2013).

[138] J. Lasave, S. Koval, N. S. Dalal, and R. L. Migoni, *Origin of antiferroelectricity in $NH_4H_2PO_4$ from first principles*, Phys. Rev. Lett. **98**, 267601 (2007).

[139] H. J. F. Jansen, *Electronic structure of cubic and tetragonal zirconia*, Phys. Rev. B **43**, 7267 (1991)

[140] G. -M. Rignanese, F. Detraux, X. Gonze, and A. Pasquarello, *First-principles study of dynamical and dielectric properties of tetragonal zirconia*, Phys. Rev. B **64**, 134301 (2001).

[141] X. Zhao and D. Vanderbilt, *Phonons and lattice dielectric properties of zirconia*, Phys. Rev. B **65**, 075105 (2002).

[142] J. E. Lowther, J. K. Dewhurst, J. M. Leger, and J. Haines, *Relative stability of* ZrO_2 *and* HfO_2 *structural phases*, Phys. Rev. B **60**, 14485 (1999).

[143] H. Ding, A. V. Virkar and L. Feng, *Defect configuration and phase stability of cubic versus tetragonal yttria-stabilized zirconia*, Solid State Ionics **215**, 16 (2012).

[144] J. Joo, T. Yu, Y. W. Kim, H. M. Park, F. Wu, J. Z. Zhang and T. Hyeon, *Multigram scale synthesis and characterization of monodisperse tetragonal zirconia nanocrystals*, J. Am. Chem. Soc. **125**, 6553 (2003).

[145] C. Jovalekic, M. Zdujic, D. Poleti, Lj. Karanovic and M. Mitric, *Structural and electrical properties of the* $2Bi_2O_3 \cdot 3ZrO_2$ *system*, J. Sol. Stat. Chem. **181**, 1321 (2008).

[146] K. Parlinski, Z-. Q. Li and Y. Kawazoe, *First-principles determination of the soft mode in cubic* ZrO_2, Phys. Rev. Lett. **78**, 4063 (1997).

[147] D. Fischer, and A. Kersch, *The effect of dopants on the dielectric constant of* HfO_2 *and* ZrO_2 *from first principles*, Appl. Phys. Lett. **92**, 012908 (2008).

[148] D. Fischer, and A. Kersch, *Stabilization of the high-k tetragonal phase in* HfO_2*: The influence of dopants and temperature from ab initio simulations*, J. Appl. Phys. **104**, 084104 (2008).

[149] X. Zhao and D. Vanderbilt, *First-principles study of structural, vibrational, and lattice dielectric properties of hafnium oxide*, Phys. Rev. B **65**, 233106 (2002).

[150] S. Clima, D. J. Wouters, C. Adelman, T. Schenk, U. Schroeder, M. Jurczak, and G. Pourtois, *Identification of the ferroelectric switching process and dopant-dependent switching properties in orthorhombic* HfO_2*: A first principles insight*, Appl. Phys. Lett. **104**, 092906 (2014).

[151] G. Shirane, R. Newnham, and R. Pepinsky, *Dielectric properties and phase transitions of* $NaNbO_3$ *and* $(Na,K)NbO_3$, Phys. Rev. **96**, 581 (1954).

[152] H. Shimizu, Y. Mizuno and C. Randall, private communication (2014).

[153] S. P. Solovev, Y. N. Venevtsev and G. S. Zhdanov, *An X-ray study of phase transitions in* $NaNbO_3$, Sov. Phys. Cryst. **6**, 218 (1961).

[154] K. E. Johnston, C. C. Tang, J. E. Parker, K. S. Knight, P. Lightfoot and S. E. Ashbrook, *The polar phase of* $NaNbO_3$*: A combined study by powder diffraction, solid-state NMR, and first-principles calculations*, J. Am. Chem. Soc. **132**, 8732 (2010).

[155] C. N. W. Darlington, H. D. Megaw, *Low-temperature phase-transition of sodium niobate and structure of low-temperature phase, N*, Acta Cryst. B **29**, 2171 (1973).

[156] L. E. Cross, *Electric double hysteresis in $(K_xNa_{1-x})NbO_3$ single crystals*, Nature **181**, 178 (1958).

[157] S. K. Mishra, N. Choudhury, S. L. Chaplot, P. S. R. Krishna, and R. Mittal, *Competing antiferroelectric and ferroelectric interactions in $NaNbO_3$: Neutron diffraction and theoretical studies*, Phys. Rev. B **76**, 024110 (2007).

[158] S. K. Mishra, R. Mittal, V. Yu. Pomjakushin, and S. L. Chaplot, *Phase stability and structural temperature dependence in sodium niobate: A high-resolution powder neutron diffraction study*, Phys. Rev. B **83**, 134105 (2011).

[159] Y. Xu, W. Hong, Y. Feng and X. Tan, *Antiferroelectricity induced by electric field in $NaNbO_3$-based lead-free ceramics*, Appl. Phys. Lett. **104**, 052903 (2014).

[160] K. Konieczny, *Pyroelectric and dielectric study of $NaNbO_3$ single crystals*, Mater. Scien. and Engineering **B60**, 124 (1999).

[161] S. Curtarolo, G. L. W. Hart, M. B. Nardelli, N. Mingo, S. Sanvito and O. Levy, *The high-throughput highway to computational materials design*, Nat. Mater. **12**, 191 (2013).

[162] V. I. Anisimov *et al.*, *Band theory and Mott insulators: Hubbard U instead of Stoner I*, Phys Rev B **44**, 943 (1991).

[163] G. Kresse and J. Hafner, *Ab initio molecular-dynamics simulation of the liquid-metal-amorphous-semiconductor transition in germanium*, Phys. Rev. B **49** 14251, 1994.

[164] G. Kresse and J. Furthmller, *Efficiency of ab-initio total energy calculations for metals and semiconductors using a plane-wave basis set*, Comput. Mat. Sci. **6** 15, 1996.

[165] V. A. Shuvaeva, M. Yu. Antipin, R. S. V. Lindeman, O. E. Fesenko, V. G. Smotrakovup and Yu. T. Struchkov, *Crystal structure of the electric-field induced ferroelectric phase of $NaNbO_3$*, Ferro. **141**, 307 (1993).

[166] J. Ravez, *The inorganic fluoride and oxyfluoride ferroelectrics*, J. Phys. III France **7**, 1129 (1997).

[167] A. T. Mulder, N. A. Benedek, J. M. Rondinelli, and C. J. Fennie, *Turning ABO_3 antiferroelectrics into ferroelectrics: Design rules for practical rotation-driven ferroelectricity in double perovskites and $A_3B_2O_7$ Ruddlesden-Popper compounds*, Adv. Funct. Mater. **23**, 4810 (2013).

[168] N. A. Benedek and C. J. Fennie, *Why are there so few perovskite ferroelectrics?*, J. Phys. Chem. C **117**, 13339 (2013).

[169] D. H. Kim, H. N. Lee, M. Varela and H. M. Christen, *Antiferroelectricity in multiferroic $BiCrO_3$ epitaxial films*, Appl. Phys. Lett. **89**, 162904 (2006).

[170] A. Belsky, M. Hellenbrandt, V. L. Karen, and P. Luksch, *New developments in the inorganic crystal structure database (ICSD): accessibility in support of materials research and design*, Acta Crystallogr. Sect. B. **58**, 364 (2002).

[171] A. A. Belik, S. Y. Stefanovich, B. I. Lazoryak and E. Takayama-Muromachi, *$BiInO_3$: a polar oxide with $GdFeO_3$-type perovskite structure*, Chem. Mater. **18**, 1964 (2006).

[172] K. Oka *et al.*, *Pressure-induced spin-state transition in $BiCoO_3$*, J. Am. Chem. Soc. **132**, (27) 9438 (2010).

[173] N.V. Sidorov, M. N. Palatnikov, N. A. Teplyakova, E. Y. Obryadina, L. A. Alyoshina, N. A. Evdokimova and E. P. Feklistova, *Investigation into the structure of ceramic $Li_xNa_{1-x}Ta_{0.1}Nb_{0.9}O_3$ solid solutions by X-ray analysis and Raman spectroscopy*, Crystall. Reps. **58**, 541 (2013).

[174] W. H. Zachariasen, *Crystal chemical studies of the 5f-series of elements. XIV. Oxyfluorides, XOF*, Acta Cryst. **4**, 231 (1951).

[175] M. Vlasse, M. Saux, P. Echegut, G. Villeneuve, *Crystallographic and NMR-study of ScOF oxyfluoride*, Mater. Res. Bull. **14**, 807 (1979).

[176] A. Taoudi, J. P. Laval, B. Frit, *Synthesis and crystal structure of three new rare earth oxyfluorides related to baddeleyite [LnOF; Ln= Tm, Yb, Lu]*, Mater. Res. Bull. **29**, 1137 (1994).

[177] N. Al-Aqtash, F. Apostol, W.-N. Mei, R. F. Sabirianov, *Electronic and optical properties of $TaO_{1-x}N_{1+x}$-based alloys*, J. Sol. State Chem. **198**, 337 (2013).

[178] D. I. Woodward, J. Knudsen and I. M. Reaney, *Review of crystal and domain structures in the $PbZr_xTi_{1-x}O_3$ solid solution*, Phys. Rev. B **72**, 104110 (2005).

[179] K. Fujii, H. Kato, K. Omoto, M. Yashima, J. Chen and X. Xing, *Experimental visualization of the Bi-O covalency in ferroelectric bismuth ferrite ($BiFeO_3$) by synchrotron X-ray powder diffraction analysis*, Phys. Chem. Chem. Phys. **15**, 6779 (2013).

[180] A. W. Sleight and C. T. Prewitt, *High-pressure $HgTiO_3$ and $HgPbO_3$ − Preparation, charcaterization, and structure*, J. Sol. State Chem. **6**, 509 (1973).

[181] I. K. Jeong and S. Park, *Correlated thermal motion in ferroelectric $LiNbO_3$ studied using neutron total scattering and a rietveld analysis*, J. Kor. Phys. Soc. **59**, 2756 (2011).

[182] S. C. Abrahams and J. L. Bernstein, *Ferroelectric lithium tantalate−1. single crystal X-ray diffraction study at 24^oC* , J. Phys. and Chem. of Solids **28**, 1685 (1967).

[183] C. Muller, J. L. Baudour, C. Bedoya, F. Bouree, J. L. Soubeyroux and M. Roubin, *Octahedral deformations and cationic displacements in the ferroelectric $PbHf_{0.8}Ti_{0.2}O_3$: a neutron powder diffraction study from 10 to 770 K*, Acta Cryst. B **56**, 27 (2000).

[184] H. Yokota, N. Zhang, P. A. Thomas and A. M. Glazer, *Crystal structure determinations of Zr rich-$PbZr_{1-x}Ti_xO_3$*, Ferro. **414**, 147 (2011).

[185] Y. Inaguma, M. Yoshida and T. Katsumata, *A polar oxide $ZnSnO_3$ with a $LiNbO_3$-type structure*, J. Am. Chem. Soc. **130**, 6704 (2008).

[186] J. Ko amd C. T. Prewitt, *High-pressure phase-transition in $MnTiO_3$ from the ilmenite to the $LiNbO_3$ structure*, Phys. Chem. Minerals **15**, 355 (1988).

[187] M. Wolcyrz and M. Lukaszewski, *The crystal-structure of the room-temperature phase of $AgTaO_3$*, Zeitschrift fuer Kristallographie **177**, 53 (1986).

[188] A. W. Sleight and C. T. Prewitt, *Preparation of $CuNbO_3$ and $CuTaO_3$ at high pressure*, Mater. Res. Bull. **5**, 207 (1970).

[189] M. -R. Li *et al.*, *A polar corundum oxide displaying weak ferromagnetism at room temperature*, J. Am. Chem. Soc. **134**, 3737 (2012).